University of Southern Queensland

Steady and Unsteady Free Surface Flow Past a Two-Dimensional Stern

A thesis submitted in fulfilment of

Doctor of Philosophy

Osama Nasser Ogilat

B.Sc., M.Sci.

2013

Abstract

The research examines an influence of a platform shape on free surface waves generated behind a semi-infinite two-dimensional platform moving with a constant speed on a water surface of a finite depth h. The fluid is assumed to be inviscid, incompressible and irrotational; the surface tension effect is neglected. The aim of the research is to find analytically and numerically such platform shape which minimizes generated waves and reduces wave drug exerting on a moving platform when the Froude number is relatively small, $F < 1$. It is shown that for certain platform shapes, generated waves can be minimised or even eliminated, at least, within the framework of a linearized theory.

Linearized hydrodynamic equations for a fluid of finite depth are solved analytically by means of the Fourier transform and Wiener–Hopf technique, as well as numerically with the help of boundary integral technique. A weakly nonlinear solution is also obtained for shallow-water approximation within the framework of the forced Korteweg–de Vries (KdV) equation.

The problem is investigated for steady motion of a platform having a different stern shape. Then the analysis is performed for unsteady motion of a platform having a flat shape. The linearized problem for a water of finite depth is solved by means of the Laplace transform and Wiener–Hopf technique. The linear problem is formulated by assuming that at the initial instant of time the free surface is slightly perturbed due to the platform submerging onto the depth $d \ll h$ beneath the free surface. It is shown that the unsteady solution approaches the steady state solution as $t \to \infty$. The dependence of maximum wave perturbation on the fluid depth is found numerically.

In the last Chapter 6 the analysis is extended to steady motion of a flat platform at the interface between two fluids of different density. It is assumed that the lower layer has a finite depth h, whereas the upper layer is infinite. Results obtained for internal waves on the sharp density interface depend on the density ratio $a = \rho_1/\rho_2$ and in the limit $a \to 0$ they coincide with the results obtained for surface waves.

The results of this research can help in understanding of the physics of wave generation past a bluff body (e.g., wide blunt ships) and shed some light on solving an engineering problem of ship building of an optimal shape.

Statement of Original Authorship

The work contained in this thesis has not been previously submitted to meet requirements for an award at this or any other higher educational institution. To the best of my knowledge and belief, the thesis contains no material previously published or written by another person except where due reference is made.

Candidate: Osama Nasser Ogilat

Signed: ______________________________

Date: ______________________________

ENDORESMENT

Principal supervisor: Associate Professor Yury Stepanyants

Signed: ______________________________

Date: ______________________________

Acknowledgements

My first and foremost thanks to ALLAH for the opportunities that He has given to me throughout my life, especially those that have brought me to the position of finishing this thesis.

I would like to express my thankfulness and gratitude to my principle supervisor Professor Yury Stepanyants for his invaluable assistance, support, patience and guidance during the period of my research. My special thanks are addressed to my associate supervisor Dr Dmitry Strunin for his advice, support and constructive feedback. Deepest gratitude is also due to Professor Ian Turner, Dr Scott McCue and Professor John Belward without their knowledge and assistance this study would not have been successful. Warmest thanks to Dr Ben Binder for his contribution to our joint paper published in Physics of Fluids. I would like to thank all postgraduate students and staff of the Department of Mathematics and Computing of USQ for providing a very good scientific environment for mathematical research.

I am indebted to the most important person in my live, my mother "Gazeah", for her incredible support, love and patience through my many years in education. My special thanks to my wonderful brothers, Khaled, Amjad, Ahmad and Moa'ath and sisters, Manal, Tharwah, Khawlah, Hend, Wisam and Ebtsam who always wished my success. I am also thankful to my sisters-in-law and brothers-in-law who always supported me. I should not forget my relatives (uncles and cousins), as well as friends.

This thesis is dedicated to my mother; and to the soul of my father (ALLAH bless upon him), that I wish he is alive to see what I have achieved and to share my happiness for completing this Theses, who encouraged and directed me for education and provided me with safe financial living before and after he passed away.

Keywords

Boundary integral technique, Wiener–Hopf technique, weakly nonlinear theory, free surface flow, steady flow, unsteady flow, Fourier transform, Laplace transform, conformal mapping, Korteweg–de Vries (KdV) equation.

List of Publications

O. Ogilat, S. W. McCue, I. W. Turner, J. A. Belward, and B. J. Binder. Minimising wave drag for free surface flow past a two-dimensional stern. *Physics of Fluids*, 2011, v. 23, p. 072101.

O. Ogilat, Y. Stepanyants. Transient free surface flow past a two-dimensional flat stern. (*Accepted in Physics of Fluids journal*).

O. Ogilat, Y. Stepanyants. Minimising internal wave generation past steadily moving flat platform in two-layer fluid of finite depth. (*To be submitted to the journal Physics of Fluids*).

Contents

List of Figures

List of Tables

Chapter 1

Introduction and Literature Review

When a ship moves in a relatively calm water, one of the most distinctive features is the wave pattern that forms on the water surface. Such wave patterns, whether caused by a ship in the sea, or by a duck swimming in a pond, or by a boat crossing a river, are called *ship waves* [70]. If the wave pattern does not change in time, it is referred to as a steady phenomenon; if it does change in time then it is an unsteady phenomenon. Generation of these patterns creates wave resistance, which in turn requires greater power from the moving object, e.g., ship engine. Reduction of wave resistance leads to increase the speed of the ship end higher efficiency of ship engine.

The aim of this research is to find the shape of the free surface created behind curved sterns and to design a two-dimensional model of ship stern that minimises, or completely eliminates, the trailing waves or swirl.

This research deals with two-dimensional problems for free surface and internal flows in two-layer fluid past a model of a ship stern in a fluid of finite depth. The problem is treated in two-dimensional formulation because it is too complicated for study in three-dimensional case. In the meantime, the flow behind a wide ship can be considered at certain approximation as two-dimensional if the edge effects are negligible. This research assumes that the fluid is incompressible, the flow is irrotational, and the effect of viscosity is negligible. Gravity at the free surface is included, but surface tension is neglected.

The free-surface flow past the stern of two-dimensional semi-infinite plate modelling a wide ship is investigated analytically using the Wiener–Hopf technique [5] and numerically using the boundary integral technique [27]. These two techniques have been used successfully by several authors to solve the free-surface flow past a ship stern (see, e.g., [30, 31, 85, 82, 83, 84, 92, 37]). The weakly nonlinear theory is also used to describe the flow on the free surface through the application of the Korteweg–de Vries equation [88]. Furthermore, the two-layer model for the free surface flow past a semi-infinite flat plate in a fluid with infinite upper layer and finite-depth lower layer is investigated analytically (see [89, 90]).

In this research we use two aforementioned techniques to examine the problem earlier considered by McCue & Stump [85] for two-dimensional steady flow past a semi-infinite flat platform. That problem can be generalised to an arbitrary stern shape, when Froude number F less than 1, where the Froude number is the ratio of plate speed V to the speed of long linear surface waves, $\sqrt{gh}$.

1.1 Two-dimensional free surface flow past a semi-infinite stern

Two-dimensional free surface flow past a semi-infinite ship stern in a fluid of finite depth is an important research subject, because it can model a real flow near the stern of the ship. Such a model would need to examine the behavior of the free surface where it interconnects with the ship stern. Two types of flow where the free surface detaches from the stern are considered here. The first is when the free surface detaches from the stern at the stagnation point, and the second is when the free surface detaches from the stern smoothly (i.e, tangentially).

The problem of wave generation behind the stern of a ship in a fluid of infinite depth has been treated numerically for the case when the free surface was attached to the body at the stagnation point (Vanden-Broeck & Tuck [49], Vanden-Broeck, Schwartz & Tuck [51], Madurasinghe [65], and Farrow & Tuck [13]). Madurasinghe [65], Farrow & Tuck [13] and Asavanant & Vanden-Broeck [40] managed to eliminate surface waves at the stagnation point.

Less attention was given to the free surface flow in fluids of finite depth. McCue & Forbes [83] investigated numerically subcritical solutions ($F < 1$), where the free surface detaches from the body at the stagnant point. These solutions are characterised by an upstream train of waves.

In this research it will be studied only the problem when the free surface detaches smoothly from the stern. The analysis of steady flow and surface waves generation will be given in Chapters 2–4, whereas the unsteady flow will be studied in in Chapter 5. In Chapter 6 the steady flow problem past plane semi-infinite stern will be generalised for two-layer fluid. The main assumption is that the free surface detaches from the plate stern at the tangential separation for the subcritical solution when the Froude number $F = V/\sqrt{gh} < 1$, where V is the velocity of the fluid downstream, g is acceleration due to gravity, and h is water depth.

1.1.1 Steady flows in fluid of infinite depth

A steady flow past the stern of a ship in a fluid of infinite depth has been investigated by Schmidt [30], who used the Wiener–Hopf technique to show that there are no downstream waves for a particular family of curved ship sterns, where the free surface detaches smoothly from the stern. Schmidt also established two methods to locate the separation point between the stern and free surface adopted from Schmidt and Sparenberg [31]. In contrast, Vanden-Broeck [47] numerically investigated the free surface flow past a semi-infinite flat stern using the boundary integral equation method. Vanden-Broeck generated waves downstream when the flow separates tangentially from the flat stern. The numerical solution to the stern flow problem was also investigated by Madurasinghe and Tuck [66], who found a waveless solution on the free surface, where the flow separated smoothly from the polygonal body. Additionally, Farrow and Tuck [13] numerically examined the free surface profile when the flow detaches smoothly from the stern and found a waveless solution for the free surface flow past the double-flat stern. Zhu and Zhang [87] considered analytically the time dependent linear problem and showed that the steady state is asymptotically achievable in the long time limit. Solving the steady problem by means of the Wiener–Hopf technique the authors showed that the closed form solution in the far field zone can be obtained for an arbitrary hull shape. Haussling [32] treated transient linear and nonlinear problems numerically for the ship model moving with draught-defined Froude numbers $\mathrm{Fr} \equiv V/\sqrt{gd} \in [1, 4]$, where V is ship velocity, g is acceleration due to gravity, and d is the draught of the ship. It was shown that for $\mathrm{Fr} > 3$ the nonlinear effects are negligibly small for most practical purposes, whereas for $\mathrm{Fr} < 3$ these effects may be significant.

1.1.2 Steady flows in fluid of finite depth

A steady free surface flow past a semi-infinite flat plate in a fluid of finite depth was considered by McCue and Stump [85], who assumed that the free surface detaches smoothly from the edge of the flat plate. The problem was solved using the Wiener–Hopf technique, and it was shown that there is a family of subcritical solutions characterised by a train of sinusoidal waves in the far downstream zone.

McCue and Forbes [84] showed numerically using the boundary-integral-equation method that there is a waveless solution when the surface flow moves past a semi-infinite flat plate. They also investigated the problem analytically using the Wiener–Hopf technique and identified that the solution is characterised by a train of waves on the free surface for the subcritical solutions, when $F < 1$. On the other hand, Maleewong and Grimshaw [71] considered the same problem for $F \approx 1$. Both the analytical and numerical solutions show that there are downstream waves when a free surface leaves the plate smoothly.

Recently Binder [11] derived weakly nonlinear theory and obtained numerical solutions to the fully nonlinear problem for the free surface flow past a semi-infinite curved plate in a fluid of finite depth. Using the weakly nonlinear theory, Binder eliminated the downstream waves for plate shapes that have zero slope at the detachment with the free surface using a Froude number $F = 0.9$ and small pressure P. However, numerical solutions to the fully nonlinear problem appear to eliminate the waves downstream in scale that includes the flat bottom of the channel.

1.1.3 Unsteady two-dimensional flow

In Chapter 5 of this Theses, the unsteady or *transient* problem is considered for a two-dimensional free surface flow past a semi-infinite plate in a fluid of finite depth. This problem was tackled previously by Haussling [32], for the free surface flow past a plate in a fluid of infinite depth. The author studied the unsteady nonlinear waves created behind the stern of a semi-infinite plate on surface of a fluid of infinite depth using the finite difference numerical method. He formulated the problem by assuming that the stern was moving instantaneously at the free surface in order to generate an unsteady flow. The problem was solved by mapping the coordinates from a physical region to a rectangular region and then discretising the problem. He examined two cases of flat and curved sterns, assuming that the flow separates smoothly from the stern, and additionally calculated the location of the point of separation by applying two conditions. The upstream atmospheric pressure p on the hull must be greater than zero and the separation point downstream on the free surface must be below the hull.

Zhu and Zhang [87] presented an analytical solution for the free surface flow past a ship stern. They formulated the problem by assuming that the stern of a ship moves with constant velocity through the fluid. The linearised problem is solved using the Fourier transform and Wiener–Hopf technique for different stern shapes in a fluid of infinite depth. They used a transient model to show that the steady state is achievable for the large-time limit, and derived the radiation condition for the steady problem.

1.1.4 Steady two-dimensional flow for the two-layer model

In Chapter 6 the steady problem is considered for the two-layer model. It is assumed that the flat plate moves with constant speed along the surface of density interface generating internal waves. Such waves are mostly hidden from eyesight, however, sometimes they produce a visible response at the free surface. The Wiener–Hopf technique is used to solve the problem of the interface flow past a semi-infinite flat plate in a fluid with a finite depth in the lower layer and infinite height in the upper layer. The effect of density ratio on the problem of minimisation of internal waves is studied. It is shown that in the limit when the density ratio of upper fluid to lower fluid becomes very, the results obtained reduce to the problem of surface wave minimisation past flat plate.

1.2 Techniques

1.2.1 Wiener–Hopf technique

The Wiener-Hopf method is a mathematical technique used widely in solving two-dimensional partial differential equations with mixed boundary conditions (Noble; [5]). The boundary conditions are transformed and these transforms are used to define a pair of complex functions (denoted with '+' and '-' subscripts) that are analytic in the upper and lower halves of the complex plane, respectively. These two functions also coincide on some region of the complex plane, such as a thin strip. Analytic continuation of these two functions defines a single function analytic in the entire complex plane. Liouville's theorem ([18], p. 85) implies that this function is an unknown polynomial and by analysis of the complex functions determines the degree of this polynomial. For example, a function, $A(k)$, analytic in a horizontal strip $0 < \mathrm{Im}(k) < \tau$, the following decomposition into a difference or quotient of functions $A_+(k)$ and $A_-(k)$ may be used:

$$A(k) = A_+(k) - A_-(k), \quad \text{or} \quad A(k) = \frac{A_+(k)}{A_-(k)}.$$

Here function $A_+(k)$ is analytic in the upper-half plane, whereas $A_-(k)$ is analytic in the lower-half plane.

The Wiener–Hopf method has been used by many researcher (among them Schmidt and Sparenberg [31], Schmidt [30], McCue and Stump [85], and Zhu and Zhang [87], for solving the stern flow problem namely, because mixed boundary conditions are used in the formulation of this problem.

1.2.2 Boundary-integral-equation technique

The boundary-integral-equation (BIE) method is based on the reformulation of the free surface flow problem to a system of nonlinear integro-differential equations for the unknown function on the free surface. These equations are then discretised and the resultant nonlinear algebraic equations are solved by iteration (for example, by using Newton's method). The BIE method can be applied in many areas of science and engineering including fluid mechanics [46].

In this research the BIE method is used to solve the nonlinear free surface problem numerically by applying the conformal mapping to transform the problem from a physical plane to the non-physical plane where the free surface is known. A further mapping of the flow region onto a half-plane enables Cauchy's integral theorem to be applied to a function on that region. An integral equation for the unknown function on the free surface then derived using the boundary integral technique to produce a system of nonlinear equations solvable by Newton's iterative method. The BIE method of solving free surface problems has been adopted and used successfully by many researches including Forbes and Schwartz ([59], 1982), Orszag [15], Meiron [14], King and Bloor [1], Ellis [93], Hoffman [43], Andersson and Vanden-Broeck [12] and Binder [11].

1.3 Research objectives

The main research objectives are;

1 – Determine the shape of the free surface created behind a stern of a constantly moving plate

The shape of the free surface created behind bodies in a uniform stream is of practical importance, as it applies to the flow of fluid at the stern of a ship. The shape of the free surface when it detaches smoothly behind the stern of a ship is found analytically using the Wiener–Hopf technique, numerically using the boundary integral equation method, and then analytically for a weakly nonlinear problem.

2 – Design a two-dimensional stern that minimises or completely elimi-

nates downstream waves

When a ship travels through a water it generates waves. These waves contain an amount of energy equal to the work done by the ship hull on the fluid. Minimisation of energy required to propel a ship requires minimisation of the wave resistance, by minimising the wave train left behind the ship.

In the steady problem, three different configurations of stern shape are examined in this research. In the first case it is assumed that the ship stern has a slope monotonically increasing in x. For this configuration, the linear, nonlinear and weakly nonlinear solutions are solved and it is found that the wave amplitude can be minimised for this plate shape. In the second case the stern shapes were examined by Binder [11]. These shapes are characterised by the zero slope at the point at which the free surface detaches from the stern. For this configuration, the amplitude of the waves for the weakly nonlinear solution vanishes completely, while the linear and nonlinear solutions have a very small wave amplitude. Finally, its shown in this study that when the stern shape has a downward-angle at the detachment point, the wave amplitude for the nonlinear solution can be completely eliminated.

3 – Investigate an asymptotic behavior of a transient solution for surface waves generated by a flat plate

For the unsteady problem, the shape of the stern is considered flat in this research. The linear solution is solved and it was found that the solution obtained asymptotically approaches the steady solution as $t \to \infty$ for the case of the flat plate.

4 – Generalise the surface wave problem to internal waves in two-layer fluid

For the simplest stern shape (flat plate) the steady problem is considered in two-layer fluid of different density. Assuming that a plate moves with constant speed along the surface of density interface, the Wiener–Hopf technique is used to find the profile of generated internal waves in a fluid with a finite depth in the lower layer and infinite height in the upper layer. The effect of density ratio on the problem of minimisation of internal waves is studied. It is shown that in the limit when the density ratio of upper fluid to lower fluid becomes very, the results obtained reduce to the problem of surface wave minimisation past flat plate.

1.4 Content of this research

The free surface flow past a semi-infinite curved plate in a fluid of finite depth is investigated. Past researches on this subject has been primarily dedicated to the case of flow in a fluid of infinite depth. Binder [11] investigated the free surface flow past a semi-infinite curved plate in a fluid of finite depth for a particular family of stern shapes for the nonlinear and weakly nonlinear cases. These results were developed further for different families of plate shapes for the linear, nonlinear and weakly nonlinear problems. It was discovered that for the particular family of stern shapes solutions obtained can provide a minimum of generated waves or even the motion without downstream waves at all. This study is devoted to further contribution to this problem. The outline of the research is as follow:

- Chapter 2 – the curved plate problem (depicted in figure 2.1) is solved. After formulating the problem, the Fourier transform and the Wiener–Hopf technique are used to solve curve plate problem for the case of subcritical flow, $F < 1$. The free surface consists of a sinusoidal component and monotonically decaying portion for different stern shapes.

- Chapter 3 describe how the problem can solved numerically. A conformal mapping is proposed and the boundary-integral-equation method is applied. A numerical scheme is used to solve the nonlinear integral equation, and different shapes of the plate are examined.

- Chapter 4 contains a comparison between the analytical, numerical and weakly nonlinear solutions for different stern shapes. A method for manipulating the shape of the plate to eliminate the downstream waves is demonstrated; a comparison of results obtained are presented against known from the literature.

- Chapter 5 defines an unsteady problem in the linear approximation for free surface waves generated behind the flat model of a ship stern. It is shown how the problem can be solved analytically using the Laplace transform and Wiener–Hopf technique.

- Chapter 6 presents a solution of the stationary problem of internal waves generation in two-layer fluid of finite depth in the lower layer and infinite depth in the upper layer. The problem is solved analytically in the linear approximation for different density ratios using the Fourier transform and Wiener–Hopf technique.

- Chapter 7 contains conclusion and discussions of results obtained for the steady and unsteady two-dimensional free surface flow past a ship stern and highlights further avenues of research in this field.

Chapter 2

Exact Solution to the Linearised Steady Problem

2.1 Introduction

In this chapter, free surface flow past a semi-infinite curved plate in a fluid of finite depth is considered (see figure 2.1). We assume that the free surface separates from the edge of the plate tangentially. The linearised problem is solved exactly using a Fourier transform and the Wiener–Hopf technique, for subcritical flow ($F < 1$), and for different families of plate shapes. The free surface consists of a sinusoidal component and monotonically decaying portion.

This problem has been studied by many authors for the case of a flat plate. For example, McCue and Stump [85] considered the free surface flow past a semi-infinite flat plate in a fluid of finite depth, where the free surface detaches smoothly from the edge of the flat plate. The problem was solved using the Wiener–Hopf technique, and it was shown that there is a family of subcritical solutions characterised by a train of sinusoidal waves far downstream. Maleewong and Grimshaw [71] and McCue and Forbes [82] solved the fully nonlinear problem numerically using the boundary integral equation method, when a free surface flows past a semi-infinite flat plate. They generated waves downstream of the plate edge, including gravity but neglecting surface tension. Recently, Binder [11] solved the problem of the free surface flow past a semi-infinite curved plate in a fluid of finite depth numerically, using the boundary integral equation method and weakly nonlinear theory. He showed that using the weakly nonlinear theory the wave amplitude vanish completely for Froude number $F \sim 1$.

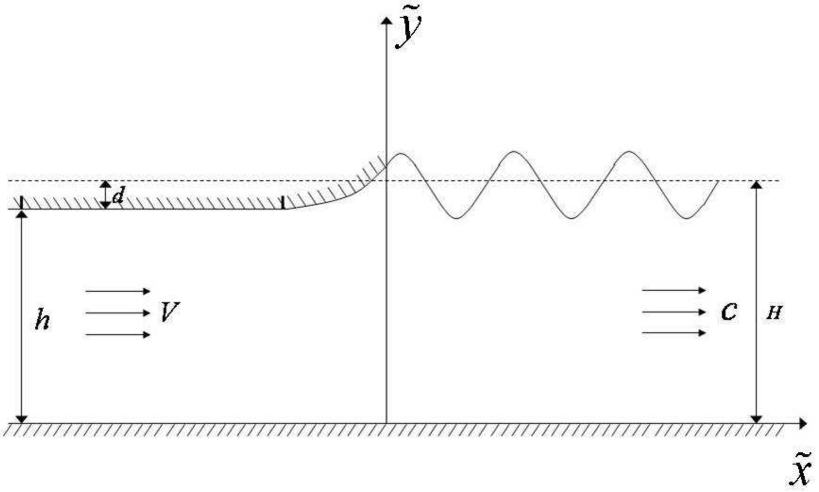

FIGURE 2.1: A schematic of the free surface flow past a semi-infinite curved plate in a finite depth fluid.

2.2 Mathematical Formulation

Steady two-dimensional free surface flow past a semi-infinite curved plate in a fluid of finite depth is shown in Figure 2.1. It is assumed that the curved plate steadily pushes into the fluid. The fluid is inviscid and incompressible, and the flow is irrotational. Surface tension is assumed to be negligible.

The distance between the horizontal bottom of the fluid and the curved plate is indicated by h, the height of the undisturbed free surface is indicated by H, and the draft of the ship denoted by d. The fluid far upstream is uniform with a constant depth $h = H - d$ and speed V. The velocity far upstream, using mass conservation, is given by $V = \frac{cH}{H-d}$ as $\tilde{x} \to -\infty$, where c is given by

$$c = \frac{Vh}{H}. \tag{2.1}$$

The Cartesian coordinates are introduced so that the $\tilde{x}$-axis lies at the bottom of the fluid and the $\tilde{y}$-axis is vertically upwards. For $\tilde{x} < 0$ the fluid is bounded above by a semi-infinite curved plate, and for $\tilde{x} > 0$, the upper boundary consists of a free surface (see Figure 2.1).

Since we assumed the flow is incompressible, the velocity potential Φ satisfies Laplace's equation

$$\nabla^2 \Phi = \frac{\partial^2 \Phi}{\partial \tilde{x}^2} + \frac{\partial^2 \Phi}{\partial \tilde{y}^2} = 0 \quad \text{for} \quad -\infty < \tilde{x} < \infty, \quad \text{on} \quad 0 < \tilde{y} < h + \tilde{\eta}(\tilde{x}), \tag{2.2}$$

and the $\tilde{x}$ and $\tilde{y}$ components of the velocity, $\tilde{u}$ and $\tilde{v}$, respectively, are given by

$$\tilde{u} = \frac{\partial \Phi}{\partial \tilde{x}}, \quad \tilde{v} = \frac{\partial \Phi}{\partial \tilde{y}}.$$

The normal component of the fluid velocity at any boundary is zero. As we have a curved plate, a free surface and a horizontal bottom, we have the following conditions

$$\frac{\partial \Phi}{\partial \tilde{y}} = 0 \quad \text{for} \quad -\infty < \tilde{x} < \infty, \quad \text{on} \quad \tilde{y} = 0, \tag{2.3}$$

$$\frac{\partial \Phi}{\partial \tilde{y}} = \tilde{\eta}'(\tilde{x}) \frac{\partial \Phi}{\partial \tilde{x}} \quad \text{for} \quad -\infty < \tilde{x} < \infty, \quad \text{on} \quad \tilde{y} = h + \tilde{\eta}(\tilde{x}), \tag{2.4}$$

where $\tilde{\eta}(\tilde{x})$ is the unknown location of the free surface for $\tilde{x} > 0$ and a specified a *priori* for $x < 0$. An additional condition is found by applying Bernoulli's equation on $\tilde{y} = h + \tilde{\eta}(\tilde{x})$, namely,

$$\frac{1}{2}\left[\left(\frac{\partial \Phi}{\partial \tilde{x}}\right)^2 + \left(\frac{\partial \Phi}{\partial \tilde{y}}\right)^2\right] + g\tilde{y} = \frac{1}{2}V^2 + gh + \frac{\tilde{P}}{\rho} \quad \text{for} \quad 0 < \tilde{x} < \infty, \tag{2.5}$$

where g is the acceleration due to gravity, ρ is the density, $\tilde{P} = \tilde{P}_{-\infty} - \tilde{P}_a$ is the difference between the pressure $\tilde{P}_{-\infty}$ applied to the plate as $x \to -\infty$ and the atmospheric pressure $\tilde{P}_a$ on the free surface. The unknown free surface for $\tilde{x} < 0$ and the known curved plate for $\tilde{x} > 0$ is described by $\tilde{y}$.

This problem is formulated by non-dimensionalising all lengths with respect to the height h and all velocities with resect to the speed V. Let $u = \tilde{u}/V$, $v = \tilde{v}/V$, $x = \tilde{x}/h$, $y = \tilde{y}/h$, $\phi = \Phi/Vh$, $P = \tilde{P}/\rho g h$ and $\eta = \tilde{\eta}/h$, applying these, equations (2.2), (2.3), (2.4) and (2.5) become

$$\nabla^2\phi = \frac{\partial^2\phi}{\partial x^2} + \frac{\partial^2\phi}{\partial y^2} = 0 \quad \text{for} \quad -\infty < x < \infty, \quad \text{on} \quad 0 < y < 1 + \eta(x), \tag{2.6}$$

with the boundary conditions

$$\frac{\partial\phi}{\partial y} = 0 \quad \text{for} \quad -\infty < x < \infty, \quad \text{on} \quad y = 0, \tag{2.7}$$

$$\frac{\partial\phi}{\partial y} = \eta'(x)\frac{\partial\phi}{\partial x} \quad \text{for} \quad -\infty < x < \infty \quad \text{on} \quad y = 1 + \eta(x), \tag{2.8}$$

$$\frac{1}{2}(u^2+v^2) + \frac{1}{F^2}y = \frac{1}{2} + \frac{1}{F^2}(1+P), \quad \text{for} \quad 0 < x < \infty, \quad \text{on} \quad y = 1+\eta(x), \tag{2.9}$$

$$\frac{\partial\phi}{\partial x} \sim 1 \quad \text{as} \quad x \to \infty,$$

for $x > 0$, where the two dimensionless parameters in the problem, the Froude number F and the applied pressure P, are defined as

$$F = \frac{V}{\sqrt{gH}}, \qquad P = \frac{\tilde{P}_{-\infty} - \tilde{P}_a}{\rho g H}. \tag{2.10}$$

It is assumed that the uniform flow is slightly perturbed, which gives the perturbation expansions

$$\phi(x,y) = x + \frac{P}{1-F^2}\phi_1(x,y) + O\left(\frac{P^2}{(1-F^2)^2}\right), \tag{2.11}$$

and

$$\eta(x) = \frac{P}{1-F^2}(1+\eta_1(x)) + O\left(\frac{P^2}{(1-F^2)^2}\right), \tag{2.12}$$

where the small parameter $P/(1-F^2) << 1$ is the dimensionless distance between the height of the plate and the undisturbed free surface. This parameter is chosen so that the linear problem coincides with McCue and Stump [85] for special case of a flat plate (recall our problem is nondimensionalised as in Binder [11], not McCue and Stump [85]).

After nondimensionalising the problem, we now linearise using the perturbation expansions given in (2.11) and (2.12). By substituting the expansion into (2.6), (2.7), (2.8) and (2.9), we obtain

$$\frac{\partial^2 \phi_1}{\partial x^2} + \frac{\partial^2 \phi_1}{\partial y^2} = 0, \quad -\infty < x < \infty, \quad 0 < y < 1, \tag{2.13}$$

with the boundary conditions given by

$$\frac{\partial \phi_1}{\partial y} = 0, \quad -\infty < x < \infty, \quad y = 0, \tag{2.14}$$

$$F^2 \frac{\partial^2 \phi_1}{\partial x^2} + \frac{\partial \phi_1}{\partial y} = n(x), \quad x < 0, \quad y = 1, \tag{2.15}$$

$$\frac{\partial \phi_1}{\partial y} = m(x), \quad x < 0, \quad y = 1. \tag{2.16}$$

Here, $m(x) = d\eta_1/dx$ is a known function that describes the shape of the plate for $x < 0$, with the assumed behaviour,

$$|m(x)| \leq K_1 e^{\tau_+ x} \quad \text{as} \quad x \to -\infty, \tag{2.17}$$

where K_1 and τ_+ are constants and $m(x)$ is expected to be periodic in the limit $x \to -\infty$. The function $n(x)$ is unknown and describes the pressure on the plate for $x < 0$, and is assumed to decay to zero, satisfying

$$|n(x)| \leq K_2 e^{\tau_- x} \quad \text{as} \quad x \to -\infty,$$

where K_2 is constant, and $\tau_- < 0$. In addition, given condition (2.17), it is expected that

$$|n(x)| \leq K_3 e^{\tau_+ x} \quad \text{as} \quad x \to -\infty, \tag{2.18}$$

where K_3 is a constant. τ_+ and τ_- determine which part of the complex plane, upper or lower-half plane, the function $n(x)$ is analytic.

We are particularly interested in the quantity

$$\eta_1(x) = -F^2 \left(1 + \frac{\partial \phi_1}{\partial x}(x, 1) \right), \quad \text{for} \quad x > 0, \tag{2.19}$$

which will describe the shape of the free-surface in the generalised solution.

McCue and Stump [85] solved the same problem by considering a flat plate, *i.e.*, $m(x) = 0$. In the present work the problem is solved for the case of a curved plate.

2.3 Wiener–Hopf technique

2.3.1 Application Of The Fourier Transform

Following McCue and Stump [85], we solve (2.13)-(2.16) with the Wiener–Hopf technique. From linear water wave theory, we expect the solution for $\phi_1(x, y)$ to be oscillatory far downstream with

$$\phi_1 \sim \text{constant} \times \cosh(\mu_R y) \times \cos(\mu_R x + \nu) \quad \text{as} \quad x \to \infty,$$

where $\mu_R > 0$ is the real positive root of the transcendental equation

$$\tanh \mu_R = \mu_R F^2, \tag{2.20}$$

and ν is a phase shift (that must be determined as part of the full solution to (2.13)-(2.16)). Thus, the Fourier transform

$$\hat{\phi}(k, y) = \int_{-\infty}^{\infty} \phi_1(x, y) \mathrm{e}^{\mathrm{i}kx} \mathrm{d}x \tag{2.21}$$

will not converge for real values of k, but instead must hold in the infinitely long strip $0 < \mathrm{Im}(k) < \tau_+$ that can be detected by the far field behaviour of the function $\phi_1(x, y)$.

By applying the Fourier transform (2.21) to Laplace's equation (2.13) and using (2.14), we find that $\hat{\phi}$ is given by

$$\hat{\phi}(k, y) = A(k) \cosh ky. \tag{2.22}$$

The transformation of the boundary conditions (2.14)-(2.16) give

$$kA(k) \sinh k = \hat{m}(k), \qquad kA(k) \left[\sinh k - F^2 k \cosh k \right] = \hat{n}_-(k), \tag{2.23}$$

both of which hold in the strip $0 < \mathrm{Im}(k) < \tau_+$(see Figure 2.2(a)). Here $\hat{m}(k)$ and $\hat{n}_-(k)$ are the Fourier transforms of $m(x)$ and $n(x)$, respectively. The equation (2.23) is solved for the two unknown functions $\hat{m}(k)$ and $\hat{n}(k)$ in the following subsection. Once $\hat{m}(k)$ is determined, we recover the unknown free surface through (2.19) and the inverse transform

$$\frac{\partial \phi_1}{\partial x}(x, 1) = \frac{1}{2\pi \mathrm{i}} \int_{-\infty+\mathrm{i}\delta}^{\infty+\mathrm{i}\delta} \frac{\hat{m}(k)}{\tanh k} \mathrm{e}^{-\mathrm{i}kx} \mathrm{d}k, \tag{2.24}$$

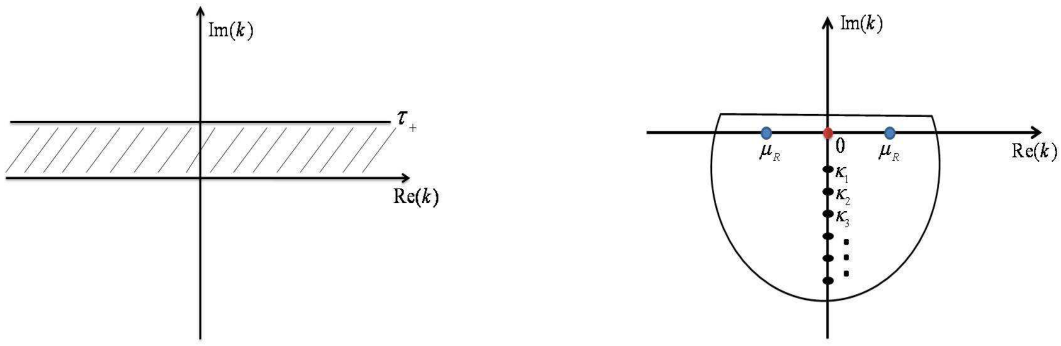

(a) (b)

FIGURE 2.2: Figure (a) shows the strip $0 < \text{Im}(k) < \tau_+$. Figure (b) shows the path of integration in the lower half k-plane.

where δ is a real constant in the range $0 < \delta < \tau_+$, forcing the path of integration to lie in the strip $0 < \text{Im}(k) < \tau_+$ as required (Noble[5], 1988).

By differentiating (2.24) with respect to x at $y = 1$, and using (2.22)-(2.23), it is found that

$$\frac{\partial \phi_1}{\partial x}(x, 1) = \frac{1}{2\pi i} \int_{-\infty+i\delta}^{\infty+i\delta} \frac{\hat{m}(k)}{\tanh k} e^{-ikx} dk. \tag{2.25}$$

where $\hat{m}(k)$ is found in Section 2.3.2, which is given by

$$\hat{m}(k) = \frac{C_0 + C_1 k}{P_+(k)(1 - \frac{k^2}{\mu_R^2})} + \frac{J_-(k)}{P_+(k)}, \tag{2.26}$$

which together with (2.19) and (2.25), provides an integral expression for the shape of the free surface $\eta(x)$ in terms of an inverse Fourier transform. Despite the complicated nature of $\hat{m}(k)$, we are able to invert the Fourier transform (2.25) exactly, as shown below.

For $x > 0$, the integral (2.25) is evaluated by closing the path of integration with a large semi-circle in the lower half k-plane (see Figure 2.2(b)). An examination of (2.25) reveals that the integrand has poles inside the closed contour when the denominator is zero, which will happen for $k = 0$. In addition the integrand may also have poles inside the contour, where $\hat{m}(k)$ is singular. These poles are located at $k = \kappa_j$, for $j = 1, 2....$ By summing the residues it is found that

$$\frac{\partial \phi_1}{\partial x}(x, 1) = -\hat{m}(0) - \sum_j \frac{\mathrm{Res}_{k=\kappa_j} \hat{m}(k)}{\tanh \kappa_j} e^{-i\kappa_j x}, \tag{2.27}$$

Now, given the solution for $\hat{m}(k)$ in (2.26), we find that $\hat{m}(k)/\tanh k$ has poles inside the closed contour when $k = 0$, $k = \pm\mu_R$ where $\mu_R > 0$ is real and satisfies

$$\tanh \mu_R = \mu_R F^2, \tag{2.28}$$

and also for $k = -\mathrm{i}\pi\mu_n$ for $n = 1, 2, \ldots$, where the μ_n are real and satisfy

$$\tan \pi\mu_n = \pi\mu_n F^2. \tag{2.29}$$

It follows that, by summing the residues, equation (2.27) can be written as

$$\begin{aligned} \frac{\partial \phi_1}{\partial x}(x, 1) &= -\hat{m}(0) - \frac{1}{2F^2 P_+(\mu_R) P_-(\mu_R)} \times \\ &\left[P_+(-\mu_R)(C_0 + C_1\mu_R) e^{-i\mu_R x} + P_+(\mu_R)(C_0 - C_1\mu_R) e^{i\mu_R x} \right] \\ &+ \sum_{j=1}^{\infty} \frac{-\pi\mu_j\mu_R F^2 P_-(i\pi\mu_j)\left[C_0 - C_1 i\pi\mu_j + (1 + \frac{\pi^2\mu_j^2}{\mu_R^2}) J_-(-i\pi\mu_j) \right]}{1 - F^2 + \pi^2\mu_j^2 F^4} e^{-\pi\mu_j x}. \end{aligned}$$

It is important to note that this solution is comprised of a constant term $-\hat{m}(0)$, a sinusoidal term and an infinite sum of terms that decay exponentially fast as $x \to \infty$. Thus, by substituting the above equation into (2.19), the shape of the free surface has the behaviour

$$\eta_1(x) \sim -F^2 + F^2\hat{m}(0) + A\sin(\mu_R x + \nu), \tag{2.30}$$

as $x \to \infty$, where A is the amplitude of the downstream waves and ν is a phase shift, both of which depend on F, $m(x)$ and $n(x)$. From linear water wave theory this behaviour should only include the sinusoidal wavetrain. Thus,

$$-F^2 + F^2\hat{m}(0) = 0,$$

and therefore,

$$\hat{m}(0) = 1. \tag{2.31}$$

Putting it together, after some algebra, we find the shape of the free surface is thus given by

$$\begin{aligned}\eta_1(x) &= \frac{-F\sqrt{\pi}\cosh(\mu_R)}{\mu_R T(\mu_R)T(-\mu_R)}\mathrm{Re}\left(T(\mu_R)\Gamma\left(1-\frac{i\mu_R}{\pi}\right)\Gamma\left(\frac{3}{2}+\frac{i\mu_R}{\pi}\right)(C_0 - C_1\mu_R)e^{i\mu_R x}\right) \\ &+\sum_{j=1}^{\infty}\frac{\mu_j\mu_R F^3 T(i\pi\mu_j)\Gamma(\mu_j)\left[C_0 - C_1 i\pi\mu_j + (1+\frac{\pi^2\mu_j^2}{\mu_R^2})J_-(-i\pi\mu_j)\right]}{\sqrt{\pi}(\frac{1}{2}+\mu_j)\Gamma(\frac{1}{2}+\mu_j)[1-F^2+\pi^2\mu_j^2F^4]}e^{-\pi\mu_j x}. \quad (2.32)\end{aligned}$$

A further calculation shows the amplitude A is given by

$$A = \sqrt{2}F\sqrt{\frac{C_0^2 - C_1^2\mu_R^2}{F^2+\mu_R^2F^4-1}}. \quad (2.33)$$

Consequently, the amplitude vanishes when $C_0^2 = C_1^2\mu_R^2$ and both $C_0 = 0$ and $C_1 = 0$.

2.3.2 The Wiener–Hopf equation

In the previous section, the solution of the free surface profile was given in terms of the unknown function $\hat{m}(k)$. In this section, the unknown function $\hat{m}(k)$ is solved by eliminating $A(k)$ from (2.23) to give

$$\hat{m}(k) = \frac{\hat{n}_-(k)}{(1-F^2k\coth k)}, \quad (2.34)$$

where $\hat{n}_-(k)$ is analytic function in the lower-half plane ($\mathrm{Im}(k) < \tau_+$), which is given by

$$\hat{n}_-(k) = \int_{-\infty}^{0} n(x)e^{ikx}dx. \quad (2.35)$$

Anticipating the use of the Wiener–Hopf technique, $\hat{m}(k)$ in (2.34) can be written as

$$\hat{m}(k) = \hat{m}_-(k) + \hat{m}_+(k),$$

where

$$\hat{m}_-(k) = \int_{-\infty}^{0} m(x)e^{ikx}dx, \qquad \hat{m}_+(k) = \int_{0}^{\infty} m(x)e^{ikx}dx, \quad (2.36)$$

are analytic functions in the lower and upper-half plane ($\mathrm{Im}(k) < \tau_+$), ($\mathrm{Im}(k) > 0$) respectively.

For our problem, the transform $\hat{m}_-(k)$ is an input to the problem (since the slope of the plate $m(x) = \mathrm{d}\eta_1(x)/\mathrm{d}x$ is known for $x < 0$) while the functions $\hat{m}_+(k)$ and $\hat{n}_-(k)$ are two unknowns that physically represent the (transforms of the) slope of the free surface for $x > 0$ and the pressure on the plate for $x < 0$, respectively. Therefore, it follows that the Wiener–Hopf equation (2.34) becomes:

$$\hat{m}_+(k) + \hat{m}_-(k) = \frac{\hat{n}_-(k)}{G(k)}, \tag{2.37}$$

in the strip $0 < \mathrm{Im}(k) < \tau_+$, where

$$G(k) = 1 - F^2 k \coth k. \tag{2.38}$$

The method of solving equation (2.37) depends crucially on a decomposition of $G(k)$ of the form

$$G(k) = \left(1 - \frac{k^2}{\mu_R^2}\right) P_+(k) P_-(k), \tag{2.39}$$

where $P_+(k)$ is analytic and non-zero in the upper-half plane ($\mathrm{Im}(k) > 0$), and $P_-(k) = P_+(-k)$ is analytic and non-zero in the lower-half plane ($\mathrm{Im}(k) < \tau_+$). Here $\mu_R > 0$ is defined in (2.28), and the actual form of $P_+(k)$ is given later in this section. The details of this factorization will be given later in this Section.

Now, substituting (2.39) into (2.37), we obtain

$$\left(1 - \frac{k^2}{\mu_R^2}\right) \left[P_+(k)\hat{m}_+(k) + P_+(k)\hat{m}_-(k)\right] = \frac{\hat{n}_-(k)}{P_-(k)}. \tag{2.40}$$

To proceed further, the function $J(k)$ is introduced and defined by

$$J(k) = P_+(k)\hat{m}_-(k). \tag{2.41}$$

Splitting these functions into $J(k) = J_+(k) + J_-(k)$, where $J_+(k)$ and $J_-(k)$ are analytic in the half-planes $\mathrm{Im}(k) > 0$ and $\mathrm{Im}(k) < \tau_+$, respectively. The details of this splitting are postponed until later in this section.

Substituting (2.41) into (2.40), the Wiener–Hopf equation (2.37) becomes

$$\left(1 - \frac{k^2}{\mu_R^2}\right) \left[P_+(k)\hat{m}_+(k) + J_+(k)\right] = \frac{\hat{n}_-(k)}{P_-(k)} - \left(1 - \frac{k^2}{\mu_R^2}\right) J_-(k), \tag{2.42}$$

where all the terms on the left-hand side of (2.42) are analytic in the upper half-plane $\mathrm{Im}(k) > 0$, and the terms on the right hand-side are analytic in the lower half-plane $\mathrm{Im}(k) < \tau_+$. Thus, both sides of (2.42) are equal in the strip $0 < \mathrm{Im}(k) < \tau_+$, and each must be the analytic continuation of the other. Furthermore both sides are equal to the as yet unknown function $E(k)$.

To determine the form of $E(k)$ we analyse the behaviour of the left-hand side of (2.42) as $k \to \infty$ in the upper half-plane ($\mathrm{Im}(k) > 0$), and in the lower half-plane ($\mathrm{Im}(k) < \tau_+$) is analysed. Thus, from (2.38) and (2.39), noting $P_-(k) = P_+(-k)$, we find $P_+(k) = O(k^{-1/2})$ as $k \to \infty$. Further, by the application of integration by parts, $\hat{m}_+(k) = O(k^{-1})$ as $k \to \infty$. Finally $J(k)$ is split in such a way that $J_+(k) = O(k^{-1})$ in the upper half-plane and $J_-(k) = O(k^{-1})$ in the lower half-plane as $k \to \infty$, (postponed to later on in this section). Together these results imply that the left-hand side of (2.42) is $O(k)$ as $k \to \infty$ in the upper half-plane $\mathrm{Im}(k) > 0$. Similarly, the right-hand side of (2.42) is $O(k)$ as $k \to \infty$ in the lower half-plane $\mathrm{Im}(k) < \tau_+$. Thus, by Liouvilles's theorem ([18], pg 85) both sides of (2.42) must be equal to the polynomial $E(k) = C_0 + C_1 k$, where C_0 and C_1 are constants left to be determined later in this section.

We have now solved the single equation (2.42) for the two unknowns $\hat{m}_+(k)$ and $\hat{n}_-(k)$; which are given by

$$\hat{n}_-(k) = P_-(k)\left[C_0 + C_1 k + \left(1 - \frac{k^2}{\mu_R^2}\right) J_-(k)\right], \tag{2.43}$$

and

$$\hat{m}_+(k) = \frac{\mu_R^2}{P_+(k)(\mu_R^2 - k^2)}\left[C_0 + C_1 k\right] - \frac{J_+(k)}{P_+(k)}. \tag{2.44}$$

Factorisation of $G(k)$

In McCue and Stump [85] the function $G(k)$, defined in (2.38), is factorised as in (2.39). The details of the factorization of $G(k)$ are handled in the same way to that presented in McCue and Stump [85]. Let $G(k) = f_1(k) f_2(k)$, where the functions $f_1(k)$ and $f_2(k)$ are given by:

$$f_1(k) = \frac{\sinh k}{k} - F^2 \cosh k, \quad f_2(k) = \frac{k}{\sinh k}. \tag{2.45}$$

The splitting of the Wiener–Hopf equation (2.42) depends upon the roots of $f_1(k)$. Here the function $f_1(k)$ has two real roots and infinitely many imaginary roots. The real roots are denoted by $k = \pm\mu_R$, for $\mu_R > 0$. As $F \to 1$, $\mu_R \to 0$, while as $F \to 0$, $\mu_R \sim \frac{1}{F^2}$. The imaginary roots are given by $k = \pm i\pi\mu_n$, for $n = 1, 2, ...$ and $\mu_n > 0$, where $\mu_n = n + \frac{1}{2} - \frac{1}{\pi^2 F^2 n} + O(n^{-2})$ as $n \to \infty$.

By applying the Weierstrass infinite product theorem [29], f_1 can be factored into the form

$$f_1(k) = (1 - F^2)\left(1 - \frac{k^2}{\mu_R^2}\right)\prod_{n=1}^{\infty}\left(1 + \frac{k^2}{\pi^2\mu_n^2}\right) = \left(1 - \frac{k^2}{\mu_R^2}\right)H_+(k)H_-(k), \quad (2.46)$$

where

$$H_+(k) = \sqrt{1 - F^2}\prod_{n=1}^{\infty}\left(1 - \frac{ik}{\pi\mu_n}\right)e^{\frac{ik}{\pi}(\frac{1}{n}-\gamma)}, \quad H_-(k) = H_+(-k),$$

and γ is Euler's constant. The exponential factor in $H_+(k)$ is required for the infinite product to converge. Now by using the result

$$\frac{1}{\Gamma(\frac{3}{2} - \frac{ik}{\pi})} = \frac{2}{\sqrt{\pi}}\prod_{n=1}^{\infty}\left(1 - \frac{ik}{\pi(n+1)}\right)e^{\frac{ik}{\pi}(\frac{1}{n}-\gamma)},$$

it is found that

$$H_+(k) = \frac{\alpha T(k)}{\Gamma(\frac{3}{2} - \frac{ik}{\pi})}, \quad (2.47)$$

is analytic and non-zero in the upper-half k-plane, with,

$$T(k) = \prod_{n=1}^{\infty}\left(\frac{\pi\mu_n - ik}{\pi(n + \frac{1}{2}) - ik}\right) \quad \text{and} \quad \alpha = \sqrt{(1 - F^2)}\frac{\sqrt{\pi}}{2}\prod_{n=1}^{\infty}\left(\frac{n + \frac{1}{2}}{\mu_n}\right). \quad (2.48)$$

The infinite product $T(k)$ is uniformly convergent, as each term has the form $1 + O(n^{-2})$. Furthermore, $T(k)$ has simple zeros at $k = -i\pi\mu_n$, simple poles at $k = -i\pi(n + \frac{1}{2})$ $(n = 1, 2, ...)$, and has the limit $T(k) \to 1$ as $k \to \infty$.

The value of α can be determined explicitly by considering the behaviour of $f_1(k)$ for large k. Thus, from equation (2.46) we find that

$$f_1(k) = \frac{4\alpha^2\pi(\mu_R^2 - k^2)T(k)T(-k)\cosh(k)}{\mu_R^2(\pi^2 + 4k^2)},$$

where $f_1 \sim -\pi\alpha^2 e^k/2\mu_R^2$ as $k \to \infty$. However, from (2.45) it is found that $f_1 \sim -F^2 e^k/2$ in this limit, thus, by comparing these two results, the value of α is found to be

$$\alpha = \frac{\mu_R F}{\sqrt{\pi}}.$$

By applying the Weierstrass infinite product theorem to the function f_2, we find

$$f_2(k) = \frac{k}{\sinh(k)} = \prod_{n=1}^{\infty}\left(1 - \frac{k^2}{n^2\pi^2}\right)^{-1} = S_+(k)S_-(k), \tag{2.49}$$

where

$$S_+(k) = e^{i\gamma k/\pi}\prod_{n=1}^{\infty}\left(1 - \frac{ik}{n\pi}\right)^{-1} e^{-ik/n\pi} = \Gamma\left(1 - \frac{ik}{\pi}\right), \tag{2.50}$$

and $S_-(k) = S_+(-k)$. The functions $S_+(k)$ and $S_-(k)$ are analytic and non-zero in the upper and lower halves of the k-plane, respectively.

In summary, $G(k)$ is split in the form (2.39), with,

$$P_+(k) = H_+(k)S_+(k), \quad \text{and} \quad P_-(k) = H_-(k)S_-(k), \tag{2.51}$$

where $H_+(k) = H_-(-k)$ is given by (2.47) and $S_+(k) = S_-(-k)$ is given by (2.50). By using Stirling's formula ([67], pg 257) we find that

$$P_+(k) \sim \alpha\left(\frac{i\pi}{k}\right)^{1/2} \text{as} \quad k \to \infty \tag{2.52}$$

in the upper-half plane $\text{Im}(k) > 0$, and

$$P_-(k) \sim \alpha\left(\frac{-i\pi}{k}\right)^{1/2} \text{as} \quad k \to \infty \tag{2.53}$$

in the lower-half plane $\text{Im}(k) < \tau_+$.

Splitting of $J(k)$

In this section we describe the key step in the analysis of Section 2.3.2, which is the manner is that $J(k)$, defined in equation (2.41), is split into the sum

$$J(k) = P_+(k)\,\hat{m}_-(k) = J_+(k) + J_-(k), \tag{2.54}$$

where the function $J_+(k)$ is analytic in the upper half-plane, $\text{Im}(k) > 0$, while $J_-(k)$ is analytic in the lower half-plane, $\text{Im}(k) < \tau_+$. The main idea is to apply Cauchy's integral theorem to give

$$J_+(k) = \frac{1}{2\pi i}\int_{-\infty+ic}^{\infty+ic} \frac{J(\zeta)}{\zeta - k} d\zeta \tag{2.55}$$

and

$$J_-(k) = -\frac{1}{2\pi i}\int_{-\infty+id}^{\infty+id} \frac{J(\zeta)}{\zeta - k} d\zeta, \tag{2.56}$$

(see Section 1.3 of Noble [5] for further details), where $\zeta = \xi + ic$ and the constants c and d are defined so that $0 < c < \text{Im}(k) < d < \tau_+$.

There are two possible ways to proceed, depending on the far-field behaviour of the plate as $x \to -\infty$.

Method 1

In method 1, if the slope of the plate $m(x)$ decays continuously to zero as $x \to -\infty$ (i.e., does not have compact support), then $\hat{m}_-(k)$ is not analytic in the upper half-plane, and has singularities at points denoted by κ_j, for $j = 1, 2, ...$ in $\text{Im}(k) > 0$. In this case, we can close the contour in (2.55) with an infinitely large semi-circle in the upper-half $\zeta-$plane to give

$$\begin{aligned} J_+(k) &= J(k) + \sum_j \text{Res}_{\zeta=\kappa_j} \frac{J(\zeta)}{\zeta - k}, \\ &= J(k) + \sum_j \frac{P_+(\kappa_j)}{\kappa_j - k} \quad \text{Res}_{\zeta=\kappa_j} \hat{m}_-(\zeta). \end{aligned}$$

For certain form of $\hat{m}_-(k)$ this step could be undertaken by inspection.

For later use, we note the far field behaviour of $J_+(k)$ is found to be

$$J_+(k) \sim -\left(\sum_j P_+(\kappa_j) \text{Res}_{\zeta=\kappa_j} \hat{m}_-(\zeta) \right) \frac{1}{k} \quad \text{as} \quad k \to \infty \tag{2.57}$$

in the upper half-plane $\text{Im}(k) > 0$.

Method 2

In method 2, we are most interested in the case in which $m(x)$ does have compact support, so that $m(x) = 0$ for $x < -L$, where $L > 0$ is some constant. Here we must be careful, as $\hat{m}_-(k)$ is analytic everywhere, growing exponentially as $k \to \infty$ in the upper half-plane $\text{Im}(k) > 0$. Thus we cannot close the contour in (2.55) in the upper half-plane, as the contribution from the infinitely large semi-circle would not vanish.

Instead, noting from (2.51) that $P_+(k)$ has an infinite number of simple poles in the lower half-plane at $\zeta = -in\pi$ for $n = 1, 2, \ldots$, we close the contour in (2.55) in the lower half-plane to give

$$\begin{aligned} J_+(k) &= -\sum_{n=1}^{\infty} \mathrm{Res}_{\zeta=-in\pi} \frac{J(\zeta)}{\zeta - k}, \\ &= -\sum_{n=1}^{\infty} \frac{\hat{m}_-(-in\pi)}{-in\pi - k} \mathrm{Res}_{\zeta=-in\pi} P_+(\zeta). \end{aligned}$$

Given that

$$P_+(\zeta) \sim \frac{\mu_R F}{\sqrt{\pi}} \frac{T(-\mathrm{i}n\pi)}{\Gamma(3/2-n)} \frac{\mathrm{i}\pi(-1)^n}{(n-1)!(\zeta + \mathrm{i}n\pi)}$$

as $\zeta \to -\mathrm{i}n\pi$, $n = 1, 2, \ldots$, we can use the identity (formula (6.1.6) in ([67], pg 255)),

$$\Gamma\left(\frac{3}{2} - n\right) = \frac{\sqrt{\pi}(-1)^{n+1}4^{n-1}(n-1)!}{(2n-2)!}$$

to show

$$\mathrm{Res}_{\zeta=-in\pi} P_+(\zeta) = \frac{i\mu_R F T(-in\pi)(2n-2)!}{4^{n-1}(n-1)!^2}$$

which can be substituted into the above equation to recover $J_+(k)$.

Again, for later use we note an alternate form for (2.57) is that

$$J_+(k) \sim \left(\sum_{n=1}^{\infty} \hat{m}_-(-\mathrm{i}n\pi) \frac{\mathrm{i}\mu_R F T(-\mathrm{i}n\pi)(2n-2)!}{4^{n-1}((n-1)!)^2} \right) \frac{1}{k} \tag{2.58}$$

as $k \to \infty$.

Determination of the Constants C_0 and C_1

The value of C_0 is found, by substituting (2.31) into (2.26), as

$$C_0 = \sqrt{1 - F^2} - J_-(0). \tag{2.59}$$

The value of C_1, in determining its constants, depends on the detail of $J_+(k)$. Thus, we determine C_1 by studying the behaviour of the left-hand side of the Wiener–Hopf equation in (2.42) in the upper half-plane $\mathrm{Im}(k) > 0$.

Using Method 1, and from (2.57), the left-hand side of (2.42) behaves as

$$-\left(\sum_j \frac{P_+(\kappa_j)\mathrm{Res}_{\zeta=\kappa_j} \hat{m}_-(\zeta)}{\mu_R^2} \right) k \quad \text{as} \quad k \to \infty,$$

then the value of C_1, in this case, is given by

$$C_1 = \sum_j \frac{P_+(\kappa_j)\mathrm{Res}_{\zeta=\kappa_j} \hat{m}_-(\zeta)}{\mu_R^2}. \tag{2.60}$$

Similarly, using Method 2, and from (2.58), if the left-hand side of (2.42) behaves as

$$\left(\sum_{n=1}^{\infty} \hat{m}_{-}(-in\pi)\frac{iFT(-in\pi)(2n-2)!}{\mu_R 4^{n-1}(n-1)!^2}\right)k \quad \text{as} \quad k \to \infty,$$

and thus the value of C_1 takes the form

$$C_1 = -\sum_{n=1}^{\infty} \hat{m}_{-}(-in\pi)\frac{iFT(-in\pi)(2n-2)!}{\mu_R 4^{n-1}((n-1)!)^2}. \tag{2.61}$$

The constants C_0 and C_1 and the two methods that we used to split the function $J(k)$ in this section is the difference between the free surface presented by McCue and Stump [85] for the case of the flat plate, and the free surface for the case of the curved plate that we derived in (2.32). Thus, if we consider $C_0 = 0$, $C_1 = 0$ and $J(k) = 0$ then we get the same solution presented by McCue and Stump [85] for the flat plate as will be shown in the next section.

2.4 Case Studies

Case 1:

In 2000, McCue and Stump [85], considered a stern with a shape given by

$$m(x) = 0 \quad \text{for} \quad x < 0, \quad \text{and} \quad n(x) = 0 \quad \text{for} \quad x > 0.$$

Using (2.36), we find that

$$\hat{m}_{-}(k) = 0,$$

which is analytic in $\text{Im}(k) < \tau_{+}$, and

$$\hat{n}_{+}(k) = 0,$$

which is analytic in $\text{Im}(k) > 0$.

We find the value of $C_0 = \sqrt{1-F^2}$ and $C_1 = 0$. Substituting C_0 and C_1 in the shape of the free surface (2.32), it is found that

$$\begin{aligned} \eta_1(x) &= F\sqrt{\pi(1-F^2)}\frac{-\cosh\mu_R}{\mu_R T(\mu_R)T(-\mu_R)}\text{Re}\left(T(\mu_R)\Gamma(1-\frac{i\mu_R}{\pi})\Gamma(\frac{3}{2}+\frac{i\mu_R}{\pi})e^{i\mu_R x}\right) \\ &+ \sum_{j=1}^{\infty}\frac{\mu_j\mu_R F^3 T(i\pi\mu_j)\Gamma(\mu_j)\sqrt{1-F^2}}{\pi(\frac{1}{2}+\mu_j)\Gamma(\frac{1}{2}+\mu_j)[1-F^2+\pi^2\mu_j^2F^4]}e^{-\pi\mu_j x}. \end{aligned} \tag{2.62}$$

Furthermore, the amplitude of the wave downstream becomes:

$$A = F\sqrt{\frac{2(1-F^2)}{F^2+\mu_R^2 F^4 - 1}}, \tag{2.63}$$

which is the same result as derived by McCue and Stump. This verifies that the solution of the free surface in (2.32) agrees with McCue and Stump for the solution of the free surface in the case of the flat plate with the attachment point $\eta_1(0) = -1$.

In the next cases we will consider different stern shapes to find the free surface profile by using the two methods given in Section 2.3.2.

Case 2:

By considering that the shape of the stern is given by

$$m(x) = ae^{bx} \quad \text{for} \quad x \leq 0, \tag{2.64}$$

where a and b are real and positive, and using the integral in (2.36),

$$\hat{m}_-(k) = \frac{a}{b+ik},$$

which is analytic in the lower half-plane, $\mathrm{Im}(k) < \tau_+$. By closing the contour in the upper-half plane, the value of $J_+(k)$ is calculated using Method 1 in Section 2.3.2. Thus $\hat{m}_-(k)$ has a pole at $k = ib$, and the integral of $J_+(k)$ becomes

$$J_+(k) = J(k) - \frac{aP_+(ib)}{(b+ik)}.$$

This implies that

$$J_-(k) = \hat{m}_-(k)P_+(ib) = \frac{aP_+(ib)}{(b+ik)}. \tag{2.65}$$

From (2.60), the value of C_1 is given by

$$C_1 = \sum_j \frac{P_+(\kappa_j)\mathrm{Res}_{\zeta=\kappa_j}\hat{m}_-(\zeta)}{\mu_R^2} = \frac{-iaP_+(ib)}{\mu_R^2}, \tag{2.66}$$

and from (2.59), C_0 is given by

$$C_0 = \sqrt{1-F^2} - J_-(0) = \sqrt{1-F^2} - \frac{a}{b}P_+(ib). \tag{2.67}$$

Also, from (2.51), the value of $P_+(k)$ is substituted by (2.65), (2.66) and (2.67) into (2.32). The shape of the free surface then becomes

$$\eta_1(x) = \frac{F\sqrt{\pi}}{\mu_R}\Bigg[\frac{-\cosh(\mu_R)}{T(\mu_R)T(-\mu_R)}\mathrm{Re}\Bigg(T(\mu_R)\Gamma(1-\frac{i\mu_R}{\pi})\Gamma(\frac{3}{2}+\frac{i\mu_R}{\pi}) \\ \left(\sqrt{1-F^2}+P_+(ib)(\frac{ia}{\mu_R}-\frac{a}{b})\right)e^{i\mu_R x}\Bigg) \\ +\sum_{j=1}^{\infty}\frac{\mu_j\mu_R^2F^2T(i\pi\mu_j)\Gamma(\mu_j)\left[\sqrt{1-F^2}-\frac{a\pi\mu_j(b^2+\mu_R^2)P_+(ib)}{b\mu_R^2(b+\pi\mu_j)}\right]}{\pi(\frac{1}{2}+\mu_j)\Gamma(\frac{1}{2}+\mu_j)[1-F^2+\pi^2\mu_j^2F^4]}e^{-\pi\mu_j x}\Bigg]. \quad (2.68)$$

By substituting (2.66) and (2.67) into (2.33), the amplitude of the sine wave is given by

$$A = \sqrt{2}F\sqrt{\frac{\left[\sqrt{1-F^2}-\frac{a}{b}P_+(ib)\right]^2+\frac{a^2}{\mu_R^2}P_+(ib)}{F^2+\mu_R^2F^4-1}}.$$

Using Method 2 in Section 2.3.2, and closing the contour in the lower half-plane, $J_+(k)$ is given by

$$J_+(k) = \sum_{n=1}^{\infty}\hat{m}_-(-in\pi)\frac{iF\mu_RT(-in\pi)(2n-2)!}{4^{n-1}(n-1)!^2} = \sum_{n=1}^{\infty}\frac{aiF\mu_RT(-in\pi)(2n-2)!}{(b+n\pi)(k+in\pi)4^{n-1}(n-1)!^2},$$

as,

$$J_-(k) = J(k) - J_+(k),$$

then $J_-(k)$ becomes

$$\begin{aligned} J_-(k) &= \frac{aP_+(k)}{b+ik} - \sum_{n=1}^{\infty}\hat{m}_-(-in\pi)\frac{iF\mu_RT(-in\pi)(2n-2)!}{4^{n-1}(n-1)!^2} \\ &= \sum_{n=1}^{\infty}\frac{aiF\mu_RT(-in\pi)(2n-2)!}{(b+n\pi)(k+in\pi)4^{n-1}(n-1)!^2}. \end{aligned} \quad (2.69)$$

Also, from (2.59) and (2.61),

$$C_0 = \sqrt{1-F^2}(1-\frac{a}{b}) + \sum_{n=1}^{\infty}\frac{aF\mu_RT(-in\pi)(2n-2)!}{(n\pi)(b+n\pi)4^{n-1}(n-1)!^2}. \quad (2.70)$$

and

$$C_1 = -\sum_{n=1}^{\infty}\frac{aiFT(-in\pi)(2n-2)!}{(b+n\pi)\mu_R4^{n-1}(n-1)!^2}. \quad (2.71)$$

Finally, substituting (2.69), (2.70) and (2.71) into (2.32), we find that the shape of the free surface is given by

$$\begin{aligned}\eta_1(x) = \frac{F\sqrt{\pi}}{\mu_R}\Bigg[&\frac{-\cosh(\mu_R)}{\mu_R T(\mu_R)T(-\mu_R)}\mathrm{Re}\Bigg(T(\mu_R)\Gamma(1-\frac{i\mu_R}{\pi})\Gamma(\frac{3}{2}+\frac{i\mu_R}{\pi})\\ &\Bigg[\sqrt{1-F^2}(1-\frac{a}{b})+\sum_{n=1}^{\infty}\frac{aFT(-in\pi)(2n-2)!(\mu_R+in\pi)}{(n\pi)(b+n\pi)4^{n-1}(n-1)!^2}\Bigg]e^{i\mu_R x}\Bigg)\\ &+\sum_{n=1}^{\infty}\frac{\mu_n\mu_R^2F^2T(i\pi\mu_n)\Gamma(\mu_n)}{\pi(\frac{1}{2}+\mu_n)\Gamma(\frac{1}{2}+\mu_n)[1-F^2+\pi^2\mu_n^2F^4]}\\ &\Bigg[\sqrt{1-F^2}(1-\frac{a}{b})+\frac{aFT(-in\pi)(2n-2)!(\mu_R^2-n\pi^2\mu_n)}{(n\pi\mu_R)(b+n\pi)4^{n-1}(n-1)!^2}\\ &+(\frac{\mu_R^2+\pi^2\mu_n^2}{\mu_R^2})\Bigg(\frac{aP_+(-i\pi\mu_n)}{b+\pi\mu_n}-\frac{aF\mu_R T(-in\pi)(2n-2)!}{\pi(b+n\pi)(\mu_n-n)4^{n-1}(n-1)!^2}\Bigg)\Bigg]e^{-\pi\mu_n x}\Bigg].\end{aligned} \tag{2.72}$$

The amplitude of the free surface is then found by substituting (2.70) and (2.71) into (2.33), and is given by

$$A = \sqrt{2}F\sqrt{\frac{\left[\sqrt{1-F^2}(1-\frac{a}{b})+\sum_{n=1}^{\infty}\frac{aF\mu_R T(-in\pi)(2n-2)!}{n\pi(b+n\pi)4^{n-1}(n-1)!^2}\right]^2-\sum_{n=1}^{\infty}\frac{aFT(-in\pi)(2n-2)!}{\mu_R(b+n\pi)4^{n-1}(n-1)!^2}}{F^2+\mu_R^2F^4-1}}.$$

From (2.82), we find the attachment point in this case is

$$\eta_1(0) = -1+\frac{a}{b}, \forall a, b.$$

The next case cannot be treated using either method given in Section 2.3.2.

Case 3:

Here we consider the shape of the stern is given by

$$m(x) = \begin{cases} 0 & \text{if} \quad x < -L \\ a[e^{bx}-e^{-bL}] & \text{if} \quad -L < x < 0 \end{cases},$$

where a, b and L are real and positive. Using the integral in (2.36), we find

$$\hat{m}_-(k) = \frac{a}{b+ik} - \frac{ae^{-L(b+ik)}}{b+ik} - \frac{ae^{-bL}}{ik} + \frac{ae^{-L(b+ik)}}{ik}, \tag{2.73}$$

which is analytic in Im(k) > 0 and has a poles at $k = -in\pi$. By applying Method 2 in Section 2.3.2, we find $J_+(k)$ becomes

$$J_+(k) = \sum_{n=1}^{\infty}\frac{i\mu_R FT(-in\pi)(2n-2)!}{(k+in\pi)4^{n-1}(n-1)!^2}\left[\frac{a[1-e^{-L(b+n\pi)}]}{b+n\pi}+\frac{a[e^{-L(b+n\pi)}-e^{-bL}]}{n\pi}\right].$$

This implies that

$$J_-(k) = \Bigg[-P_+(k)\bigg(\frac{ak[1-e^{-bL}]+ab[e^{-L(b+ik)}-e^{-bL}]}{k(k-ib)}\bigg) \\ -\sum_{n=1}^{\infty}\frac{i\mu_R FT(-in\pi)(2n-2)!}{(k+in\pi)4^{n-1}(n-1)!^2}\bigg[\frac{an\pi[1-e^{-L(b+n\pi)}]+ab[e^{-L(b+n\pi)}-e^{-bL}]}{n\pi(b+n\pi)}\bigg]\Bigg]. \tag{2.74}$$

Also, from (2.59) and (2.61), C_0 and C_1 are equal to:

$$C_0 = \Bigg[\sqrt{1-F^2}\bigg(1+\frac{a(-1+(1+bL)e^{-bL})}{b}\bigg) \\ -\sum_{n=1}^{\infty}\frac{\mu_R FT(-in\pi)(2n-2)!\Big(an\pi[1-e^{-bL}]+ab[e^{-L(b+n\pi)}-e^{-bL}]\Big)}{(n^2\pi^2)(b+n\pi)4^{n-1}(n-1)!^2}\Bigg], \tag{2.75}$$

and

$$C_1 = -\sum_{n=1}^{\infty}\frac{iFT(-in\pi)(2n-2)!\Big(an\pi[1-e^{-bL}]+ab[e^{-L(b+n\pi)}-e^{-bL}]\Big)}{n\pi\mu_R(b+n\pi)4^{n-1}(n-1)!^2}. \tag{2.76}$$

Finally, by substituting (2.74), (2.75) and (2.76) into (2.32), we find that the shape of the free surface is given by

$$\eta_1(x) = \Bigg[\frac{-F\sqrt{\pi}\cosh(\mu_R)}{\mu_R T(\mu_R)T(-\mu_R)}\mathrm{Re}\Bigg(T(\mu_R)\Gamma(1-\frac{i\mu_R}{\pi})\Gamma(\frac{3}{2}+\frac{i\mu_R}{\pi}) \\ \bigg[\sqrt{1-F^2}\bigg(1+\frac{a(-1+(1+bL)e^{-bL})}{b}\bigg) \\ +\sum_{n=1}^{\infty}\frac{F(in\pi-\mu_R)T(-in\pi)(2n-2)!\Big(an\pi[1-e^{-bL}]+ab[e^{-L(b+n\pi)}-e^{-bL}]\Big)}{(n^2\pi^2)(b+n\pi)4^{n-1}(n-1)!^2}\bigg]e^{i\mu_R x}\Bigg) \\ +\sum_{n=1}^{\infty}\frac{\mu_n\mu_R F^3 T(i\pi\mu_n)\Gamma(\mu_n)}{\sqrt{\pi}(\frac{1}{2}+\mu_n)\Gamma(\frac{1}{2}+\mu_n)[1-F^2+\pi^2\mu_n^2F^4]}\bigg[\sqrt{1-F^2}\bigg(1+\frac{a(-1+(1+bL)e^{-bL})}{b}\bigg) \\ +\frac{FT(-in\pi)(2n-2)!\Big(an\pi[1-e^{-bL}]+ab[e^{-L(b+n\pi)}-e^{-bL}]\Big)}{(b+n\pi)4^{n-1}(n-1)!^2}\times \\ \bigg(\frac{\mu_R^2+\pi^2\mu_n^2}{n\pi^2\mu_R(\mu_n-n)}-\frac{\mu_R+n\pi^2\mu_n}{n^2\pi^2}\bigg)\bigg]e^{-\pi\mu_n x}\Bigg]. \tag{2.77}$$

The amplitude of the free surface is given by:

$$\begin{aligned}A = \Bigg[\sqrt{2}F\Bigg[\Bigg(\Bigg(\sqrt{1-F^2}\bigg(1+\frac{a(-1+(1+bL)e^{-bL})}{b}\bigg) \\ -\sum_{n=1}^{\infty}\frac{\bigg(an\pi[1-e^{-bL}]+ab[e^{-L(b+n\pi)}-e^{-bL}]\bigg)\mu_R F T(-in\pi)(2n-2)!}{(n^2\pi^2)(b+n\pi)4^{n-1}(n-1)!^2}\Bigg)^2 \\ +\Bigg(\frac{\bigg(an\pi[1-e^{-bL}]+ab[e^{-L(b+n\pi)}-e^{-bL}]\bigg)F T(-in\pi)(2n-2)!}{n\pi(b+n\pi)4^{n-1}(n-1)!^2}\Bigg)^2\Bigg)\Bigg/(F^2+\mu_R^2F^4-1)\Bigg]^{1/2}\Bigg].\end{aligned} \tag{2.78}$$

From (2.82), the attachment point in this case is given by

$$\eta_1(0) = -1+\frac{a}{b}[1+(bL-1)e^{-bL}],$$

$\forall$ a, b and L.

2.5 Numerical Considerations

The solution for the free surface given in (2.32) is calculated using the same technique presented by McCue and Stump [85], using the Maple 12 programming language. We start with the imaginary roots of the function $f_1(k)$ defined in (2.45), and by performing a Taylor expansion, we find μ_n is given by

$$\mu_n = n+\frac{1}{2}-\frac{1}{\pi^2F^2n^2}+O(n^{-3}) \quad \text{as} \quad n\to\infty. \tag{2.79}$$

Following McCue and Stump, the infinite product $T(k)$, given by (2.48), for the real roots $k=\pm\mu_R$ can be written as

$$T(\mu_R) = \exp\left(\sum_{n=1}^{N}\log\left[\frac{\mu_n - i\mu_R/\pi}{(n+\frac{1}{2})-i\mu_R/\pi}\right]-\sum_{n=N+1}^{\infty}\left[\frac{-1}{\pi^2F^2n^2}+\frac{1-i\mu_R/\pi}{\pi^2F^2n^3}\right]\right). \tag{2.80}$$

This product is computed for different values of N, for the first N terms as shown in Table B.2, and in Table B.3 the infinite product is computed for $n > N$. For a fixed values of N the accuracy of the approximation increases as the Froude number F increase.

The infinite product $T(k)$ for the imaginary roots $k = \pm i\pi\mu_n$ can be written as

$$T(i\pi\mu_m) = \exp\left[\sum_{n=1}^{N} \log\left(1 + \frac{\mu_n - (n+1/2)}{\mu_m + (n+1/2)}\right) - \frac{-1}{\pi^2 F^2 (N+1)} + \frac{1+\mu_m}{\pi^2 F^2 (N+1)^2}\right]. \tag{2.81}$$

The calculation of this product is shown in Table B.4 for different values of m (for more details see [85]).

2.6 Results

The problem of the linearised free surface flow from the edge of a semi-infinite curved plate in a fluid of finite depth has been solved using the Wiener–Hopf technique in the case of subcritical flows, (for a Froude number $F < 1$). The free surface in (2.32) consists of a sinusoidal component and a monotonically decaying portion. The data in Appendix B, Tables B.2-B.1, show that the location of the free surface, given by (2.32), can be computed accurately to seven decimal places for the case of the flat plate.

In Section 2.4, three families of plate shapes were described. We employ this family of plate shapes to show the effect of these shapes of eliminating or minimising the waves downstream. In Case 1, the free surface profiles are shown in Figure 2.3, for the case of the flat plate given by (2.62), for $F = 0.5$ and $F = 0.7$. The second part of the free surface in (2.62) is an exponentially decaying term, as $x \to \infty$, and effects the height of the first wave crest; so after one wave length the free surface profiles are sinusoidal. These Figures are also drawn by McCue and Stump ([85], 2000) with the same scales.

As it is clearly seen from figure 2.3(b), the free surface detaches smoothly from the plate and the position of the point of separation between the stern and the free surface is given by

$$\eta_1(0) = -1 + \int_{-\infty}^{0} m(x)dx. \tag{2.82}$$

The relation between the Froude number F and the wavelength λ is shown in Figure 2.4. We note that, as $F \to 1$, the wavelength $\lambda \to \infty$, as indicated by the dashed line. Also, as $F \to 0$, the wavelength behaves like $\lambda \sim 2\pi F^2$, as indicated by the solid line. The distance between the height of the plate and the undisturbed free surface $\epsilon \approx P/(1 - F^2) << 1$ is very small, and thus we obtain linear waves, and in this case, from linear water wave theory, the wavelength is given by the dispersion relation $F^2 = \tanh(k)/k$ where $k = 2\pi/\lambda$, independent of ϵ and dependent on F. But if ϵ is of order one, we obtain nonlinear waves and here the wavelength is weakly depend on ϵ, and strongly dependent on the Froude number F.

In Case 2, Section 2.4, the free surface profiles are calculated using the two Methods given by (2.68) and (2.72) as shown in Figure 2.5 for different Froude numbers $F = 0.5$ (Figure 2.5(a)) and $F = 0.7$ (Figure 2.5(b)). The free surface detaches from the curved plate at $\eta_1(0) = -0.5$, where the values $a = 1$ and $b = 2$ are chosen. Figure 2.6 shows the relation between the amplitude A and the parameters a and b in Figure 2.6(a) and 2.6(b), respectively. The free surface for the local minimum of a and b are shown in Figure 2.6(c) and 2.6(d), respectively. We note that by increasing the slope of the plate the amplitude decreases to a minimum and then increases again. In Figure 2.7 the free surface profiles are shown for different families of the stern at $F = 0.5$, $b = 1$ and different values of a, namely $a = 0$, 0.5, 1 and 1.5. For a fixed value of a and different values of b, the free surface profiles are the same shape, only stretched in the y-direction.

In Case 3, Section 2.4, the slope of the plate is continuous for all $x < 0$. this shape is chosen to illustrate the behavior of the solution for plate shapes whose slopes are monotonically increasing in x. The free surface profiles are shown in Figure 2.8(a), where $F = 0.5$, $a = 1$, $b = 2$, and $L = 3$ using the second method given by (2.77). The detachment point between the curved plate and the free surface is $\eta_1(0) = -0.5$. Figure 2.8(b) shows the relation between the parameter a and the amplitude A for different values of $b = 1$, 2, 3, and $L = 1$. By increasing the values of a up to the local minimum, $a = 2.9$, 3.2, 3.3, the amplitude A decreases and after that the amplitude increases with increasing a.

Figure 2.8(c) shows that, when we increase the parameter b, the amplitude decreases to a local minimum $b = 1.8$, 1.8, 1.3, for $a = 1$, 2, and 3 and $L = 1$ respectively, and then the amplitude slightly increases as we increase b until we have the same amplitude. Figure 2.8(d), shows the relation between the amplitude A and the parameter L for different scales, where $a = -0.5$, 0, 0.5, 1, with $b = 1$. The amplitude decreases when we increase the parameter L up to the local minimum $L = 6$, 6.2, 6.3, 8 for $a = -0.5$, 0, 0.5, 1 and $b = 1$, respectively, and then the amplitude slightly increases to become stable. We conclude that for a fixed value of a and different values of b and L, the results are qualitatively similar.

In conclusion, when we increase the slope of the plate up to critical points, the amplitude decreases. It is at these critical points we find the optimal stern shape that can minimise the waves.

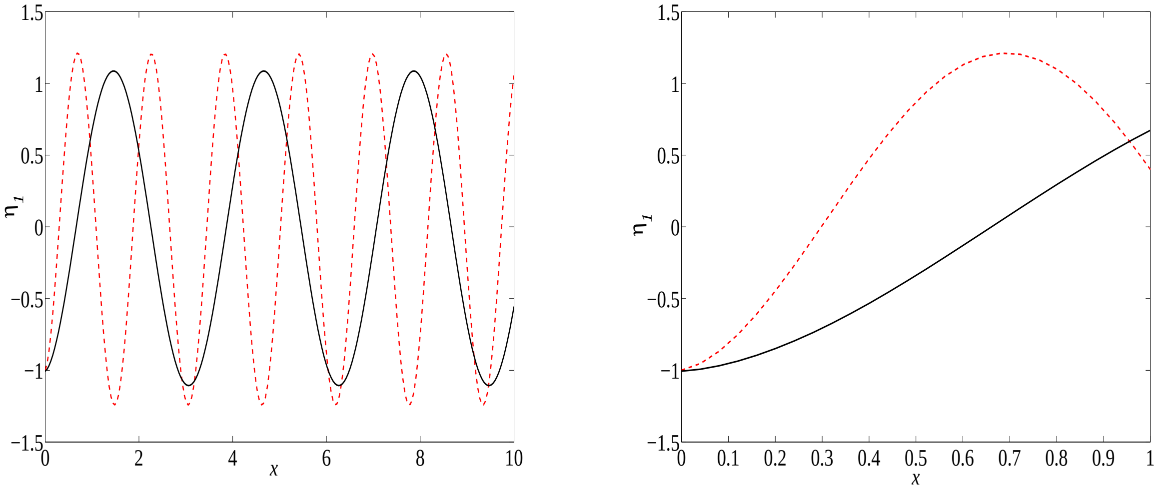

(a) (b)

FIGURE 2.3: Free surface profiles drawn for flat plate shapes given by (2.62) for different scales, with $F = 0.5$(red), and $F = 0.7$(black) by using Method 1 in Section 2.3.2. These figures are presented exactly by McCue and Stump [85] on the same scale.

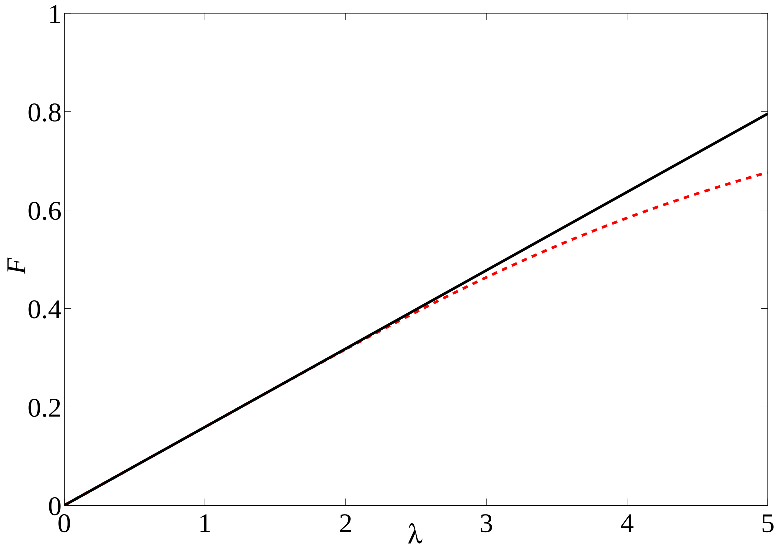

FIGURE 2.4: The dependence of the wavelength λ on the Froude number F. The red dashed is computed using dispersion relation and the black solid line is the asymptotic line.

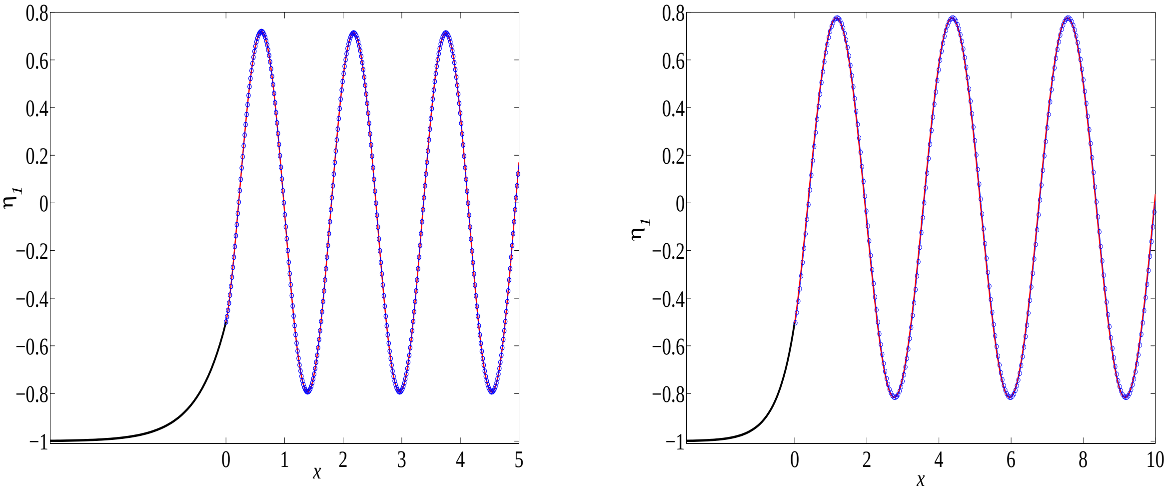

(a) (b)

FIGURE 2.5: Free surface profiles drawn for the plate shape in Case 2 given by (2.64), with $F = 0.5$, $a = 1$ and $b = 2$ (Figure (a)) and $F = 0.7$, $a = 1$ and $b = 2$ (Figure (b)), by using Method 1 (circles) and Method 2 (solid-line) as given by (2.68) and (2.72), respectively, in Section 2.3.2.

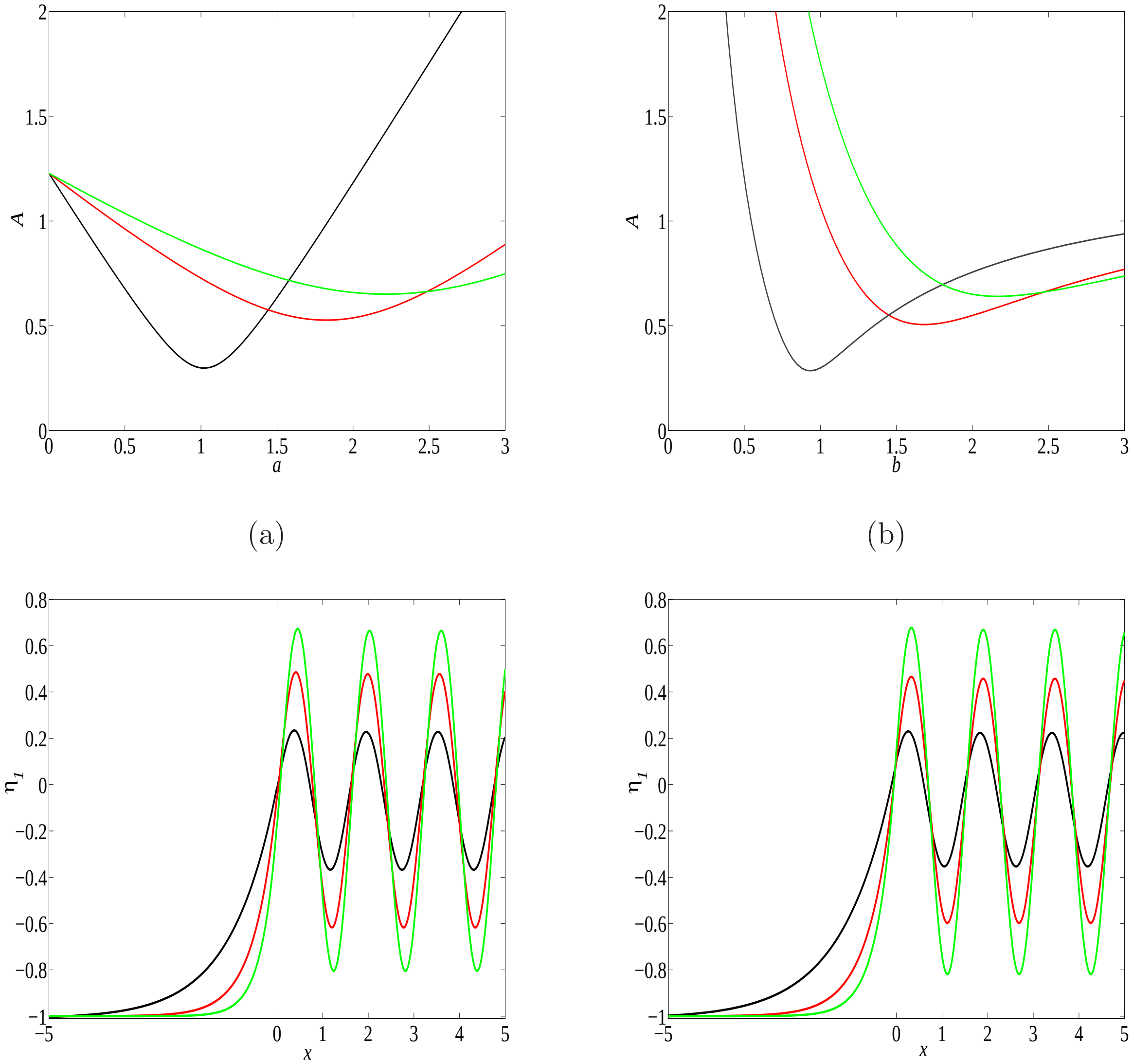

(a) (b)

(c) (d)

FIGURE 2.6: Figures (a) and (b) show the dependence of the amplitude A on the parameter a with $b = 1$(black), 2(red), 3(green), and the dependence of the amplitude A on b for $a = 1$(black), 2(red), 3(green), for $F = 0.5$, respectively, for the plate shape given by (2.64). Figure (c) shows the free surface for the local minimum of the parameter a, $(a = 1, b = 1, A = 0.298)$(black), $(a = 1.9, b = 2, A = 0.549)$(red), $(a = 2.5, b = 3, A = 0.73)$(green). Figure (d) shows the free surface for the local minimum of the b, $(a = 1, b = .9, A = 0.289)$(black), $(a = 2, b = 1.8, A = 0.529)$(red), $(a = 3, b = 2.6, A = 0.749)$(green).

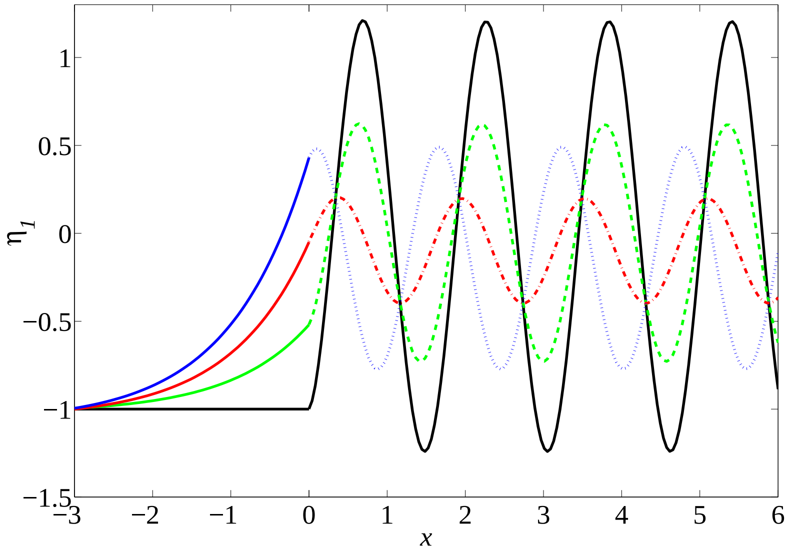

FIGURE 2.7: Free surface profile drawn for the plate shape (2.64) with $F = 0.5$ and $a = 0$(solid black), 0.5(green dashed), 1(red dot-dashed), 1.5((blue dot)) and $b = 1$.

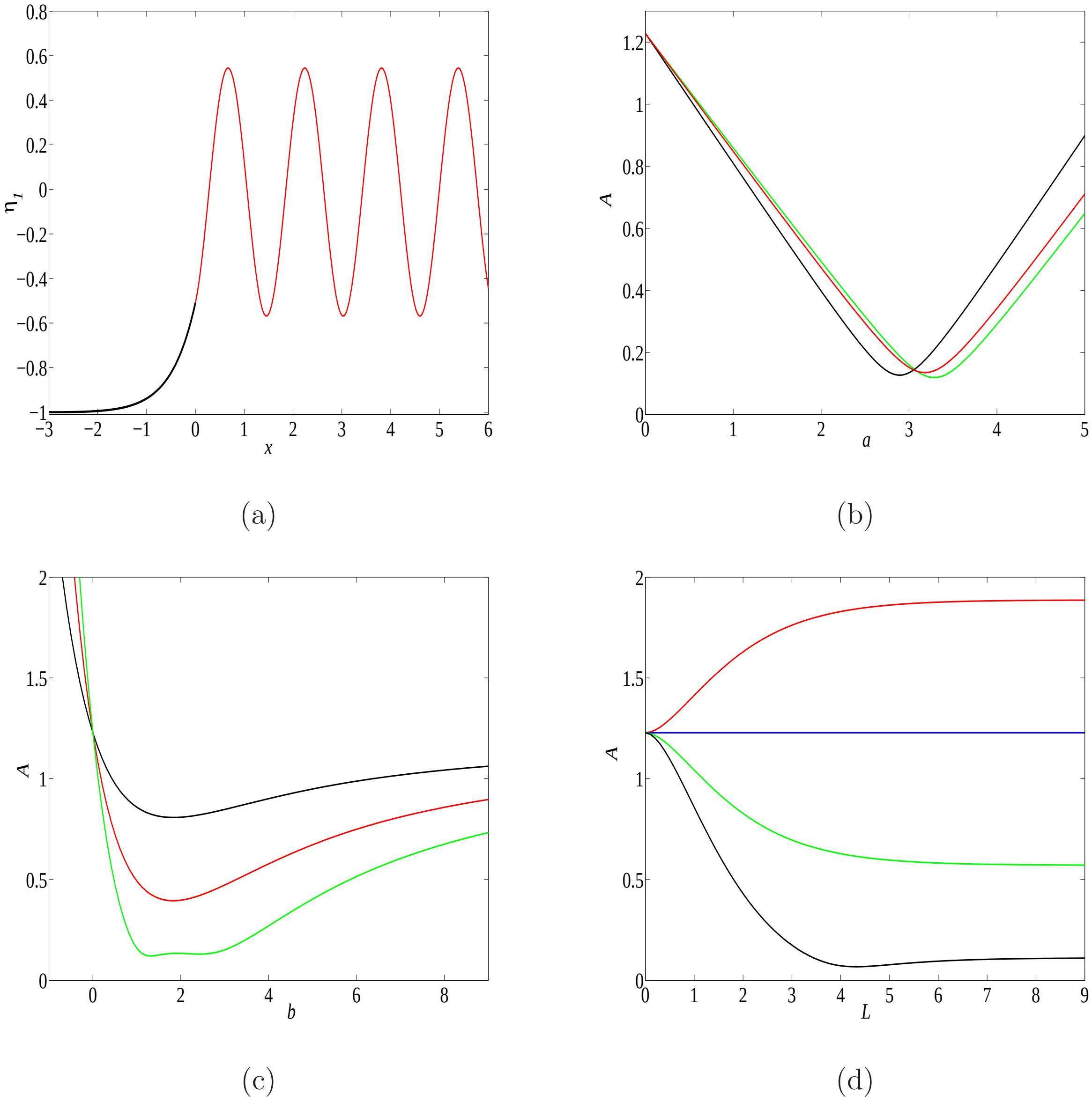

(a)

(b)

(c)

(d)

FIGURE 2.8: In figure (a), Free surface profiles are drawn for the plate shape in Case 3 given by (2.77), with $F = 0.5$, $a = 1$, $b = 2$, $L = 3$, using Method 1 in Section 2.3.2. In figures (b), (c) and (d) the dependence of the wave amplitude A on the parameters a, b and L respectively, with $F = 0.5$, $b = 1$(black), 2(red), 3(blue) and $L = 1$ in figure (a), $a = 1$(black), 2(red), 3(green) and $L = 1$ in figure (b) and $a = -0.5$(red), 0(blue), 0.5(green), 1(black) and $b = 1$ in figure (c).

Chapter 3

Numerical Solution to the Fully Nonlinear Steady Problem

3.1 Introduction

After solving the problem by the Wiener–Hopf technique analytically, the same problem will be solved numerically using the boundary integral equation method.

We consider a two-dimensional flow past a semi-infinite plate in a fluid of finite depth, such that the free surface separates from the end of the curved plate BC, as shown in figure 3.1. The stern flow separates tangentially from the edge of the plate. Furthermore, we assume that the fluid is inviscid and incompressible, and that the flow is steady and irrotational. This problem has been considered by many authors. For instance, McCue and Forbes [82] and Maleewomg and Grimshaw [71] solved the problem numerically using the boundary integral method for the case of the flat plate. Recently, Binder [11] solved the same problem numerically, using the same technique, for the case of a curved plate.

3.2 Problem Formulation

We consider two-dimensional flow past a semi-infinite plate in a fluid of finite depth, assuming that the stern flow separates tangentially from the edge of a curved plate. The fluid far upstream is taken to be uniform, with a constant depth h and speed V. The configuration of the flow examined in this work is presented in figure 3.1.

A Cartesian coordinate system is introduced so that the x-axis lies at the bottom of the plate and the y-axis points vertically upwards (x and y are used in this chapter instead of $\tilde{x}$ and $\tilde{y}$ for easy notation). The plane geometry consists of the free surface from the separation point C, extending into the far field D as $x \to \infty$, and three solid boundaries: a horizontal flat plate AB, located at $y = h$, and $-\infty < x < x_B$; a horizontal bottom boundary EF, located at $y = 0$, $-\infty < x < \infty$; and a curved BC at $x_B < x < 0$. The dimensionless boundary condition is given by

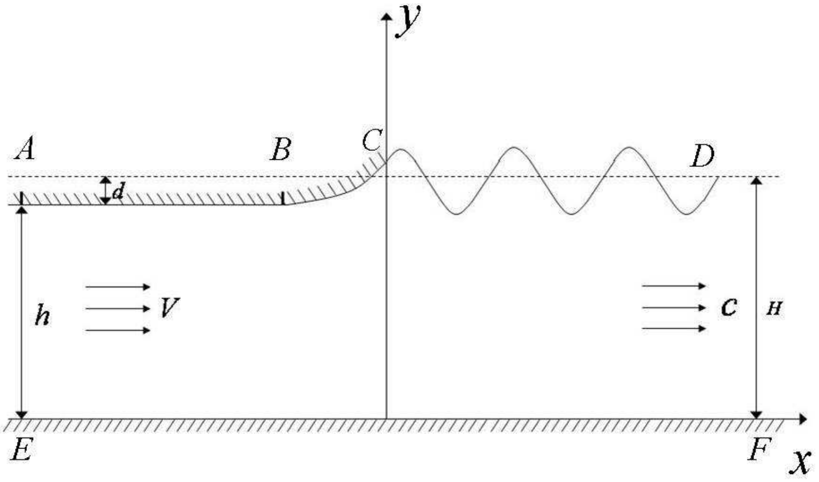

Figure 3.1: Sketch of the flow and the position of the coordinates

$$v = 0 \quad \text{on} \quad y = 0, \quad -\infty < x < \infty, \tag{3.1}$$

$$v = u\frac{\partial \eta}{\partial x} \quad \text{on} \quad y = 1 + \eta(x), \quad -\infty < x < \infty, \tag{3.2}$$

An additional boundary condition from Bernoulli's equation along the free surface $y = \eta(x)$, gives

$$\frac{1}{2}F^2(u^2 + v^2) + y = \frac{1}{2}F^2 + 1 + P, \quad \text{on} \quad y = 1 + \eta(x), \tag{3.3}$$

where P is not a constant for $x < 0$. $u \sim 1$ as $x \to \infty$, the Froude number is $F = \frac{V}{\sqrt{gh}}$.

3.2.1 Conformal Mapping

In the conformal mapping method, the stream function ψ and potential function ϕ satisfy

$$\frac{\partial \phi}{\partial x} = \frac{\partial \psi}{\partial y} \qquad \text{and} \qquad \frac{\partial \phi}{\partial y} = -\frac{\partial \psi}{\partial x}. \tag{3.4}$$

As the stream function ψ is a constant along the free surface, we introduce a complex function f analytic over $z = x + iy$, given by

$$f = \phi + i\psi. \tag{3.5}$$

The stern flow problem exhibits complicated geometries in the Cartesian z-plane, as shown in figure 3.1. Thus, we simplified the problem in the f-plane, by transforming from the (x, y)-plane to the (ϕ, ψ)-plane, as shown in figure 3.2(for more details see [11]).

By choosing $\phi = 0$ at the separation point C, $\psi = 0$ along the streamline $ABCD$, and $\psi = -1$ on the bottom (EF), then the fluid region, is within, $-1 < \psi < 0$ and $-\infty < \phi < \infty$. Finally, the kinematic boundary conditions (3.1) and (3.2) can be written in the f-plane as:

$$v = 0 \quad \text{on} \quad EF, \tag{3.6}$$

$$v = 0 \quad \text{on} \quad AB. \tag{3.7}$$

The boundary condition (3.2) can not be expressed in the f-plane, because the objective is to derive an integral relation that only involves unknowns that are on the free surface, and this can not be done in the f-plane. However it can be done by using first the conformal mapping

$$\zeta = \alpha + i\beta = e^{-\pi f} = e^{-\pi(\phi + i\psi)} = e^{-\pi\phi}(\cos(\pi\psi) - i\sin(\pi\psi)). \tag{3.8}$$

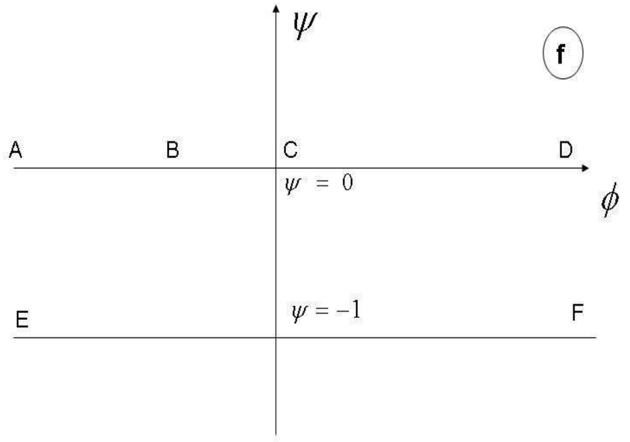

FIGURE 3.2: This figure shows the flow in the complex f-plane.

z - plane (x,y)	f-plane (ϕ,ψ)
$A(-\infty, 1)$	$\phi = \phi_A = -\infty$, $\psi = 0$
$B(1, x_B)$	$\phi = \phi_B < 0$, $\psi = 0$
$C(x_B, 0)$	$\phi = \phi_C = 0$, $\psi = 0$
$D(0, \infty)$	$\phi = \phi_D = \infty$, $\psi = 0$
$E(-\infty, 0)$	$\phi = \phi_E = -\infty$, $\psi = -1$
$F(0, \infty)$	$\phi = \phi_F = \infty$, $\psi = -1$

TABLE 3.1: The coordinates of key points in the f-plane.

z - plane (x,y)	f-plane (ϕ,ψ)	ζ - plane (α,β)
$A(-\infty, 1)$	$\phi = \phi_A = -\infty$, $\psi = 0$	$\alpha = \alpha_A = \infty, \quad \beta = 0$
$B(1, x_B)$	$\phi = \phi_B < 0$, $\psi = 0$	$\alpha = \alpha_B > 1, \quad \beta = 0$
$C(x_B, 0)$	$\phi = \phi_C = 0$, $\psi = 0$	$\alpha = \alpha_C = 1, \quad \beta = 0$
$D(0, \infty)$	$\phi = \phi_D = \infty$, $\psi = 0$	$\alpha = \alpha_D = 0, \quad \beta = 0$
$E(-\infty, 0)$	$\phi = \phi_E = -\infty$, $\psi = -1$	$\alpha = \alpha_E = -\infty, \quad \beta = 0$
$F(0, \infty)$	$\phi = \phi_F = \infty$, $\psi = -1$	$\alpha = \alpha_F = 0, \quad \beta = 0$

TABLE 3.2: The mapping between the $z-$, $f-$ and $\zeta-$planes

In the ζ-plane, the curved plate BC and the free surface CD are mapped to the positive real axis, while the bottom boundary EF is mapped to the negative real axis. In addition, the streamlines in the fluid are mapped to the region $-\infty < \alpha < \infty$ and $\beta \geq 0$, as shown in figure 3.3. Table 3.1 has been extended to include the image of the point in the ζ-plane, as shown in Table 3.2.

Complex velocity components, $u - iv$, are introduced in terms of the potential ϕ and the stream function ψ in (3.4), given by

$$u - iv = \frac{\partial \phi}{\partial x} + i\frac{\partial \psi}{\partial x} = \frac{df}{dz}. \tag{3.9}$$

The components u and v in (3.3) can be re-written by applying the new complex function related to the complex velocity given by

$$u - iv = e^{\tau - i\theta}. \tag{3.10}$$

as

$$u^2 + v^2 = e^{2\tau}(\cos^2\theta + \sin^2\theta) = e^{2\tau}. \tag{3.11}$$

Substituting (3.11) into (3.3), we obtain

$$\frac{F^2}{2}e^{2\tau} + y = \frac{F^2}{2} + 1 + P \quad \text{on the free surface,} \quad CD, \tag{3.12}$$

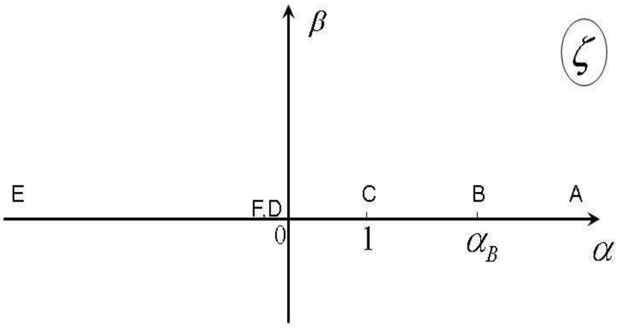

FIGURE 3.3: This figure shows the flow in the complex ζ-plan.

where P is a constant. From (3.2) and (3.10), we defined the shape of the curved plate as

$$\frac{\partial \eta}{\partial x} = \tan(\theta) = M(x) \quad \text{on} \quad BC. \tag{3.13}$$

Additionally, the free surface profile can be determined by integrating the identity

$$\frac{\partial x}{\partial \phi} + i\frac{\partial y}{\partial \phi} = e^{-\tau}\cos\theta + ie^{-\tau}\sin\theta, \tag{3.14}$$

and by integrating the imaginary parts of (3.14). Using $\alpha = e^{-\pi\phi}$, we find that

$$y(\alpha) = -\frac{1}{\pi}\int_0^{\alpha} \frac{e^{-\tau}\sin\theta}{\alpha} d\alpha + y(C), \qquad 0 < \alpha < 1. \tag{3.15}$$

Finally, the kinematic boundary conditions (3.6) and (3.7) are mapped to the ζ-plane to become

$$\theta = 0 \quad \text{for} \quad \alpha > \alpha_B \quad \text{and} \quad \beta = 0 \tag{3.16}$$

and

$$\theta = 0 \quad \text{for} \quad \alpha < 0 \quad \text{and} \quad \beta = 0. \tag{3.17}$$

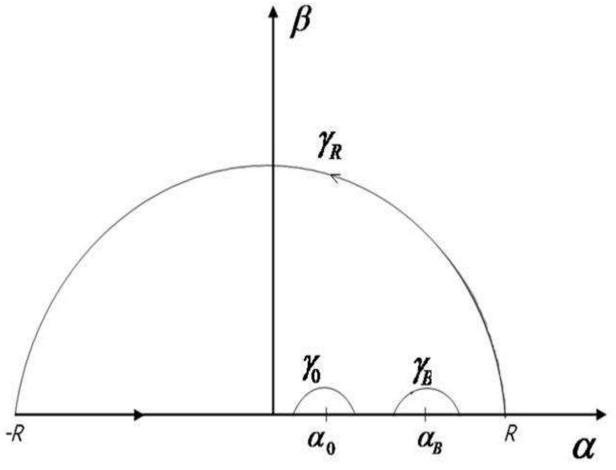

FIGURE 3.4: This figure shows the complex ζ-plane on the contour γ.

3.2.2 Boundary Integral equation

In this section, we will use the boundary integral method to derive an integral relation between τ and θ on the free surface. In the ζ-plane, as shown in figure 3.4, a contour integral is given by

$$\oint_{\gamma} \frac{\tau(\alpha,\beta) - i\theta(\alpha,\beta)}{\zeta - \alpha_0} d\zeta, \tag{3.18}$$

where $0 < \alpha_0 < 1$, is a mapped point on the free surface. The path γ consists of a large semi-circular arc of radius R, centred at the origin, and the real axis with a circular indentation of radius r about the point α_0 and a circular indentation about the point α_B. See Figure 3.4. Therefore, breaking up the contour into its components, (3.18) becomes

$$\begin{aligned} \oint_{\gamma} \frac{\tau(\alpha,\beta) - i\theta(\alpha,\beta)}{\zeta - \alpha_0} d\zeta &= \int_{\gamma_R} \frac{\tau(\alpha,\beta) - i\theta(\alpha,\beta)}{\zeta - \alpha_0} d\zeta + \int_{\gamma_0} \frac{\tau(\alpha,\beta) - i\theta(\alpha,\beta)}{\zeta - \alpha_0} d\zeta \\ &+ \int_{-R}^{R} \frac{\tau(\alpha,0) - i\theta(\alpha,0)}{\alpha - \alpha_0} d\alpha + \int_{\gamma_B} \frac{\tau(\alpha,\beta) - i\theta(\alpha,\beta)}{\zeta - \alpha_0} d\zeta. \end{aligned} \tag{3.19}$$

It should be noted that there is no contribution made by the integral by γ_B, because it is a logarithmic singularity which is weaker than a pole. Cauchy's theorem states that along any closed contour not enclosing a singularity of an analytic, a single-valued function is equal to zero. Since γ does not enclose any singularity, then (3.19) becomes:

$$\int_{\gamma_R} \frac{\tau(\alpha,\beta)-i\theta(\alpha,\beta)}{\zeta-\alpha_0}d\zeta+\int_{\gamma_0} \frac{\tau(\alpha,\beta)-i\theta(\alpha,\beta)}{\zeta-\alpha_0}d\zeta+\int_{-R}^{R} \frac{\tau(\alpha,0)-i\theta(\alpha,0)}{\alpha-\alpha_0}d\alpha=0. \tag{3.20}$$

Integrating (3.20) separately, starting with γ_0, it can be simplified further.

Let $\zeta=\alpha_0+re^{i\kappa}$, so $d\zeta=ire^{i\kappa}d\kappa$. Then

$$\begin{aligned}\int_{\gamma_0} \frac{\tau(\alpha,\beta)-i\theta(\alpha,\beta)}{\zeta-\alpha_0}d\zeta &= \int_{\pi}^{0} \frac{\tau(\alpha_0+r\cos\kappa,r\sin\kappa)-i\theta(\alpha_0+r\cos\kappa,r\sin\kappa)}{re^{i\kappa}}ire^{i\kappa}d\kappa \\ &= \int_{\pi}^{0}[\tau(\alpha_0+r\cos\kappa,r\sin\kappa)-i\theta(\alpha_0+r\cos\kappa,r\sin\kappa)]id\kappa. \end{aligned}\tag{3.21}$$

As $r\to 0$, this implies that

$$\int_{\pi}^{0}[\tau(\alpha_0,0)-i\theta(\alpha_0,0)]id\kappa=-i\pi[\tau(\alpha_0,0)-i\theta(\alpha_0,0)]. \tag{3.22}$$

Substituting this into (3.20), gives

$$[\tau(\alpha_0,0)-i\theta(\alpha_0,0)]=\frac{1}{i\pi}\int_{\gamma_R} \frac{\tau(\alpha,\beta)-i\theta(\alpha,\beta)}{\zeta-\alpha_0}d\zeta+\frac{1}{i\pi}\int_{-R}^{R} \frac{\tau(\alpha,0)-i\theta(\alpha,0)}{\alpha-\alpha_0}d\alpha. \tag{3.23}$$

As $R\to\infty$, the second integral on the right hand side of (3.23) becomes

$$\lim_{R\to\infty}\frac{1}{\pi i}\int_{-R}^{R} \frac{\tau(\alpha,0)-i\theta(\alpha,0)}{\alpha-\alpha_0}d\alpha=\frac{1}{\pi i}\int_{-\infty}^{\infty} \frac{\tau(\alpha,0)-i\theta(\alpha,0)}{\alpha-\alpha_0}d\alpha. \tag{3.24}$$

It can be seen from (3.8) as $\phi\to-\infty$, the flow becomes a horizontal uniform stream, with velocity non-dimensionalised to 1, this means $u-iv\to 1$. From (3.10) it implies that $\tau-i\theta\to 0$, therefore the limit of the first integral in the right hand side of (3.23), as $R\to\infty$ is

$$\lim_{R\to\infty}\quad \frac{1}{\pi i}\int_{\gamma_R} \frac{\tau(\alpha,\beta)-i\theta(\alpha,\beta)}{\zeta-\alpha_0}d\zeta=0. \tag{3.25}$$

Now, we reduce the integral in (3.18) to

$$[\tau(\alpha_0, 0) - i\theta(\alpha_0, 0)] = \frac{1}{\pi i}\int_{-\infty}^{\infty} \frac{\tau(\alpha, 0) - i\theta(\alpha, 0)}{\alpha - \alpha_0} d\alpha. \tag{3.26}$$

By taking the real and imaginary parts of (3.26) we obtain

$$\tau(\alpha_0) = -\frac{1}{\pi}\int_{-\infty}^{\infty} \frac{\theta(\alpha)}{\alpha - \alpha_0} d\alpha, \tag{3.27}$$

and

$$\theta(\alpha_0) = \frac{1}{\pi}\int_{-\infty}^{\infty} \frac{\tau(\alpha)}{\alpha - \alpha_0} d\alpha, \tag{3.28}$$

where $\theta(\alpha) = \theta(\alpha, 0)$ and $\tau(\alpha) = \tau(\alpha, 0)$. Here we choose (3.27) to obtain the integral relation between τ and θ on the free surface.

The boundary conditions (3.16) and (3.17) can be used to simplify (3.27) into four parts to give

$$-\frac{1}{\pi}\int_{-\infty}^{\infty} \frac{\theta(\alpha)}{\alpha - \alpha_0} d\alpha = -\frac{1}{\pi}\Bigg[\int_{-\infty}^{0} \frac{\theta(\alpha)}{\alpha - \alpha_0} d\alpha + \int_{0}^{1} \frac{\theta(\alpha)}{\alpha - \alpha_0} d\alpha \quad + \\ \int_{1}^{\alpha_B} \frac{\theta(\alpha)}{\alpha - \alpha_0} d\alpha + \int_{\alpha_B}^{\infty} \frac{\theta(\alpha)}{\alpha - \alpha_0} d\alpha\Bigg].$$

Applying (3.16) and (3.17), we find that the first and last integral on the right equate to zero. Thus, we may write (3.27) as

$$\tau(\alpha_0) = -\frac{1}{\pi}\int_{0}^{1} \frac{\theta(\alpha)}{\alpha - \alpha_0} d\alpha - \frac{1}{\pi}\int_{1}^{\alpha_B} \frac{\theta(\alpha)}{\alpha - \alpha_0} d\alpha. \tag{3.29}$$

Using (3.8) and the fact that $\psi = 0$ along the free surface, we have

$$\alpha = e^{-\pi\phi} \tag{3.30}$$

We perform a change of variable by substituting (3.30) into (3.29) to give

$$\tau(\phi_0) = -\int_{0}^{\infty} \frac{\theta(\phi)e^{-\pi\phi}}{e^{-\pi\phi} - e^{-\pi\phi_0}} d\phi + \int_{0}^{\phi_B} \frac{\theta(\phi)e^{-\pi\phi}}{e^{-\pi\phi} - e^{-\pi\phi_0}} d\phi, \tag{3.31}$$

where $\tau(\phi_0) = \tau(e^{-\pi\phi_0})$, $\theta(\phi) = \theta(e^{-\pi\phi})$ and $\phi_B = e^{-\pi\phi_B}$. The function, $\theta(\phi)$, in the second integral of the right hand side is a known function for the curved plate BC.

Equations (3.12), (3.15) and (3.31) define a nonlinear integral equation for the unknown function $\theta(\phi)$ on the free surface.

3.2.3 Numerical Procedure

A numerical procedure is used to calculate the solution to the nonlinear integral equation derived in Section 3.31. This integral equation is used to calculate τ along the curved plate and the free surface $ABCD$ in terms of θ. In order to calculate τ, it is necessary to have a discrete point ϕ_0, along the free surface and the plate at which the τ values may be evaluated. This is done by defining an equally spaced mesh on the curved plate and the free surface, $\phi_B < \phi < \infty$, given by

$$\phi_j = \phi_{j-1} + h_j, \quad j = 1, .., N_1, \tag{3.32}$$

and

$$\phi_j^* = \phi_{j-1}^* + h_j^*, \quad j = 1, .., N_2, \tag{3.33}$$

where $h_j = -\phi_B/N_1$ is the distance between consecutive mesh points on the free surface, and $h_j^* = L/N_2$ is the distance between consecutive mesh points on the curved plate. We define $N = N_1 + N_2$ to be the total number of mesh points.

It can be seen from the integral part of (3.31) that, for each mesh point, there would be a singularity in the integrand, to avoid this singularity, it is necessary to introduce midpoints, at which τ may be calculated, as follows

$$\phi_{I+\frac{1}{2}} = \frac{\phi_{I-1} + \phi_I}{2} \qquad I = 1, .., N_1, \tag{3.34}$$

and

$$\phi_{I+\frac{1}{2}}^* = \frac{\phi_{I-1}^* + \phi_I^*}{2} \qquad I = 1, .., N_2. \tag{3.35}$$

The integral in (3.31) is approximated by applying the trapezoidal rule, with a summation over the midpoints $\phi_{I+\frac{1}{2}}$ to give

$$\tau_{I+\frac{1}{2}} = -\sum_{j=1}^{N_1} \frac{\theta(\phi_j) e^{-\pi\phi_j} h_j}{e^{-\pi\phi_j} - e^{-\pi\phi_{I+\frac{1}{2}}}} \omega_j - \sum_{j=1}^{N_2} \frac{\theta(\phi_j^*) e^{-\pi\phi_j^*} h_j^*}{e^{-\pi\phi_j^*} - e^{-\pi\phi_{I+\frac{1}{2}}^*}} \omega_j, \quad I = 1.., N, \tag{3.36}$$

where ω_j is the weight of the trapezoidal rule. Next, we evaluate $y_I = y(\phi_I)$ at the midpoints by rewriting (3.15) as

$$y(\phi) = y(0) + \int_0^{\phi} e^{-\tau(\phi_0)} \sin\theta(\phi_0) d\phi_0, \tag{3.37}$$

where $y(\phi) = y(e^{-\pi\phi})$, $\tau(\phi_0) = \tau(e^{-\pi\phi_0})$ and $\theta(\phi_0) = \theta(e^{-\pi\phi_0})$.

By applying the trapezoidal rule to (3.37), with $y(0) = 1$, we obtain

$$y_I = y_{I-1} + e^{-\tau_{I+\frac{1}{2}}} \sin\theta(\phi_{I+\frac{1}{2}})\Delta, \quad I = 1, .., N. \tag{3.38}$$

Finally, we calculate θ_I on the curved plate from (3.13), which is given by

$$\tan(\theta_I) - M(x_I) = 0 \quad \text{for} \quad I = 1.., N_2. \tag{3.39}$$

Now, we rewrite equations (3.12), (3.36) and (3.38) as

$$\frac{F^2}{2} e^{2\tau_{I+\frac{1}{2}}} + y_I = \frac{F^2}{2} + 1 + P, \quad I = 1.., N, \tag{3.40}$$

$$y_I = y_{I-1} + e^{-\tau_{I+\frac{1}{2}}} \sin(\theta_{I+\frac{1}{2}})\Delta, \quad I = 1.., N, \tag{3.41}$$

$$\tau_{I+\frac{1}{2}} = -\sum_{j=1}^{N1} \frac{\theta(\phi_j)e^{-\pi\phi_j} h_j}{e^{-\pi\phi_j} - e^{-\pi\phi_{I+\frac{1}{2}}}}\omega_j - \sum_{j=1}^{N2} \frac{\theta(\phi_j^*)e^{-\pi\phi_j^*} h_j^*}{e^{-\pi\phi_j^*} - e^{-\pi\phi_{I+\frac{1}{2}}^*}}\omega_j, \quad I = 1.., N. \tag{3.42}$$

By substituting (3.41) and (3.42) into (3.40), evaluated at the midpoints given by (3.34) and (3.35), a system of N nonlinear equations in N unknowns is obtained, for θ_I for $I = 1, ..N_1$ on the free surface and θ_I^* for $I = N_1 + 1..N_2$ on the curved plate.

Having derived the system of nonlinear equations (3.40), (3.41) and (3.42) in terms of θ. we employ Newton's method to solve this system of equations (see Hoffman [43], Ellis [93]). Newton's method is one of the most well known procedures in numerical analysis. A system of $N_1 + N_2$ nonlinear equations with $N_1 + N_2$ unknowns has been derived. Solving this system is describe below.

From equation (3.39) and Bernoulli's relation (3.40), we have the N coordinate functions

$$Y_I = \tan(\theta_I) - M(x_I) \quad \text{for} \quad I = 1.., N_1. \tag{3.43}$$

and

$$Ys_I = \frac{F^2}{2} e^{2\tau_{I+\frac{1}{2}}} + y_I - \frac{F^2}{2} - (1 + P) \quad \text{for} \quad I = N_1 + 1.., N_2, \tag{3.44}$$

This system can be rewritten as

$$Y_1(\theta_1, ..., \theta_{N_1}, \theta_{N_1+1}^*, ..., \theta_{N_2}^*) = 0.$$

$$Y_2(\theta_1, ..., \theta_{N_1}, \theta_{N_1+1}^*, ..., \theta_{N_2}^*) = 0.$$

$$\vdots$$

$$Y_{N_2}(\theta_1, ..., \theta_{N_1}, \theta^*_{N_1+1}, ..., \theta^*_{N_2}) = 0. \tag{3.45}$$

Newton's method is an efficient iterative method for estimating solutions to the system of nonlinear equations.

The technique employed to generate the free surface profile that will be presented in the next section, after we solved this system to find the unknown θ_I on the plate and the free surface.

3.2.4 Free Surface Profiles

In this section the free surface $y = 1 + \eta(x)$ for $x > 0$ is parameterised by writing $x = x(\phi)$, $y = y(\phi)$ with $\phi > 0$, so that

$$\frac{dx}{d\phi} + i\frac{dy}{d\phi} = e^{-\tau+i\theta}. \tag{3.46}$$

By taking the real and imaginary parts of (3.14) to write

$$\frac{\partial x}{\partial \phi} = e^{-\tau}\cos\theta \qquad \text{and} \qquad \frac{\partial y}{\partial \phi} = e^{-\tau}\sin\theta. \tag{3.47}$$

Also, the shape of the plate is calculated using (3.47) and (3.13) to give

$$\frac{dy}{dx} = \frac{d\eta}{dx} = M(x) \quad \text{for} \quad x < 0, \tag{3.48}$$

where $M(x)$ is described by the shape of the curved plate. Equation (3.46) can be integrated to obtain the location of the free surface, which we can presented from the two equation

$$x_{I+1} = x_I + \Delta e^{-\tau_{I+\frac{1}{2}}}\cos\theta_{I+\frac{1}{2}}, \quad \text{for} \quad I = 1...N_1 + N_2, \tag{3.49}$$

and

$$y_{I+1} = y_I + \Delta e^{-\tau_{I+\frac{1}{2}}}\sin\theta_{I+\frac{1}{2}}, \quad \text{for} \quad I = 1...N_1 + N_2. \tag{3.50}$$

3.2.5 Results

The nonlinear problem of the free surface flow past a semi-infinite curved plate in a fluid of finite depth has been solved numerically by using the Conformal mapping and boundary integral method, for the case of the subcritical flows, $F < 1$. A system of nonlinear equation is derived and solved by Newton's method.

We now investigate the numerical solution for the case in which the shape of the stern, as described in the third case in Chapter 2, is defined by

$$M(x) = \begin{cases} 0 & \text{if} \quad x < -L \\ a[e^{bx} - e^{-bL}] & \text{if} \quad -L < x < 0 \end{cases},$$

where a, b and L are real and positive.

For this stern shape, the solution is characterized by a sinusoidal wave downstream. The free surface profiles for this family of plate shapes are shown in figures 3.6(a) and 3.7(a), for $F = 0.5$ and $F = 0.9$, for different values of the parameter $a = 0, \ldots, 0.2$ where $P = 0.01$, $b = 1$. Figures 3.6(b) and 3.7(b) show the relation between the amplitude A and the parameter a. We note that, by increasing the slope of the plate, the wave amplitude decreases up to the local minimum at $a = 0.047$ for $F = 0.5$ and $a = 0.042$ for $F = 0.9$. The local minima, $a = 0.047$ and $a = 0.042$ minimise the wave amplitude, and thus are optimal.

Furthermore, the free surface profile and the relation between the amplitude A and the parameter a are shown in figures 3.8-3.11 for different Froude number, $F = 0.4, \ldots, 0.8$. In addition, the relation between the Froude number F and the amplitude A is shown in figure 3.13. We note that the amplitude increases with increasing the Froude number, for $a = 0.045$, $b = 1$ and $P = 0.01$.

For this family of plate shapes the wave amplitude can be minimised, for any given Froude number, F.

The numerical solutions were computed for $N_1 = 1100$ grid points were used on the free surface, with the Newton's method applied until the residual error is less than 10^{-9} within four iteration as shown in figure 3.5. The errors occur due to numerical implementation, via Trapezoidal rule, of the integral in equations (3.42) and (3.40) as well as the truncation of equation (3.42). The use of Trapezoidal rule and the application of equation (3.42) at points halfway between mesh points allow us to treat the Cauchy Principle Value integral in equation (3.42) as an ordinary integral. The effect of truncation is not expected to be large, since the contribution from each half-period of wave train in the far-field is expected to cancel the next half period; this is particularly the case of small-amplitude waves, which are sinusoidal in shape. Given the complexity of the system, it is difficult to quantify the precise size of the numerical errors for a given mesh, also our quadrature rule offers $O(\Delta\phi^2)$ accuracy, where $\Delta\phi$ is the separation between each numerical grid point. We note, however, that we have applied the usual test of doubling the number of gride points until the resulting free surface profiles are independent of this number within graphical accuracy.

The initial condition chosen to be zero for the case of the flat plate, where $a = 0$. By changing the coefficient a slightly, for example, from $a = 0$ to $a = 0.2$ with $\Delta = 0.01$, the plate changed to a curve, Then the previous results from the flat plate gave such an accurate initial estimate within two iteration to achieve an accuracy of 10^{-9}. The sensitivity of the starting iteration is due to the initial condition that we choose as shown in figure 3.5.

The procedure for the steady free surface profile is summarised in the following algorithm:

```
Algorithm 1: Steady Free surface flow
INPUT: Mesh points on the plate $\phi_j$, mesh point on the free surface $\phi^*_j$, number of mesh points
    on the plate $N_1$, number of mesh point on the free surface $N_2$, the shape of the plate
    $M(x)$, Froude number $F$, pressure $P$.
Step 1: Choose the number of data points on the plate and the free surface $N = N_1 + N_2$.
Step 2: Calculate the midpoints $\phi_{j+\frac{1}{2}}$, $\phi^*_{j+\frac{1}{2}}$ on the plate and free surface given by equation
    (3.32) and (3.33) respectively.
Step 3: Solve the system of nonlinear equation, $Y_I$, given by equations (3.43) and (3.44), using
    Newton's method with initial condition $\theta = (0, 0, 0, ..., 0)^T$ and tolerance $10^{-9}$.
Step 4: Compute the location of the free surface, $x_{I+1}$, $y_{I+1}$, given by equations (3.49) and
    (3.50) at the midpoint using the result in step 3.
```

We investigate the free surface profile for different plate shapes and various values of the parameter F and P using **Algorithm 1**. We noticed that the initial condition has impact on the first iteration. For the case of the flat plate the initial condition chosen to be zero on the plate and the free surface, which gives a good solution and this also had been confirmed by [85]. Moreover, we used the solution for the flat plate case as an initial condition for the curved plate case and this provided better solution and convergence within three iteration.

Finally, in this chapter the numerical solution to the nonlinear problem is investigated, and we note that the wave amplitude can be minimised for this family of stern shapes. In the next chapter, the comparison between the nonlinear, linear and weakly nonlinear solutions for different families of plate shapes will be investigated.

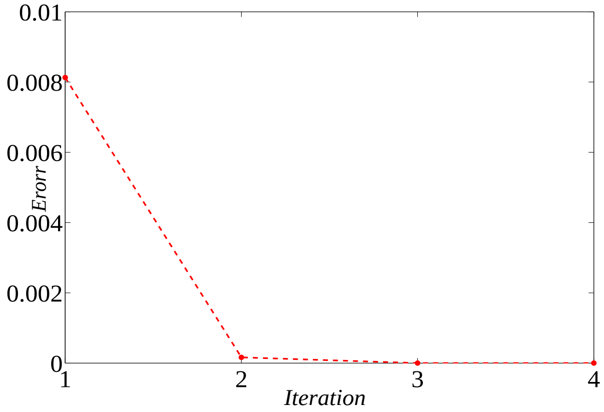

FIGURE 3.5: This figure show the relation between the iteration and the error.

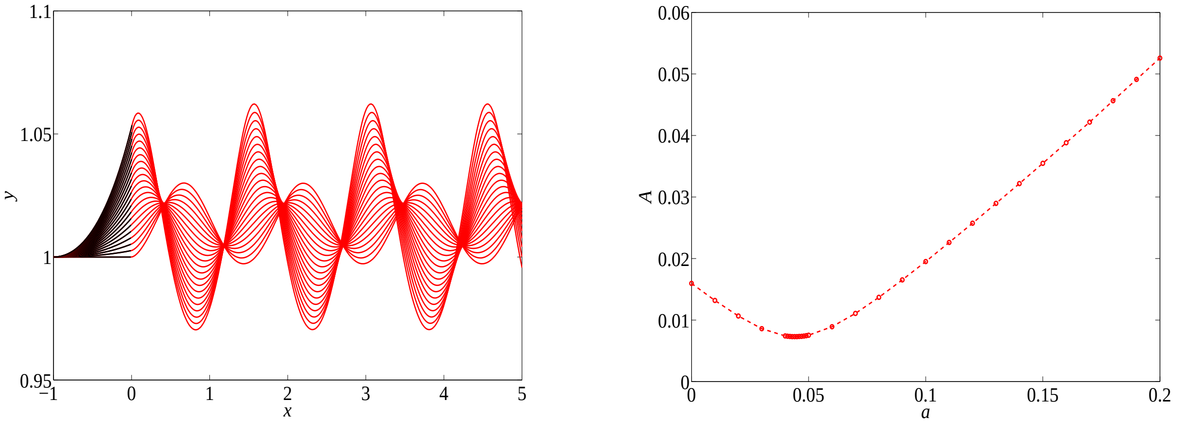

(a) (b)

FIGURE 3.6: The free surface profile for $F = 0.5$, $P = 0.01$, $b = 1$, using $N = 1100$, for $a = 0, \ldots, 0.2$, is shown in figure (a). The dependence of the wave amplitude A and the parameter a is shown in figure (b).

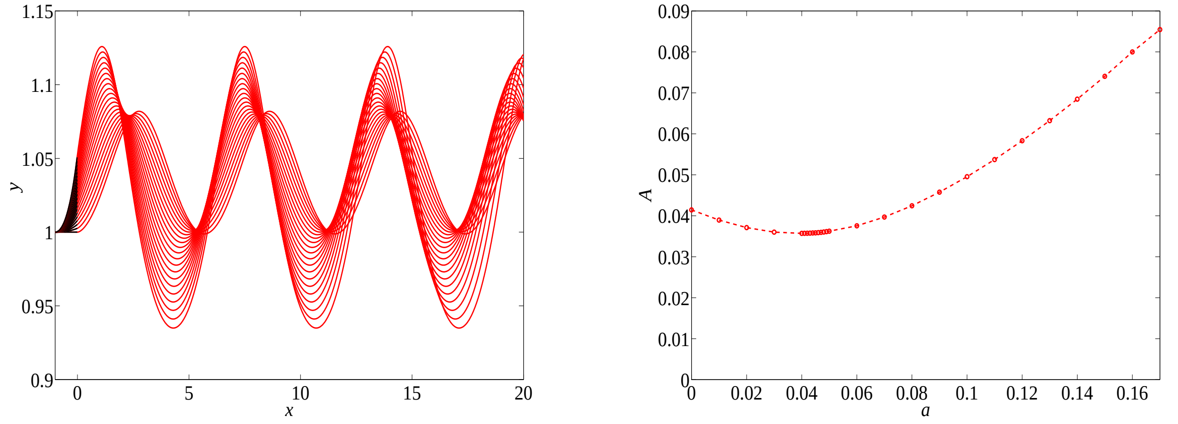

(a) (b)

FIGURE 3.7: The free surface profile for $F = 0.9$, $P = 0.01$, $b = 1$, using $N = 1100$, for $a = 0, \ldots, 0.2$, is shown in figure (a). The dependence of the wave amplitude A and the parameter a is shown in figure (b).

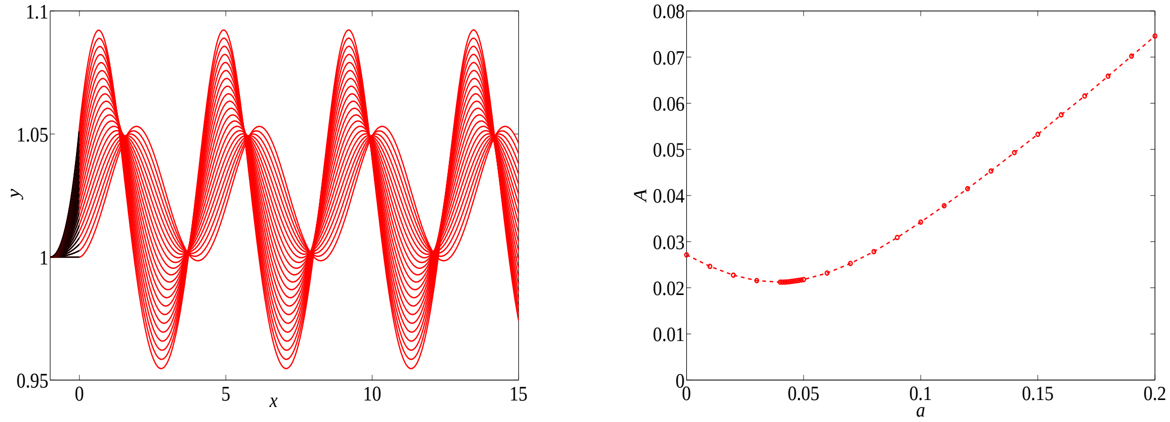

(a) (b)

FIGURE 3.8: Figure (a) shows the numerical solution for $F = 0.8$, $P = 0.01$, $b = 1$, $a = 0, \ldots, 0.2$. The relation between the amplitude A and the parameter a at the Froude number $F = 0.8$ is shown in figure (b).

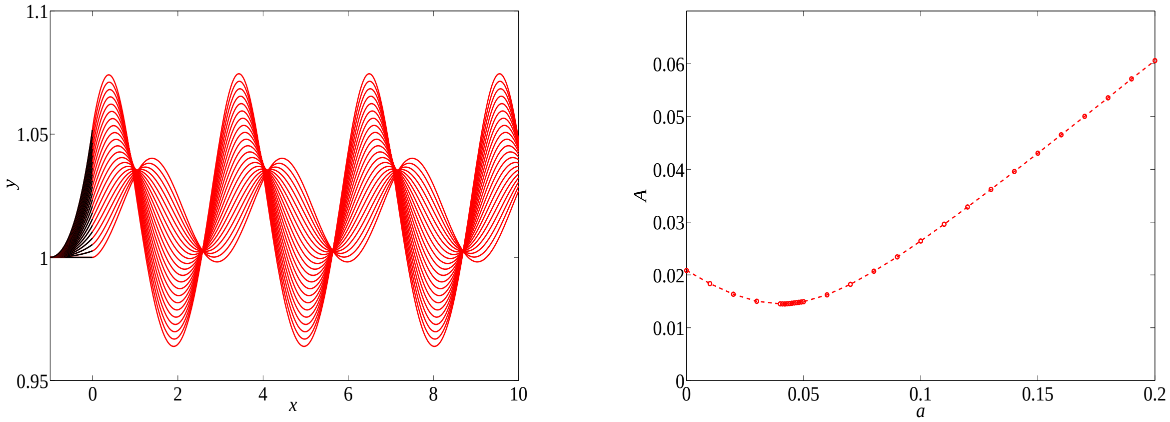

(a) (b)

FIGURE 3.9: Figure (a) shows the numerical solution for $F = 0.7$, $P = 0.01$, $b = 1$, $a = 0, \ldots, 0.2$. The relation between the amplitude A and the parameter a at the Froude number $F = 0.7$ is shown in figure (b).

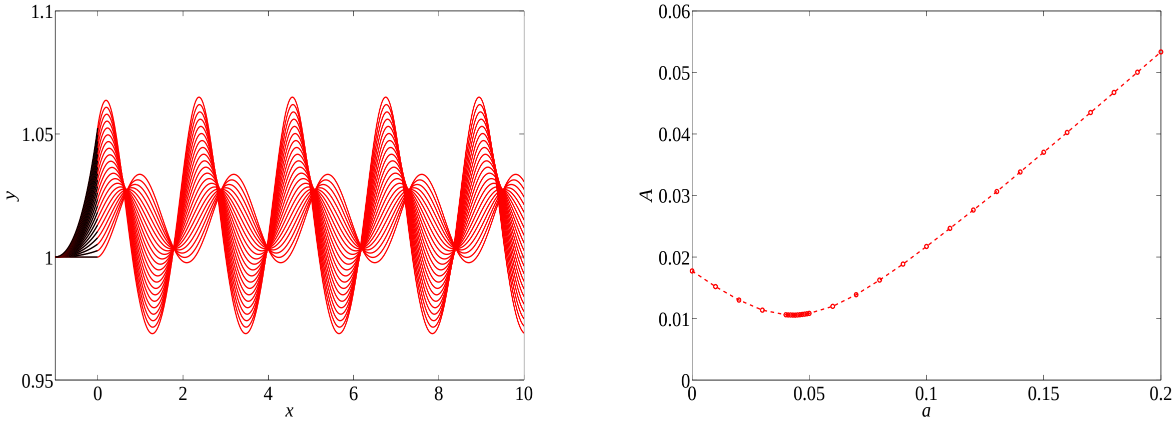

(a) (b)

FIGURE 3.10: Figure (a) shows the numerical solution for $F = 0.6$, $P = 0.01$, $b = 1$, $a = 0, \dots, 0.2$. The relation between the amplitude A and the parameter a at the Froude number $F = 0.6$ is shown in figure (b).

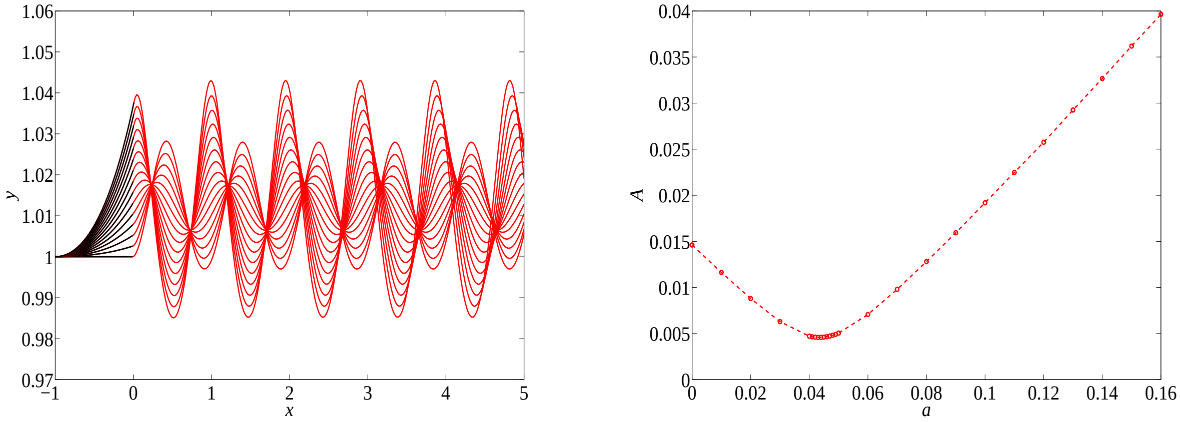

(a) (b)

FIGURE 3.11: Figure (a) shows the numerical solution for $F = 0.4$, $P = 0.01$, $b = 1$, $a = 0, \dots, 0.14$. The relation between the amplitude A and the parameter a at the Froude number $F = 0.4$ is shown in figure (b).

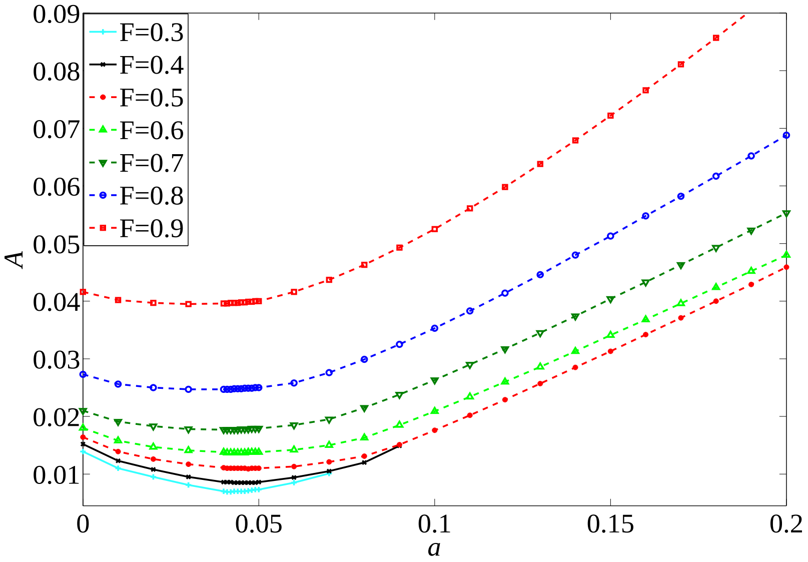

FIGURE 3.12: This figure shows the relation between the amplitude A and the parameter a for various Froude numbers $F = 0.3, \ldots, 0.9$, for $P = 0.01$ and $b = 1$.

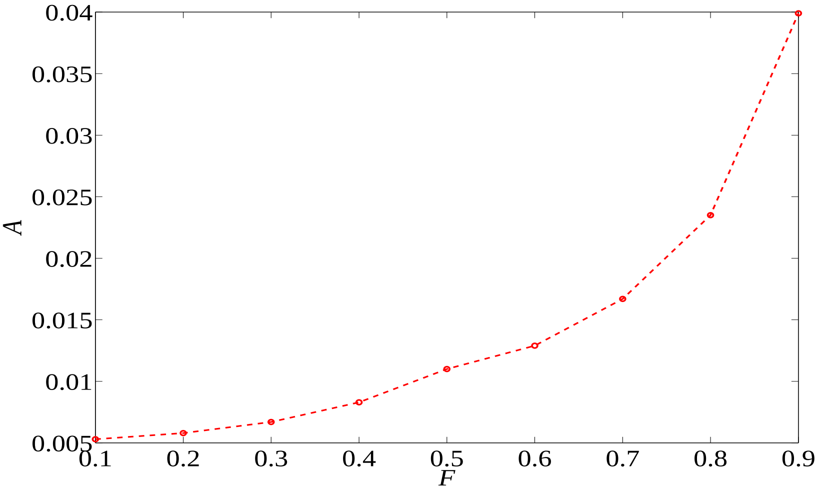

FIGURE 3.13: This figure shows the relation between the amplitude A and the Froude number F, for $a = 0.045$, $P = 0.01$ and $b = 1$.

Chapter 4

Weakly Non-linear Theory

4.1 Introduction

The problem of free surface flow past a semi-infinite curved plate in a fluid of finite depth has been solved analytically by using the the Wiener–Hopf technique in Chapter 2 and numerically by using the boundary integral technique for the case of the subcritical solution $F < 1$, in Chapters 3. In this chapter, the weakly nonlinear solution will be presented describing the flow of the free surface using the Korteweg–de Vries equation (KdV). This problem depends on two parameters, namely the Froude number, F, and the applied pressure P, as defined in (5.16).
We will present a comparison between the analytical, numerical and weakly non-linear solutions for different stern shapes, and examine the effect of the stern shape to minimise or even eliminate the wave amplitude, and hence minimise the wave drag. The results will also be compared with those in the literature.
We consider two kinds of plate shapes, namely, flat and curved plates. For the curved stern, we will consider three variation of stern shapes; the one treated by Binder [11], the third case in Chapter 2, Section 2.4, and a new stern shape, to be introduced in Section 4.5.2.

4.2 Weakly Nonlinear Theory

The Korteweg–de Vries equation (KdV) has been derived to model the flow past an obstacle. This theory is valid in the weakly–nonlinear, long–wave limit and has been investigated and applied successfully by many authors including Shen [88], Binder and Vanden-Broeck [6], Binder *et al.* [8] and Binder [11]. For the regime $F \sim 1$ and $P \ll 1$, the steady free surface is governed by the Korteweg–de Vries equation (KdV)

$$\frac{d^3\eta}{dx^3} + 3[2(1-F) + 3\eta]\frac{d\eta}{dx} = 0. \tag{4.1}$$

Integrating once gives

$$\frac{d^2\eta}{dx^2} + \frac{9}{2}\eta^2 + 6(1-F)\eta = 3P. \tag{4.2}$$

Multiplying by $d\eta/dx$ and integrating again, we obtain

$$\left(\frac{d\eta}{dx}\right)^2 + 6(1-F)\eta^2 + 3\eta^3 - 6P\eta = C, \tag{4.3}$$

where C is a constant of integration that is found by evaluating equation (4.3) at $x = 0$. The solution of equation (4.3) can be constructed in the phase plane, as described in Binder [11]. However, we note that equation (4.3) has an exact solution, as will be shown below.

The solution to (4.3) will be a wavetrain with amplitude A and wavelength λ. Let the value of η at the trough be given by η_T, and the value of η at the crest be given by $\eta_C = \eta_T + 2A$. These two points on the wavetrain are characterised by zero slope, and from (4.3) we see that η_T and η_C are both positive roots of the equation

$$6(1-F)\eta^2 + 3\eta^3 - 6P\eta = C. \tag{4.4}$$

The other real root η_N of this equation is negative. Denoting the three roots of (4.4) as η_N, η_T and η_C, we have

$$\frac{1}{3}\left(\frac{d\eta}{dx}\right)^2 = (\eta - \eta_T)(\eta_C - \eta)(\eta - \eta_N).$$

Performing the change of variable

$$\eta_C - \eta = (\eta_C - \eta_T)q^2, \tag{4.5}$$

we obtain

$$\frac{4}{3}\left(\frac{dq}{dx}\right)^2 = (1-q^2)(\eta_C - \eta_N - (\eta_C - \eta_T)q^2).$$

This equation is separable, and can be written as

$$\frac{dq}{\sqrt{(1-q^2)(1-(\eta_C-\eta_T)q^2/(\eta_C-\eta_N))}} = \frac{\sqrt{3(\eta_C-\eta_T)}}{2}dx.$$

Integrating this equation, we find that

$$q = \mathrm{sn}\left(\frac{\sqrt{3(\eta_C-\eta_N)}}{2}x + K, \frac{\eta_C-\eta_T}{\eta_C-\eta_N}\right), \tag{4.6}$$

where $\mathrm{sn}(z, m)$ is a Jacobian elliptic function [67], and the constant, K, which fixes the initial condition is given by

$$K = \int_0^{\sqrt{\frac{\eta_C-\eta(0)}{\eta_C-\eta_T}}} \frac{dq}{\sqrt{(1-q^2)(1-(\eta_C-\eta_T)q^2/(\eta_C-\eta_N))}}.$$

Substituting equation (4.5) into equation (4.6), we obtain

$$\eta = \eta_T + (\eta_C - \eta_T)\mathrm{cn}^2\left(\frac{\sqrt{3(\eta_C-\eta_N)}}{2}x + K, \frac{\eta_C-\eta_T}{\eta_C-\eta_N}\right),$$

where cn is another Jacobian elliptic function [67], with the property $\mathrm{cn}(z,\ell) \sim \cos z$ as $\ell \to 0^+$. The amplitude of the wavetrain is simply found by solving the cubic equation (4.4) numerically to give

$$A = \frac{1}{2}(\eta_C - \eta_T). \tag{4.7}$$

We note that this solution for the free surface depends on the values of η and $d\eta/dx$ at the single point $x = 0$, as well as the values of the parameter F and P, and does not explicitly depend on the full shape of the plate for $x \leq 0$; that is, the weakly nonlinear theory is only affected by the slope and location of the plate at the point at which the free surface detaches.

Let $M(x) = d\eta/dx$ denote the slope of the curved plate. We consider two cases, namely flow past a flat plate and flow past a curved plate.

For the first case, $M(x) = 0$, the constant of integration, C, is obtained by substituting $d\eta/dx = 0$ in (4.3) to give

$$\eta = \frac{2}{3}(F-1) + \sqrt{\frac{4}{9}(F-1)^2 + \frac{2}{3}P},$$

at the center point.

For the curved plate, we consider three families of plate shapes, the first of which is defined by

$$M(x) = \begin{cases} 0 & \text{if} \quad -\infty < x < -L \\ \frac{Pa[e^{bx} - e^{-bL}]}{1-F^2} & \text{if} \quad -L < x < 0 \end{cases},$$

where a, b and L are real and positive, with $\eta(x)$ given by

$$\eta(x) = \frac{Pa}{1-F^2}\left[\frac{e^{bx}}{b} - xe^{-bL}\right] + C, \tag{4.8}$$

where C is a constant, obtained by substituting $\eta = 0$ at $x = -L$ at the center point in (4.8) to give

$$C = -\frac{Pa}{1-F^2}\left[\frac{e^{-bL}}{b} + Le^{-bL}\right].$$

Substituting this into equation (4.8), we have

$$\eta(x) = \frac{Pa}{1-F^2}\left[\frac{e^{bx}}{b} - xe^{-bL} - \frac{e^{-bL}}{b} - Le^{-bL}\right]. \tag{4.9}$$

The second stern shape, considered by Binder [11], is given by

$$M(x) = \begin{cases} 0 & \text{if} \quad -\infty < x < -\pi \\ -\frac{\alpha}{2}\sin(x) & \text{if} \quad -\pi < x < 0 \end{cases},$$

for which $\eta(x)$ is given by

$$\eta(x) = \frac{1}{2}\alpha(1 + \cos(x)). \tag{4.10}$$

Generalising the stern shapes considered by Binder to

$$M(x) = \begin{cases} 0 & \text{if} \quad -\infty < x < -\pi \\ -\frac{1}{2}\alpha\sin(x) + \beta\left[\cos(x) + \cos(2x)\right] & \text{if} \quad -\pi < x < 0 \end{cases},$$

noting that for $\beta > 0$ the stern has a distinctive downward angle at the detachment point, we find that $\eta(x)$ is given as

$$\eta(x) = \frac{1}{2}\alpha(1 + \cos(x)) + \beta\left[\sin(x) + 2\sin(2x)\right]. \tag{4.11}$$

4.3 Results for the Flat Plate Case

We begin the comparison between linear, nonlinear and weakly nonlinear solutions by considering a special case of the flat plate when the value of the parameter $a = 0$ or $\alpha = 0$. The solutions are characterised by a train of sinusoidal waves downstream as noted for the linear problem in Chapter 2.

In figures 4.1 and 4.2 the comparison between the analytic, numerical and weakly nonlinear solutions is exhibited for Froude numbers $F = 0.5$, and $F = 0.9$, respectively. In figure 4.1(a), (b), (c) and (d), the free surface profiles are shown when the shape of the stern is flat for $F = 0.9$ and $P = 0.1, 0.01, 0.001$ and 0.0001, respectively. The numerical solution is depicted as the red solid-line, the analytic solution is depicted by the black dashed-line and the weakly nonlinear solution is depicted by the blue dot dashed-line. For these values of the parameters, the comparison between the analytic and the weakly nonlinear solution for a high value of P, is not good, as shown in figure 4.1(a), at $P = 0.1$. However, for much smaller values of P, the solution for the free surface profile is good as shown in figure 4.1(d), at $P = 0.0001$. The numerical solution can be seen to be in excellent agreement, for the small value of $P = 0.0001$, with the analytic solution and in good agreement with the weakly nonlinear solution, as shown in figure 4.1(d). The numerical solution in these figures was computed with $N_1 = 1000$ grid points on the free surface.

Figure 4.2(a), (b), (c) and (d) show the free surface profile for the three solution methods, for $F = 0.5$ and $P = 0.1, 0.01, 0.001$ and 0.0001, respectively. We note that the analytic solution and the weakly nonlinear solution do not agree for $F = 0.5$, although the weakly nonlinear solution gives a good approximation for $F = 0.9$ and $P = 0.01$ as shown in Binder ([11], 2010). Also the numerical solution for $P = 0.1$, $F = 0.5$ doesn't converge, as shown in figure 4.2(a). However, decreasing the values to $P = 0.01, 0.001$, and 0.0001, the analytic and the numerical solution are in excellent agreement as shown in figure 4.2(b), and (d).
We conclude that an agreement for the three solutions for Froude number $F \sim 1$ at a small value of P. And an excellent agreement between the analytic solution and numerical solution for $F = 0.5$ and small values of P.

In addition, the validity of the numerical solution is shown for different Froude numbers at the highest value of P in figure 4.3. The highest value of P that the numerical solution allows is at $P = 0.05$ and $P = 0.3$ for $F = 0.5$ and $F = 0.9$, respectively. In these figures, as the plate is moved further from the undisturbed level, $y = 1$, the amplitude increases while the wavelength decreases, and the waves develop sharp crests and broad troughs. Beyond this, the numerical solution does not converge.

The relation between the amplitude, A, and the Froude Number, F, for a fixed value of P is shown in figure 4.4 for $P = 0.01$, where it can be seen that increasing the Froude number, increases the amplitude.

The free surface profiles in figure 4.5 show the comparison between the analytic solution and the numerical solution at the same scale as that presented by McCue and Forbes [82], for $F = (1-\epsilon)\tilde{F}$, where $\tilde{F} = 0.5$, $\epsilon = 0.001$ and 0.058, respectively. These figures confirm the accuracy of the numerical solution for the case of the flat plate.

Figure 4.6, shows the nonlinear profile and the phase trajectories presented by Binder [11] for the case of a flat plate, for $F = \hat{F} = 0.9$ and $P = 0.01$. Figure 4.7 shows the weakly nonlinear profile and the phase trajectories for the flat plate case. For $F = 0.9$ and $P = 0.01$, this figures is presented by Binder ([11], 2010). The phase planes in figure 4.6(b) and 4.7(b) can be described as follows; we start at the origin in the phase plane, which represents the flat plate, and then move along the circle to describe the waves on the free surface.

We conclude the analytical, numerical and weakly nonlinear solutions are in excellent agreement for the free surface flow past a flat plate for $F \sim 1$, with a small value of $P = 0.001$, producing waves with amplitude $A \sim 0.00105$.

In the next section, we will consider the case when the stern of the ship is curved, as treated by Binder [11]. Binder presented the numerical and weakly nonlinear solution. Here we will compare our linear solution with the other two solutions.

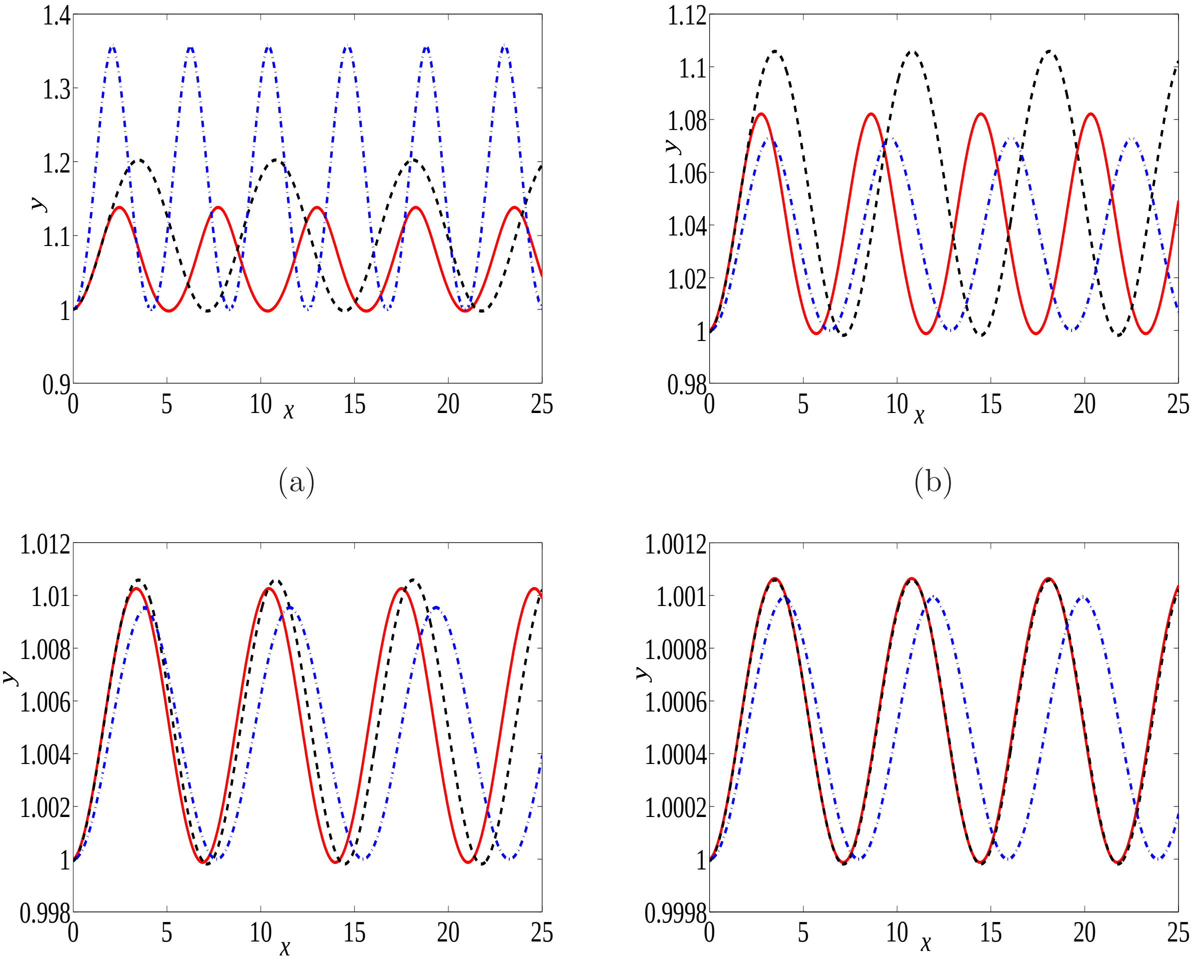

(a) (b)

(c) (d)

FIGURE 4.1: Figures of the free surface, comparing the numerical (solid-lines), analytical (dashed-lines), and weakly nonlinear (dot dashed-lines) solutions for the case of the flat plate, with Froude number $F = 0.9$, and $\epsilon = P/(1 - F^2)$ at (a) $P = 0.1$, at (b) $P = 0.01$, (c) $P = 0.001$, and (d) $P = 0.0001$.

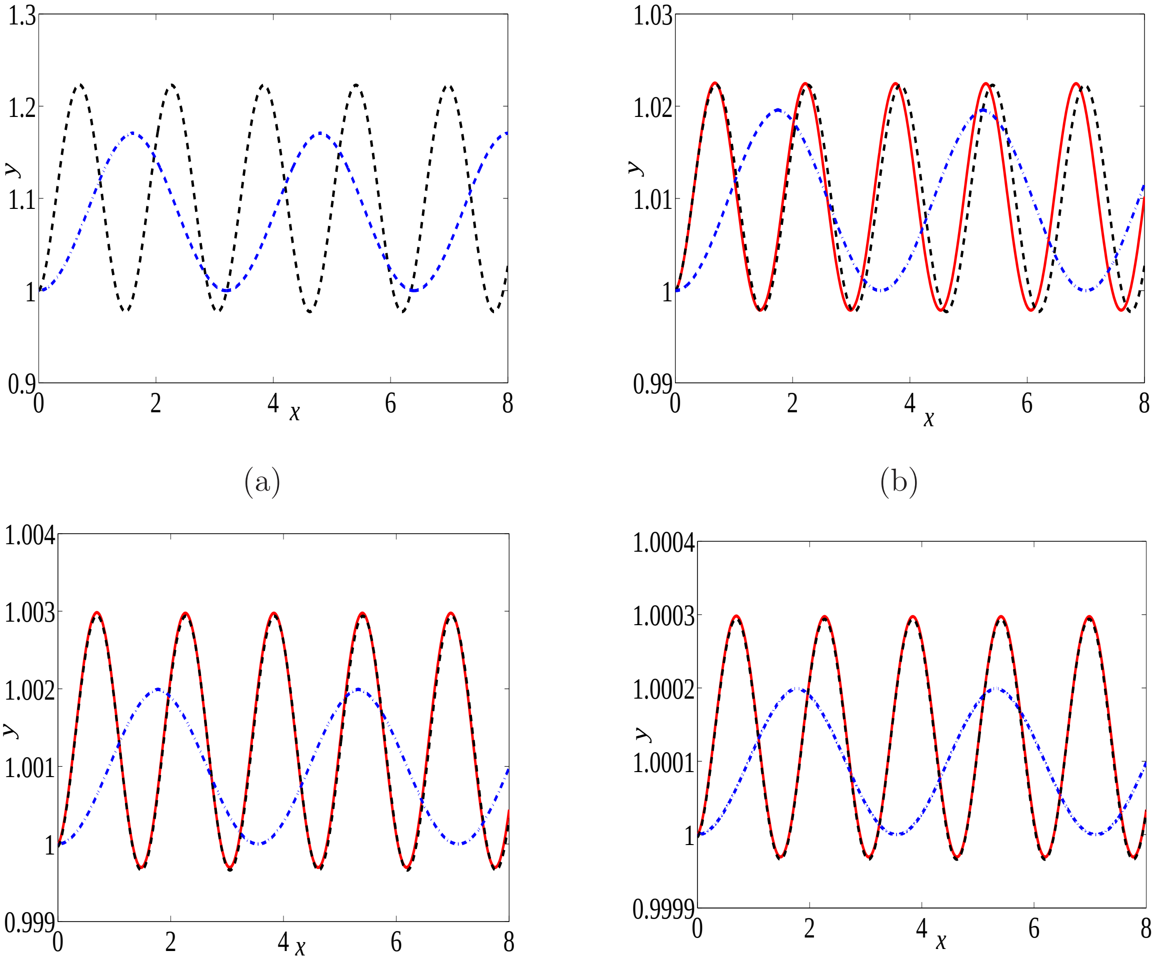

(a) (b)

(c) (d)

FIGURE 4.2: Figures of the free surface, comparing the numerical (solid-lines), analytical (dashed-lines), and weakly nonlinear (dot dashed-lines) solutions for the case of the flat plate, with Froude number $F = 0.5$, and $\epsilon = P/(1 - F^2)$ at (a) $P = 0.1$, at (b) $P = 0.01$, (c) $P = 0.001$, and (d) $P = 0.0001$. Note that, in (a), the numerical solution does not converge, and thus is not shown.

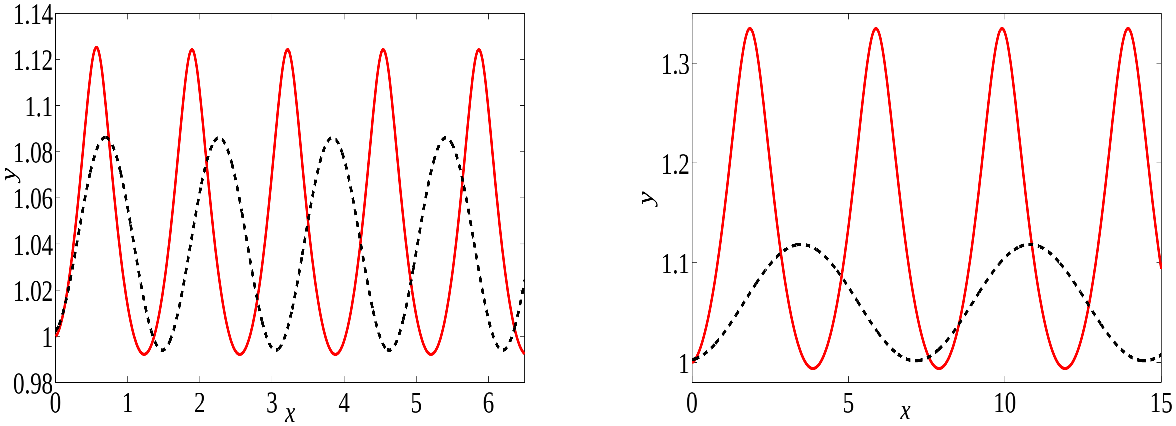

(a) (b)

FIGURE 4.3: Figures (a) and (b) show the comparison between the numerical solution (solid-line), analytical solution (dashed-line), for the highest value of P that the numerical solution allows. The Froude number $F = 0.5$ (figure (a)) and $= F = 0.9$ (figure (b)), at $P = 0.05, 0.3$ respectively.

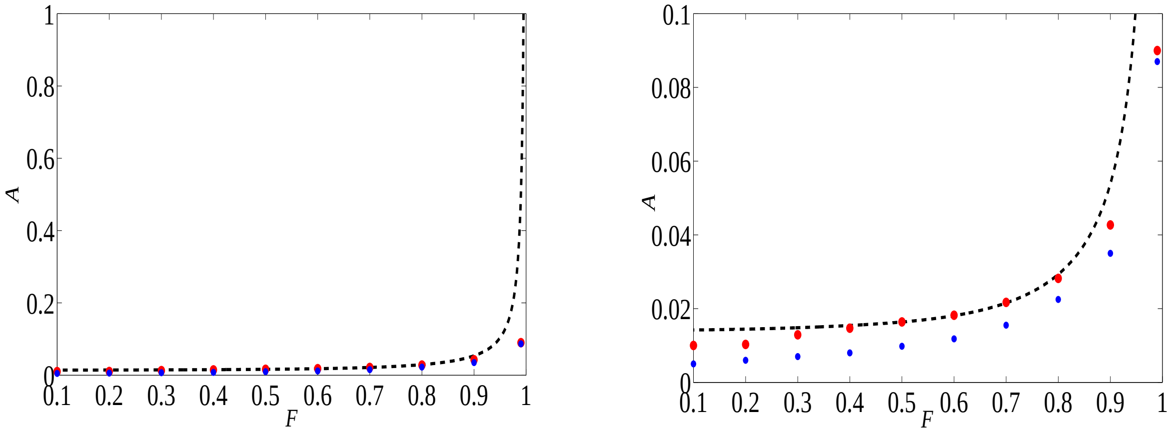

(a) (b)

FIGURE 4.4: Figures (a) and (b) show the relation between the amplitude A and the Froude number F for the case of the flat plate at $P = 0.01$, for the analytical (dashed-line), numerical (red dots), and weakly nonlinear solutions (blue dot), for different scale.

4.4 Geometry Treated By Binder (2010)

In 2010, Binder ([11]) investigated the numerical and the weakly nonlinear solutions of the free surface flow past a curved plate. The slope of the stern was given by

$$M(x) = \begin{cases} 0 & \text{if} \quad -\infty < x < -\pi \\ -\frac{\alpha}{2}\sin(x) & \text{if} \quad -\pi < x < 0. \end{cases}$$

Binder presented the free surface profiles for the numerical and the weakly nonlinear solutions for $F = 0.9$ and $P = 0.01$, for different values of α. In this section, we revisit the stern shapes considered by Binder. For each value of the parameter, α, the shape of the stern is characterised having a zero slope at the point at which the free surface detaches. Using the weakly nonlinear theory of Section 4.2, Binder showed that by carefully choosing the value of α, a trajectory representing the plate in phase space will terminate at the 'center', so that the two positive roots of (4.4) coalesce, and the amplitude of the waves given by equation (4.7) vanish completely. As a comparison, Binder also included a numerical solution to the fully

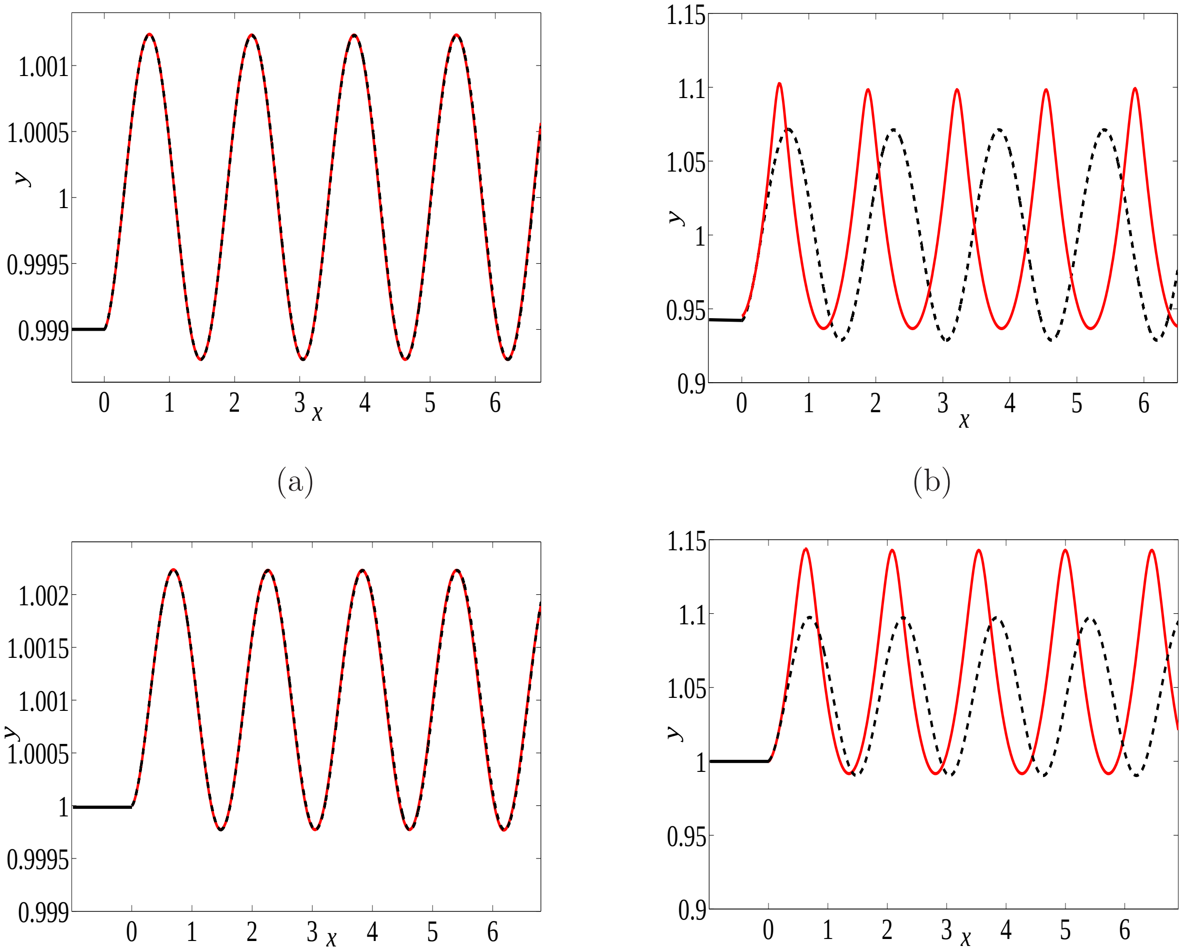

(a) (b)

(c) (d)

Figure 4.5: Figures (a) and (b) show the comparison between the numerical solution (dashed-line), analytical solutions in the solid-line for the case of the flat plate. The Froude number $\tilde{F} = 0.5$ and $\epsilon = 0.001, 0.058$ respectively, where $F = (1-\epsilon)\tilde{F}$. These figures are as presented by McCue and Forbes in 2002. In figure (c) and (d) shows the comparison between analytical and numerical solutions for $F = 0.5$ and $P = 0.001$, 0.058 respectively.

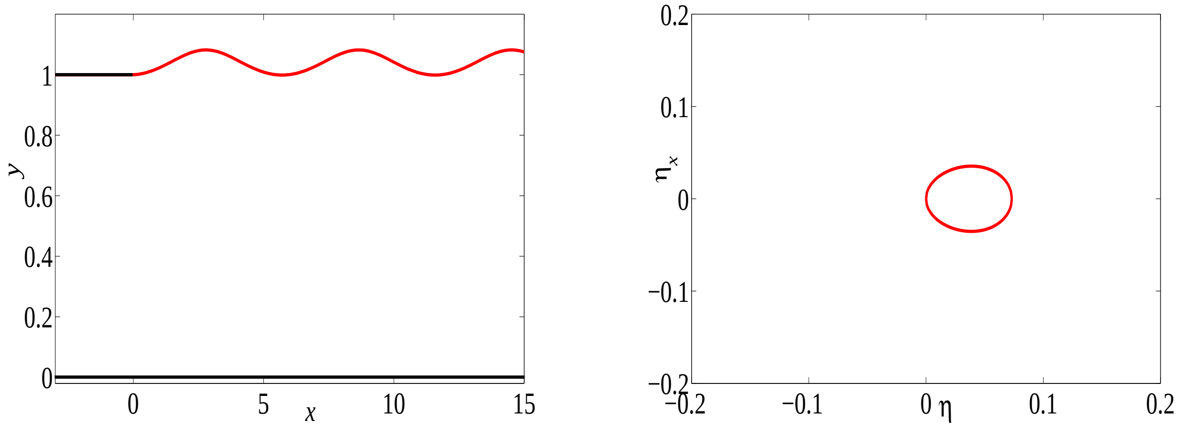

(a) (b)

FIGURE 4.6: The nonlinear profile for the case of the flat plate is shown in figure (a) and the phase trajectories in figure (b), at the Froude number $F = 0.9$ and $P = 0.01$.

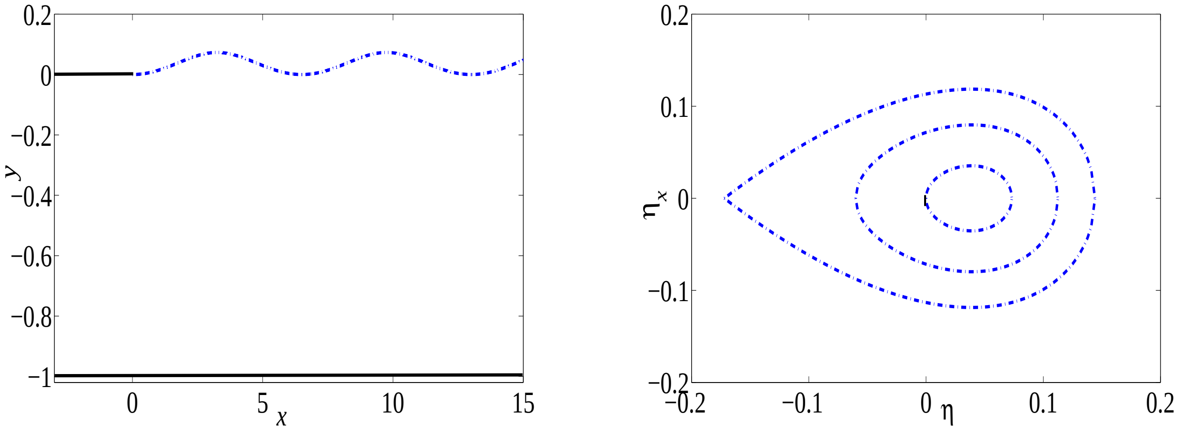

(a) (b)

FIGURE 4.7: The weakly nonlinear profile for the case of the flat plate are shown in figure (a) and the phase trajectories in figure (b), at the Froude number $F = 0.9$ and $P = 0.01$.

nonlinear problem and we include here the analytic solution to the linear problem for different values of Froude number F and α.

In figure 4.8, the relation between the amplitude A and the parameter α for the fully nonlinear, linear and weakly nonlinear solutions at $F = 0.9$ and $P = 0.01$ are investigated. In the weakly nonlinear solution the amplitude goes to zero at $\alpha = 0.0378$, which is the value predicted by Binder [11]. However, the curve corresponding to the numerical solution of the fully nonlinear problem appears to have a nonzero local minimum, at $\alpha = 0.0427$, although the resulting amplitude is very small, $A = 0.0002$. We note that the linear solution in figure 4.8 does not agree particulary well with the numerical solution, because while $P/(1 - F^2)$ is reasonably small for these solutions (a requirement for the linear theory to be valid), $F = 0.9$ is a large Froude number, and the linear theory breaks down as $F \to 1^-$.

To illustrate the size of the minimum wave amplitude noted above, the fully nonlinear free surface profile for $\alpha = 0.0427$, as well as for $\alpha = 0.019$ and 0.0655 are presented in figure 4.9. In figure 4.9(a), the free surface profile is displayed on a scale that includes the flat bottom of the channel, while figure 4.9(b) shows the result more clearly. We see that the profiles for $\alpha = 0.019$ and 0.0655 have roughly the same amplitude, $A = 0.023$, yet are out of phase, while the profile for $\alpha = 0.0427$ has an amplitude that is so small ($A = 0.0002$) that the waves do not appear visible on the scale of figure 4.9(a).

In figure 4.10, the free surface profile and the phase plane for the weakly nonlinear solution for $F = 0.9$ and $P = 0.01$ with $\alpha = 0.057, 0.019$ and 0.038 are shown. The phase plane is described as follows: we start at the origin in the phase plane, which represents the the horizontal flat bottom of the plate and then move along the black curved part at the separation point between the curved plate and the free surface, until we reach the periodic wave orbit representing the waves for figures 4.10(b) and (d). However in figure 4.10(f), we move along the black curve part at the separation point between the curved plate and the free surface $(x, \eta) = (0, 0.05)$, $(\eta, \eta_x) = (0.05, 0)$ in the phase plane and by moving along the flat free surface, we arrive at the same point $(\eta, \eta_x) = (0.05, 0)$ in the phase plane, which represents no waves.

To explore the issue of eliminating waves further, we show the relationship between wave amplitude and α for Froude number $F = 0.5$, $P = 0.01$ in figure 4.11. We note that the wave amplitude in the linear and nonlinear solution at $\alpha = 0.0134$ and 0.0136 (the local minimum) respectively, is very small, $A = 1.9220 \times 10^{-4}, 2.6417 \times 10^{-4}$, as shown in figure 4.12 and 4.13, respectively. Also, for $F = 0.5$ and $P = 0.04$, the relation between wave amplitude and α is shown in figure 4.14 (a) and (b) at different scales. This parameter set is chosen such that $1 - F$ is not small, but the value of $P/(1 - F^2)$ is roughly the same as in figures 4.8 and 4.9. Again, we note that for the weakly nonlinear theory, the wave amplitude reduces to zero for some α, yet the fully nonlinear solutions have a very small but nonzero minimum amplitude, with the minimum amplitude again of the order of $A = 0.0002$. In figure 4.15 we show the relation between the amplitude A and the Froude number F at $P = 0.01$ and $\alpha = 0.0427$, which exhibit a decrease in amplitude with increasing Froude number.

From this, we may conclude that for the one-parameter family of stern shapes considered by Binder [11], the weakly nonlinear theory predicts that the wave amplitude will vanish for a single member (corresponding to a single value of the parameter α) in the limit $F \to 1^-$ and $P/(1-F^2) \to 0$. However, strictly speaking, for $1 - F$ and $P/(1 - F^2)$ finite, the downstream waves can be minimised, but not entirely eliminated. The weakly nonlinear theory of Binder [11] does, however, provide a relatively simple and elegant way to predict what shape of stern will generate small or large downstream waves.

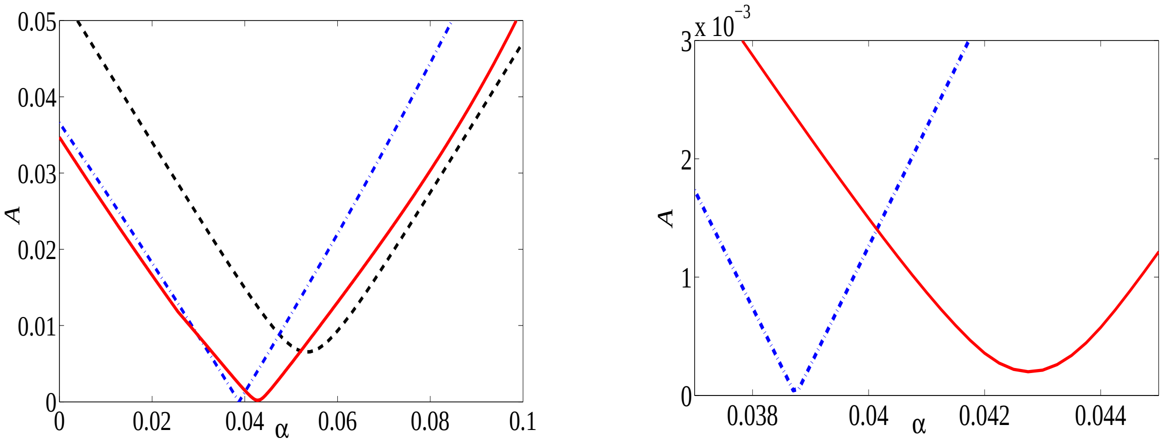

(a) (b)

Figure 4.8: The dependence of the wave amplitude A on the parameter α for $F = 0.9$, $P = 0.01$. The red solid curve, black dashed curve and blue dot-dashed curve correspond to the fully nonlinear, linear and weakly nonlinear solution, respectively. In (a) the scale is such that the nonlinear amplitude appears to vanish at a value of α, but the scale in (b) suggests there is in fact a local minimum for which A is finite but small.

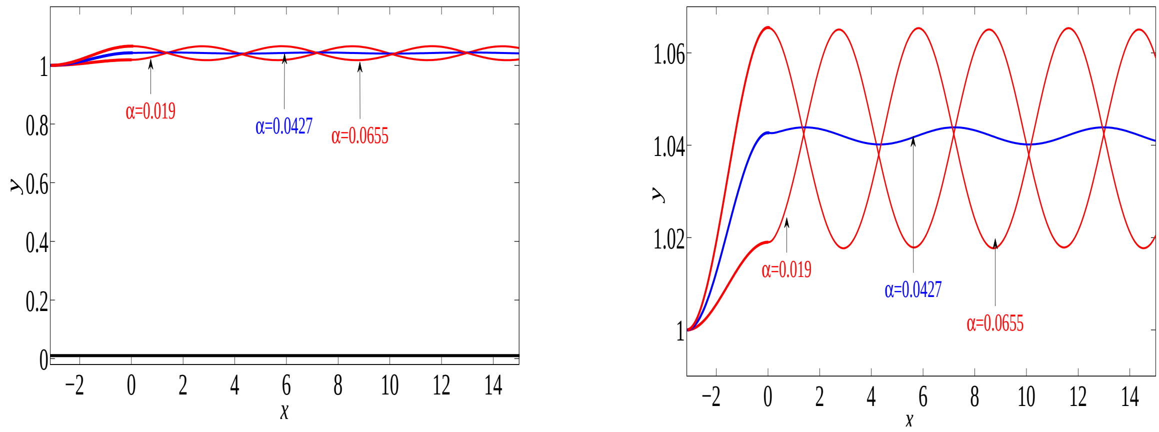

(a) (b)

FIGURE 4.9: The nonlinear free surface profiles drawn for different scales, with $F = 0.9$, $P = 0.01$ at $\alpha = 0.019$(red), 0.0655(red), 0.0427(blue) respectively.

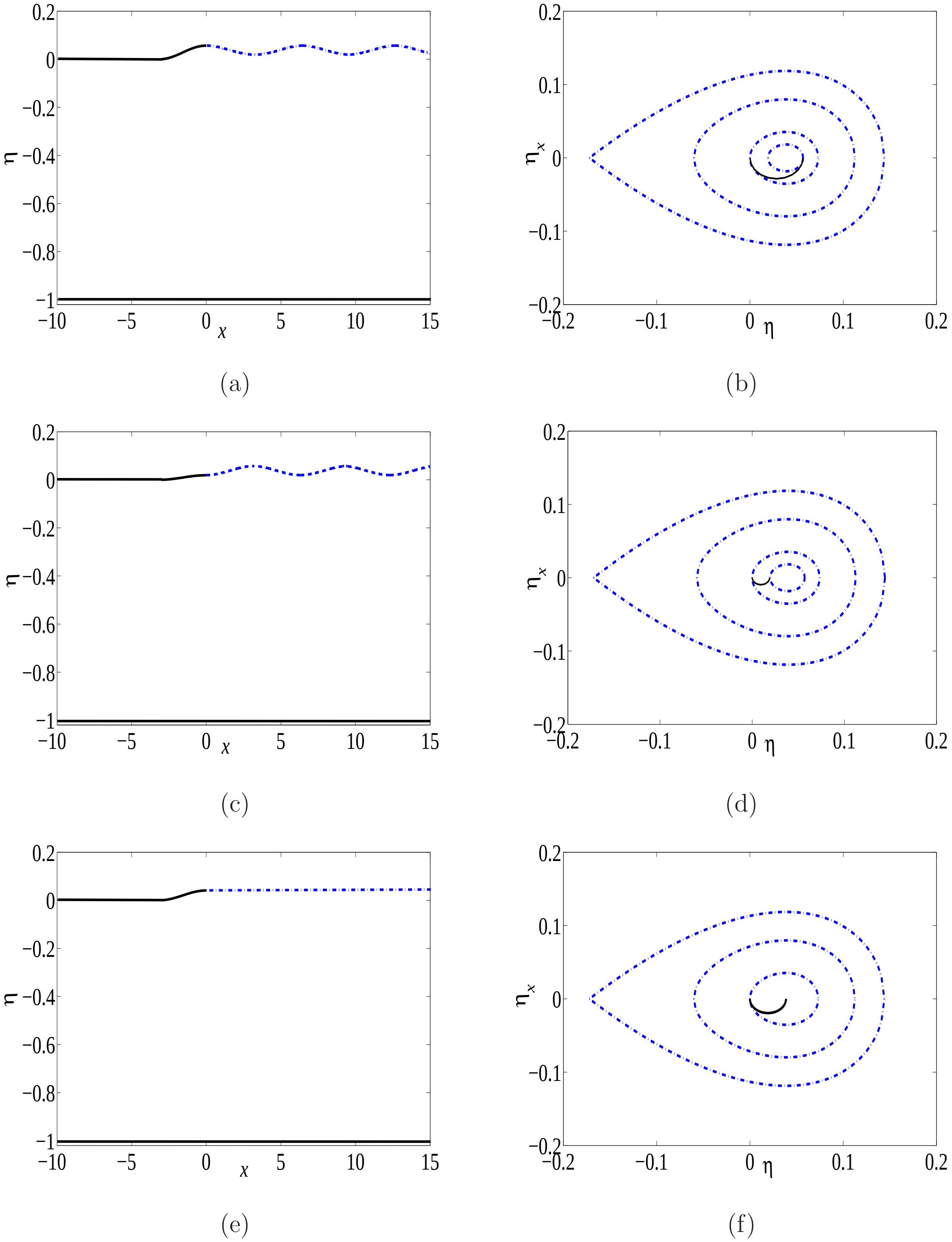

(a) (b)

(c) (d)

(e) (f)

FIGURE 4.10: The weakly nonlinear profiles are shown in figure (a), (c) and (e), and phase trajectories are shown in figure (b), (d) and (f), with the Froude number $F = 0.9$ and $P = 0.01$ at $\alpha = 0.057, 0.019$, and 0.038, respectively. These figures are the same as figures drawn by Binder ([11], 2010).

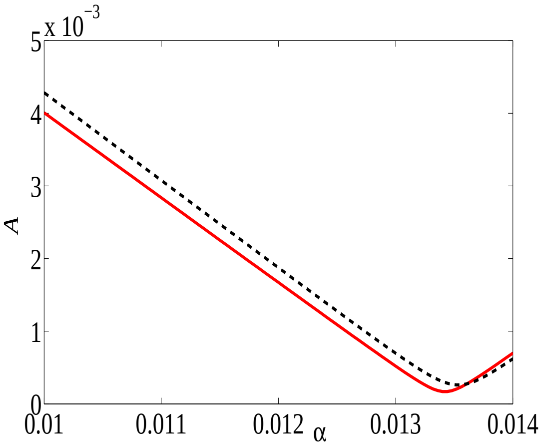

FIGURE 4.11: This figure shows the relation between the amplitude A and the parameter α for Froude number $F = 0.5$ and $P = 0.01$. The red solid curve and black dashed curve correspond to the fully nonlinear and linear solution, respectively.

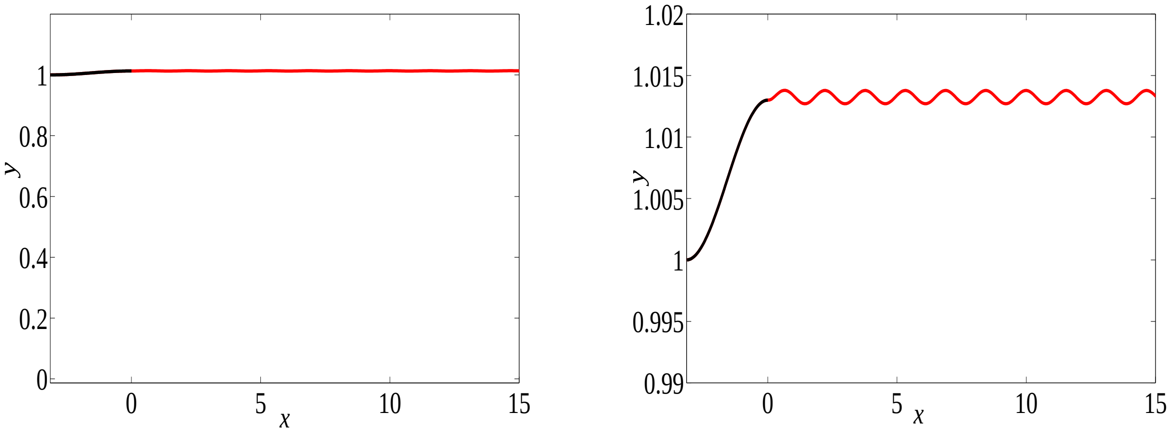

(a) (b)

FIGURE 4.12: Figures (a) and (b) show the free surface profile for the numerical solution at the Froude number $F = 0.5$, $P = 0.01$ and $\alpha = 0.0134$(local minimum), for a different scale with amplitude $A = 1.9220 \times 10^{-4}$.

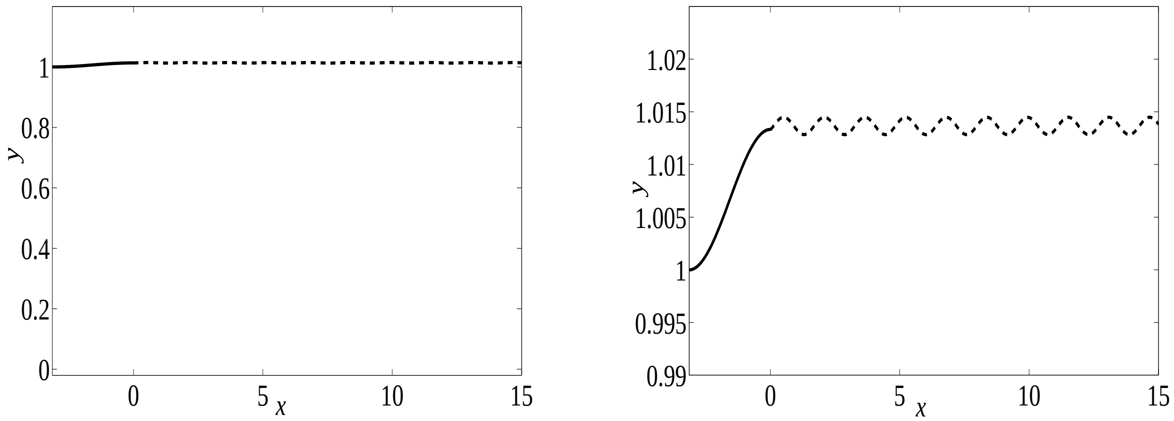

(a) (b)

FIGURE 4.13: Figures (a) and (b) show the free surface profile for the analytical solution at the Froude number $F = 0.5$, $P = 0.01$ and $\alpha = 0.0136$(local minimum), for a different scale with amplitude $A = 2.6417 \times 10^{-4}$

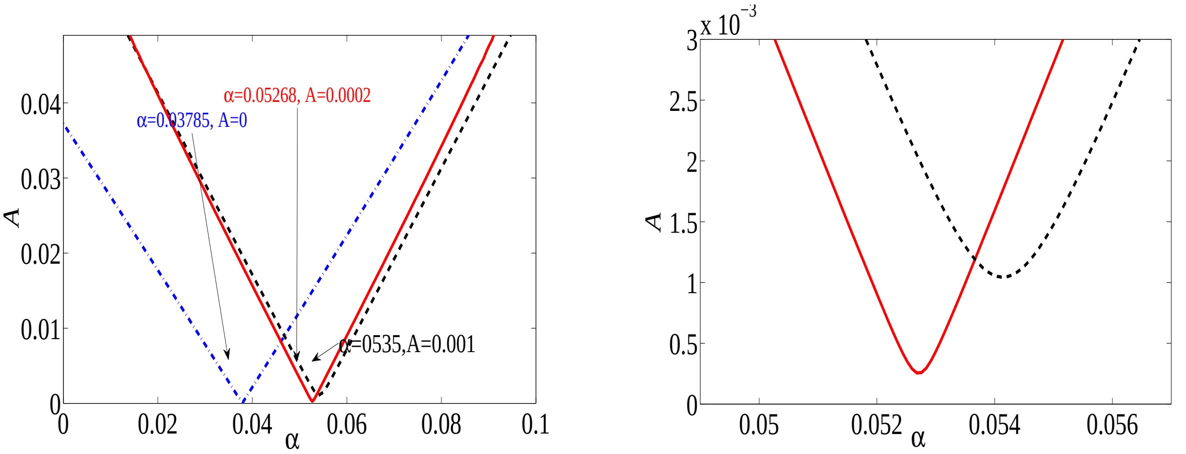

(a) (b)

FIGURE 4.14: The dependence of the wave amplitude A on the parameter α for $F = 0.5$, $P = 0.04$. The red solid curve, black dashed curve and blue dot-dashed curved correspond to the fully nonlinear, linear and weakly nonlinear solutions, respectively.

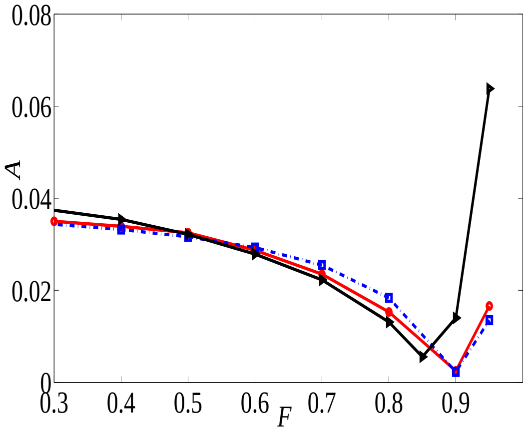

FIGURE 4.15: The relation between the amplitude A and the Froude number F at $\alpha = 0.0427$, $P = 0.01$ are shown in this figure. The red solid curve, black solid curve and blue dot-dashed curved correspond to the fully nonlinear, linear and weakly nonlinear solution, respectively.

4.5 Results for a Family Of Curved Plates

We now examine the effect that two new families of plate shapes have on the minimisation, or elimination, of the downstream waves.

4.5.1 Upward Pointing Sterns

This family of plate shapes is given by

$$M(x) = \begin{cases} 0 & \text{if} \quad -\infty < x < -L \\ \frac{Pa[e^{bx} - e^{-bL}]}{1-F^2} & \text{if} \quad -L < x < 0 \end{cases},$$

where a, b, L are real and positive.
This stern shape has the property that the slope $M(x) = \mathrm{d}\eta/\mathrm{d}x$ is continuous for all $x < 0$. This shape is chosen to illustrate the behaviour of the solutions for plate shapes whose slopes are monotonically increasing in x. The actual form of this stern shape is not particularly important; however, the advantage of using the exponential in this stern shape is that it has a straightforward Fourier transform. For our calculations, we fix $b = 1$ and $L = 1$, and observe the effect of varying the single parameter, a, for a fixed pressure, P, and Froude number, F; investigation suggests that the results for other values of b and L are qualitatively similar.

Figure 4.16(a) shows free surface profiles for $F = 0.5$ and $P = 0.01$ calculated using the linear solution, equation (2.30). Note that, because the linear solution is derived using $P/(1 - F^2)$ as the small parameter, linearised free surface profiles for other values of $P/(1 - F^2)$ (with the remaining parameter values fixed) are the same shape, only stretched in the y-direction. In figure 4.16(a), the special value $a = 0$ corresponds to the case of a flat plate considered in McCue and Stump[85]. Note that increasing a from $a = 0$ increases the slope of the plate. We see that, for increasing a, the amplitude of the waves first decreases then increases, suggesting that there is a minimum value of the wave amplitude for a finite value of $a > 0$. This dependence is made more explicit in figure 4.17, where the dashed curve is the amplitude A from equation (2.33) plotted against a for these parameter values. A local minimum is found at approximately $a = 3.725$.

Figure 4.16(b) shows nonlinear free surface profiles computed using the numerical scheme in Section 3.2.3(Chapter 3), while the solid curve in figure 4.17 provides the dependence of the wave amplitude on the parameter a using the same numerical scheme. The linear and nonlinear curves in figure 4.17 are not in exact agreement, which is expected, as the linear approximation ignores terms that are $\mathcal{O}\left(P^2/(1-F^2)^2\right)$. However, there is general qualitative agreement, with the numerical solution to the fully nonlinear problem giving a local minimum in the wave amplitude of approximately $a = 3.15$. The free surface profiles in figure 4.16(b) are plotted for the equally spaced values of a between $a = 0, \ldots, 3.9$, showing that, as the parameter a passes through $a = 3.15$, the phase of the waves changes but the amplitude does not vanish.

Also included in figure 4.17 is a plot of the wave amplitude A versus the parameter a, computed using the weakly nonlinear theory of Section 4.2. As expected, this curve does not agree very well with the other two at all, as the weakly nonlinear theory applies when $1 - F \ll 1$, while this figure is for $F = 0.5$.

The free surface profiles shown in figures 4.18 (a) and (c) are for $F = 0.5$, $P = 0.01$, $b = 1$, $L = 1$ and the local minimum, $a = 1$ and 3.15, respectively. The phase trajectories are shown in figures 4.18 (b) and (d) for the weakly nonlinear solution. We note that, as the Froude number decreases the wave amplitude also decreases for $a = 3.3$, $b = 1$, $L = 1$ and $P = 0.01$, as shown in figure 4.19.

Figure 4.20 shows the relation between the amplitude A and the parameter a for $F = 0.9$ and $P = 0.01$. For these values of the parameter, the linear solution does not agree well with the other two solutions, as the linear solution breaks down as $F \to 1$. The free surface profile for the linear, nonlinear and the weakly nonlinear solutions at the local minimum, $a = 0.7$, 0.45 and 0.4, are shown in figure 4.21 (a), (c) and (e), respectively. In addition, the phase trajectories are shown in figure 4.21 (b), (d) and (f) for the weakly nonlinear solution, which is described as follows. We begin at the origin of the phase plane, which represents the horizontal flat bottom of the plate, and then move along the black curved part, at the separation point between the curved plate and the free surface, until we reach the periodic wave orbit.

We conclude, for this family of plate shapes, the wave amplitude from the linear,

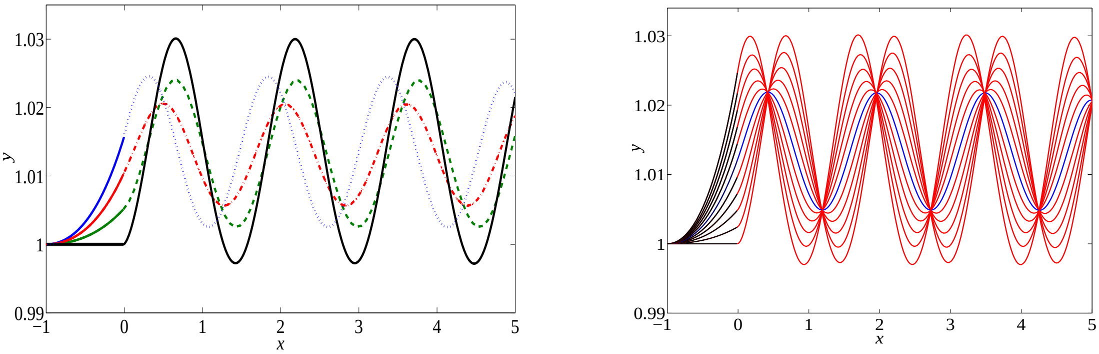

(a) (b)

FIGURE 4.16: Free surface profiles drawn for $F = 0.5$, $P = 0.01$, $b = 1$ and $L = 1$. (a) Linear solutions with $a = 0$ (solid black), 1.5 (green dashed), 3 (red dot-dashed) and 4.5 (blue dot). (b) Nonlinear solutions for $a = 0, \ldots, 3.9$.

nonlinear and weakly nonlinear solutions can be minimised.

4.5.2 Downward Pointing Sterns

We now consider a plate shape described by

$$M(x) = \begin{cases} 0 & \text{if} \quad -\infty < x < -\pi \\ -\frac{1}{2}\alpha \sin(x) + \beta \Big[\cos(x) + \cos(2x) \Big] & \text{if} \quad -\pi < x < 0 \end{cases},$$

where α and β are real numbers.

In this family of stern shapes, we generalise the stern shapes treated by Binder in Section 4.4, noting that, for $\beta > 0$, the stern has a distinctive downward-angle at the detachment point. As with both families of stern shapes that were presented by Binder in Section 4.4 and the shape in Section 4.5.1, we have specified this shape such that the slope is continuous for all x. Further, this form of stern shape is easily amenable to Fourier transform, allowing us to apply the linear theory (2.30).

In figure 4.22 we show plots of amplitude versus β for the same parameter values as in figure 4.8. This figure shows that, as β is increased from $\beta = 0$, the

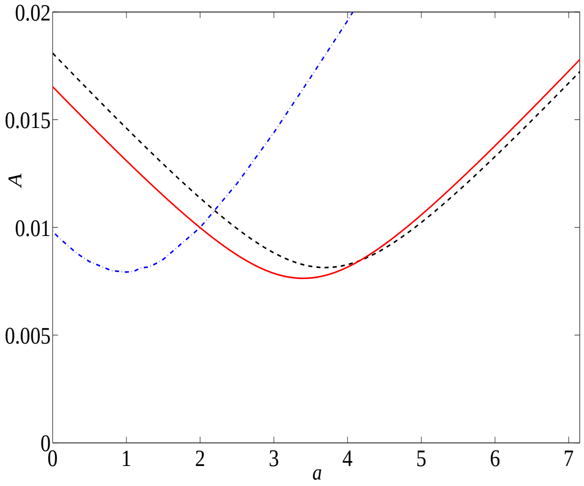

FIGURE 4.17: The dependence of the wave amplitude A on the parameter a for $F = 0.5$ and $P = 0.01$. The red solid curve, black solid curve and blue dot-dashed curved correspond to the fully nonlinear, linear and weakly nonlinear solutions, respectively.

wave amplitude decreases until a minimum is reached. In particular, for the values $\alpha = 0.0427$ and $\beta = 0$ the amplitude is $A = 0.00019$, but the local minimum is $A = 0.00001$, which occurs for roughly $\beta = 0.001$. Thus, by allowing the stern to have a very slightly downward pointing shape at the detachment point, we are able to reduce the initially small wave amplitude for the shape in Section 4.4 by an order of magnitude.

Figure 4.23 shows the dependence of amplitude on β for $F = 0.5$, $P = 0.04$ and $\alpha = 0.0527$. These parameter values correspond to the local minimum amplitude in the fully nonlinear case in figure 4.14. Again, increasing β from $\beta = 0$ introduces a slightly downward pointing stern shape at the detachment point, and we see that, for the value $\beta = 0.0004$, the amplitude is minimised to be $A = 0.00005$, which is considerably smaller in this context. Indeed, the free surface profile for this set of parameters is illustrated in figure 4.24, showing that, effectively, the wavetrain has been eliminated entirely. Also for the linear case as shown in figure 4.25(b) for $F = 0.5$, $P = 0.01$, $\alpha = 0.00135$ and $\beta = 0.004$, the minimum amplitude is very

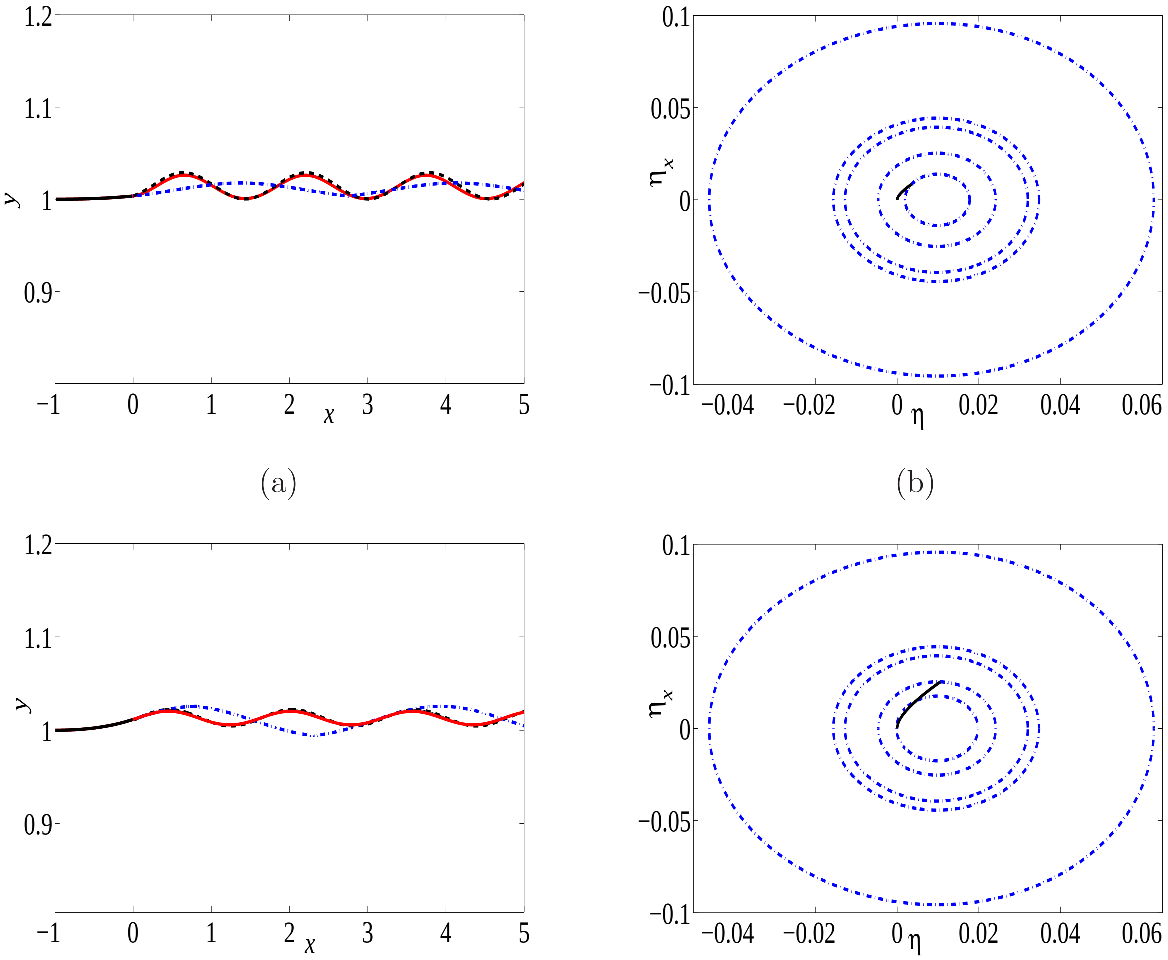

(a) (b)

(c) (d)

FIGURE 4.18: This figure shows the comparison between the analytic, numerical and the weakly nonlinear solution. The free surface profile are shown in figures (a) and (c) and phase trajectories are shown in figure (b) and (d) with the Froude number $F = 0.5$ and $P = 0.01$ at $a = 1, 3.15$ respectively.

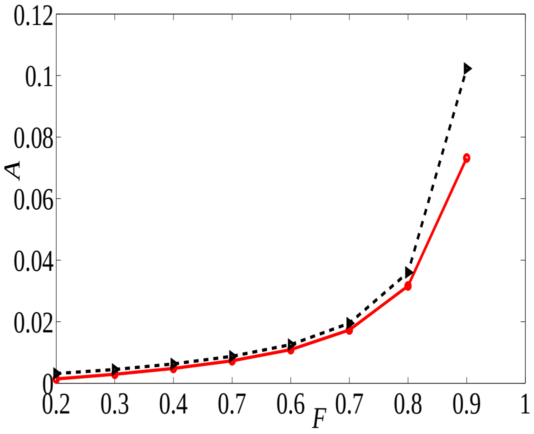

FIGURE 4.19: The dependence of the wave amplitude A on the Froude number F for $a = 3.15$, $b = 1$, $L = 1$ and $P = 0.01$.

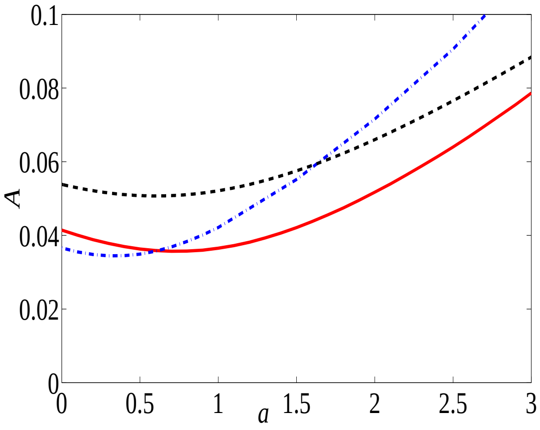

FIGURE 4.20: The dependence of the wave amplitude A on the parameter a for $F = 0.9$ and $P = 0.01$. The red solid curve, black solid curve and blue dot-dashed curve correspond to the fully nonlinear, linear and weakly nonlinear solutions, respectively.

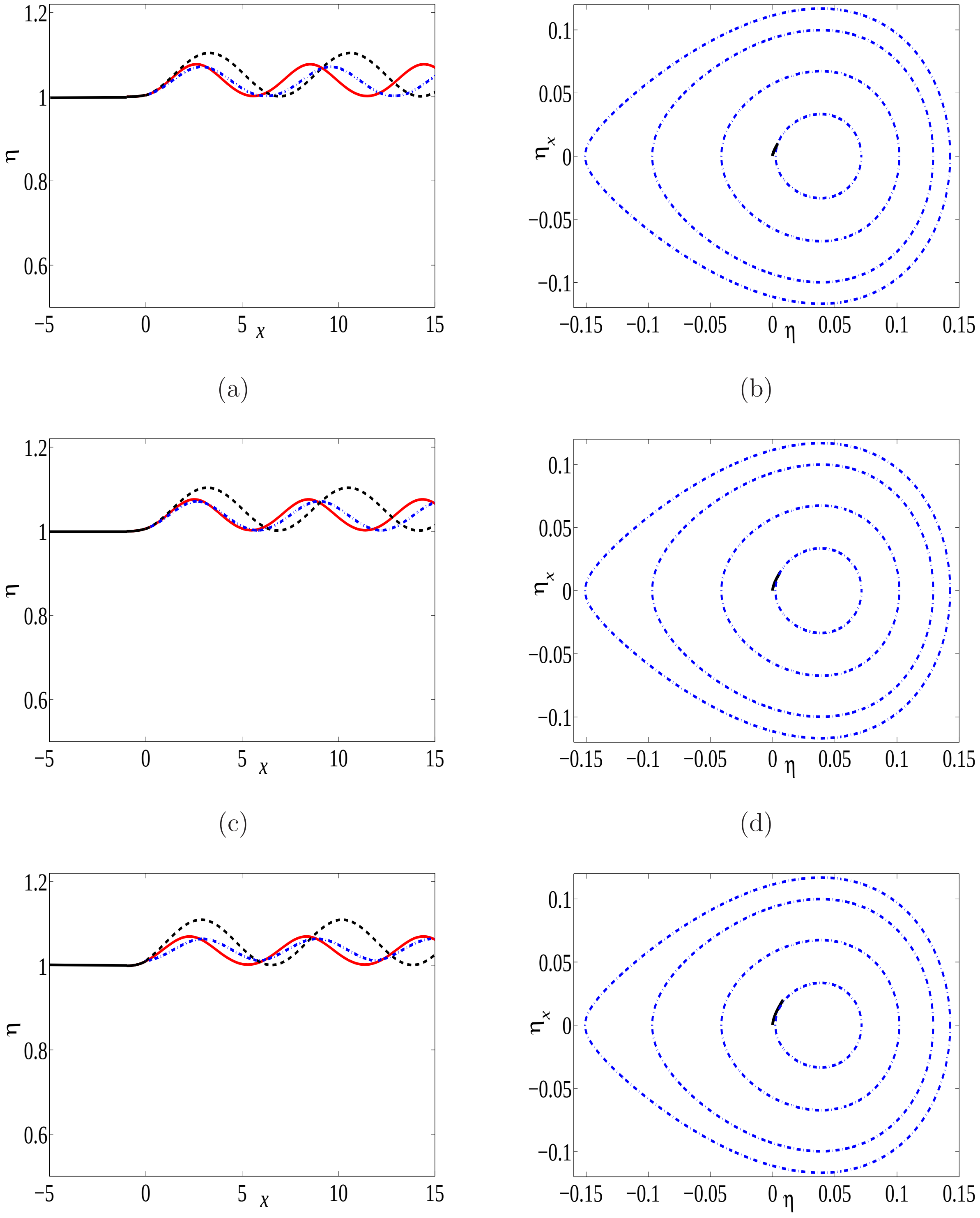

(a) (b)

(c) (d)

(e) (f)

FIGURE 4.21: This figure shows the comparison between the analytic, numerical and the weakly nonlinear solution. The free surface profile are shown in figures (a), (c) and (e) and phase trajectories are shown in figure (b), (d) and (f), with the Froude number $F = 0.9$ and $P = 0.01$ at $a = 0.7, 0.45$, and 0.4 respectively.

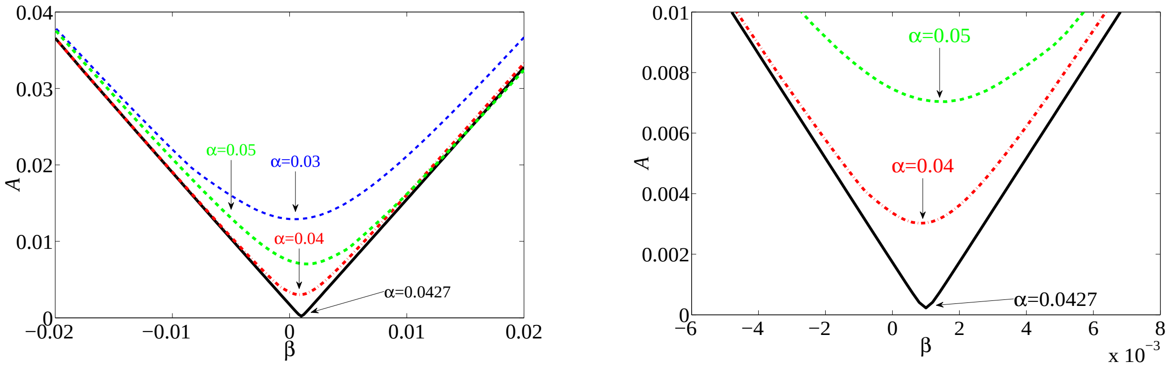

(a) (b)

FIGURE 4.22: The dependence of the wave amplitude A on the parameter β for the nonlinear solution for $F = 0.9$, $P = 0.01$, for the values $\alpha = 0.03$, 0.04, 0.0427 and 0.05.

small (approximately $A = 0.000076425$) which is also considerably small in the context. To illustrate the minimum wave amplitude, the linear and nonlinear free surface profiles for $\alpha = 0.00135$ and $\beta = 0.004$ are presented in figure 4.26 (a) and (b) at different scales, with amplitude $A = 1.13651 \times 10^{-4}$ and $A = 7.6425 \times 10^{-5}$, respectively.

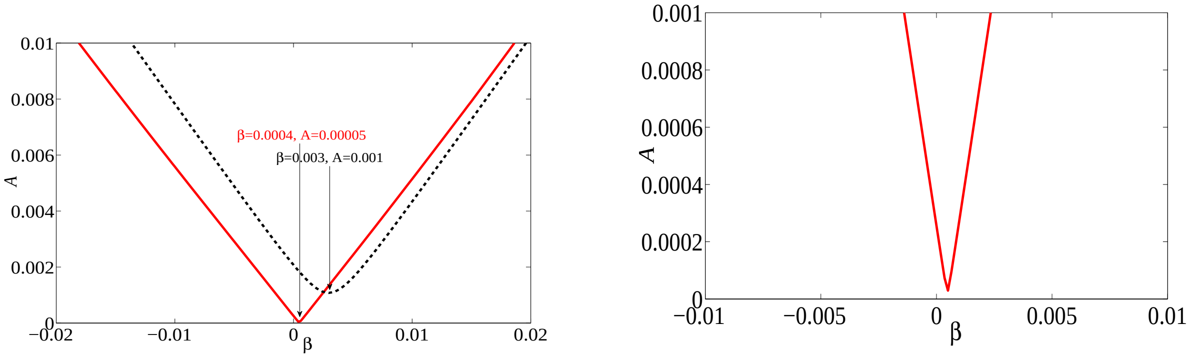

(a) (b)

FIGURE 4.23: The dependence of the wave amplitude A on the parameter β for $F = 0.5$, $P = 0.04$ and $\alpha = 0.0527$. The red solid curve and black dashed curve correspond to the fully nonlinear and linear solution, respectively.

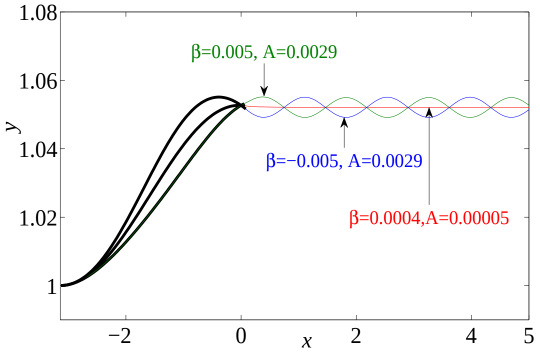

FIGURE 4.24: Nonlinear free surface profiles drawn for $F = 0.5$, $P = 0.04$ and $\alpha = 0.0527$ with $\beta = -0.005$, 0.0004 and 0.005 with amplitude $A = 0.0029$, 0.00005 and 0.0029, respectively.

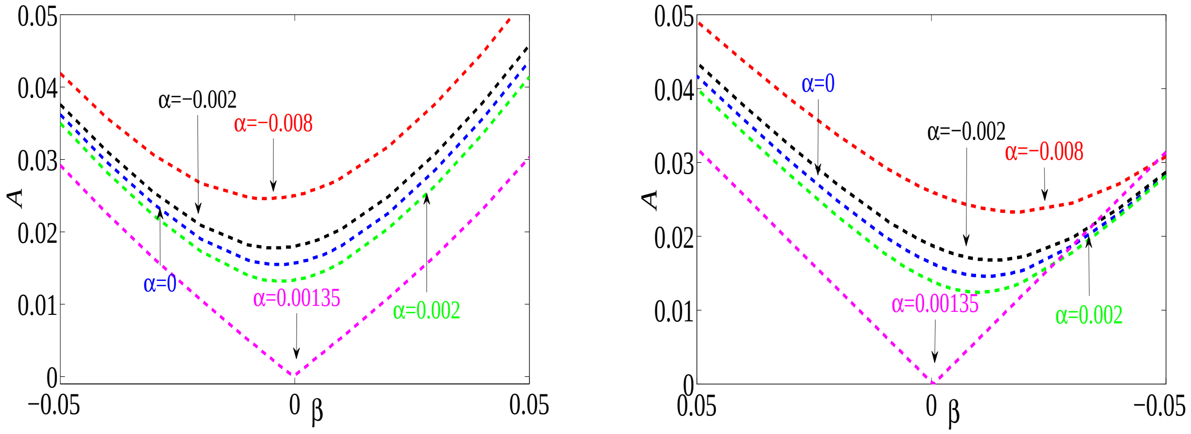

(a) (b)

FIGURE 4.25: The dependence of the wave amplitude A on the parameter β for $F = 0.5$, $P = 0.01$ and different values of α, $\alpha = -0.008, -0.002, 0, 0.002, 0.00135$. (a) nonlinear solution, (b) linear solution.

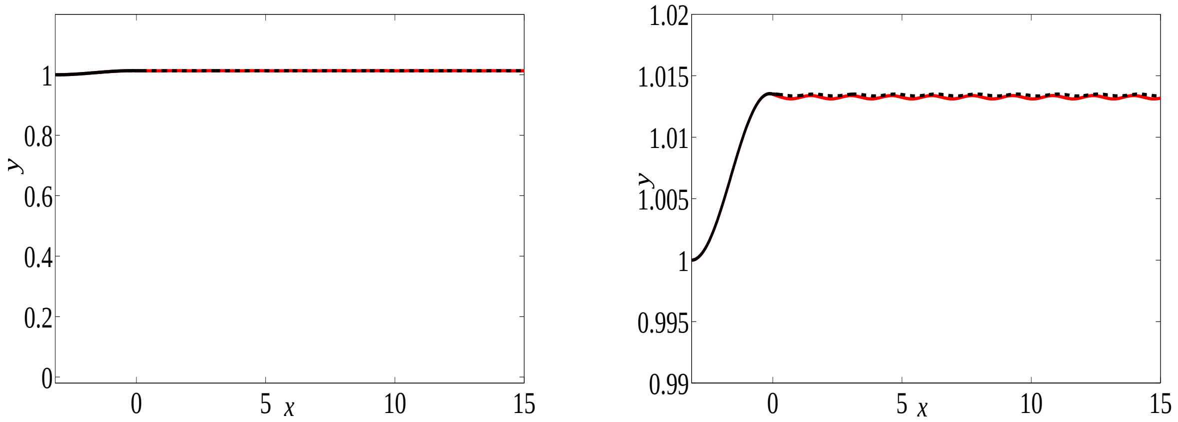

(a) (b)

FIGURE 4.26: Figure (a) and (b), show the free surface profile for different scale, for the analytical and numerical solution. The Froude number $F = 0.5$, $P = 0.01$, $\alpha = 0.00135$ with the local minimum $\beta = 0.004$.

Now, we will summaries the three main results of this Chapter. First, the linear free surface flow problem has mixed boundary conditions, and is therefore much more difficult to solve than the well-studied problems of flow over a bottom topography, or flow due to a pressure distribution, for example. Even taking into account the normal issues arising from applying the Wiener–Hopf technique, a challenging feature of the present problem is that for plate shapes that have slopes with compact support ($\mathrm{d}\eta/\mathrm{d}x = 0$ for $x < -L$ with $L > 0$), we are unable to close the contour of integration in the more natural upper half-plane, and instead have to deal with the significant algebra that accompanies closing the contour in the lower half-plane (note that this aspect was not present in the flat plate problem considered by McCue and Stump [85], since the function $J(k)$ was identically zero in that case). Furthermore, an additional subtlety associated with the present problem is that the term $J_+(k)$ provides the leading order behaviour in (2.42) for large k, being $\mathcal{O}(k^{-1})$ in the limit $k \to \infty$, with the other term $P_+(k)\hat{m}_+(k) = \mathcal{O}(k^{-3/2})$. On the other hand, for the case of the flat plate, the scalings change completely, as the function $J_+(k)$ vanishes, and the term $P_+(k)\hat{m}_+(k)$ transitions to being $\mathcal{O}(k^{-2})$.

Second, the weakly nonlinear analysis of Section 4.2 (and applied in other free surface flow problems in [8, 9, 10, 11]) is relatively simple to apply, and gives very good approximate solutions to the full nonlinear problem provided $1 - F \ll 1$ and $P \ll 1$. As shown by Binder [11], the theory can be used to predict plate shapes that are candidates for eliminating the downstream waves on the free surface. Upon closer inspection, we find that for these plate shapes, numerical solutions to the full nonlinear equations do in fact exhibit waves, although with such small amplitudes that the waves are unable to be detected on a scale that includes the channel bottom.

Third, by taking these solutions with very small wave amplitudes, we have been able to reduce the amplitude even further by adjusting the geometry of the plate so that it points slightly downwards at the point of detachment (as suggested for the infinite depth problem by Schmidt [30], Madurasinghe and Tuck [66] and Farrow and Tuck [13]). Indeed, given the inevitable numerical error associated with our numerical scheme, for these solution we may even claim that the waves are entirely eliminated.

Much attention has been devoted to the question of whether or not we can adjust the shape of the semi-infinite plate to eliminate the waves that appear on the downstream free surface. For practical purposes, this motivation is linked to the well-known idea that there is energy associated with wave drag behind ships, and it is desirable to design stern shapes that minimise this energy loss by minimising the wave amplitude. For free surface flow problems in two dimensions, there is also the mathematical interest in discovering particular subcritical solutions that are non-generic in the sense that they exhibit free surfaces that are flat far downstream, remembering that the general outcome for that parameter regime is to have a train of period waves on the surface in the limit. Furthermore, for configurations that completely eliminate the waves downstream, the flow direction can be reversed (since the radiation condition would no longer apply), resulting in a bow flow solution. In this case, a single (isolated) bow flow solution may also be a member of a completely different family of solutions, such as those with a splash near the bow, for example.

For the linearised problem of free surface flow past a semi-infinite curved plate in a fluid of finite depth, we have derived a (rather complicated) formula (2.33) for the wave amplitude that depends on the shape of the plate as well as the Froude number F. For the families of plate shapes treated in this chapter, the amplitude was not eliminated, but this does not preclude the possibility of setting up more general families of plate shapes, and using optimisation to eliminate the downstream waves. For the corresponding linear problem in infinite depth, such an approach is suggested by Zhu and Zhang [87], and even undertaken by Schmidt [30]. Unfortunately, as Schmidt [30] does not show the corresponding free surface profiles, it is not clear whether his scheme actually worked.

Regardless of the results of any such linear approach, our experience in the present study is that care must be given to any prediction from an approximate linear or weakly nonlinear theory, as it may be that these theories predict solutions without waves, when the fully nonlinear problems do in fact exhibit waves, albeit with a very small amplitude. Indeed, even with numerical solutions to the fully nonlinear equations, it may appear that waves are completely eliminated (as for the infinite depth problem studied by Madurasinghe and Tuck [66] and Farrow and Tuck [13]), when in fact they are just too small to detect using the numerical resolution available.

In this Chapter, the problem of the free surface flow past a curved plate for three families of plate shapes was investigated analytically, numerically and using the weakly nonlinear approximation. Comparison with results in the literature reported and the results for the new stern shape showed good agreement for the three solutions. The wave amplitude was eliminated for plate shapes that has a downward point at the detachment with the free surface for the nonlinear and weakly nonlinear solutions.

In the next chapter, the unsteady free surface flow past a semi-infinite flat plate in a fluid of finite depth will be investigated.

Chapter 5

Linearised Unsteady Flow Problem

5.1 Introduction

In the previous chapters, steady two-dimensional free surface flow past a semi-infinite curved plate in a fluid of finite depth was investigated analytically, numerically and using the weakly nonlinear approximation. In this chapter a transient free surface flow past a two-dimensional semi-infinite flat plate in a fluid of finite depth is investigated analytically using Laplace transform and the Wiener–Hopf technique. The linearised problem is solved under the assumption that the plate is submerged into the fluid at a small depth d below the free surface at $\tilde{t} > 0^+$. This unsteady problem has previously been approached analytically by Zhu and Zhang [87] via the Wiener–Hopf technique, assuming the free surface flow past a semi-infinite plate in a fluid of infinite depth. Also Haussling [32] treated linear and nonlinear problems numerically for the ship model with Froude numbers $\mathrm{Fr} \equiv V/\sqrt{gd} \in [1,4]$. (Notice that this definition of the Froude number differs from the depth-defined Froude number $F \equiv V/\sqrt{gh}$ used here, where h is the fluid depth. The relationship between these two definitions is $F = \mathrm{Fr}\sqrt{d/h}$. Therefore in our notations, the results obtained by Haussling[32] pertain to small Froude numbers because usually $d/h \ll 1$.)

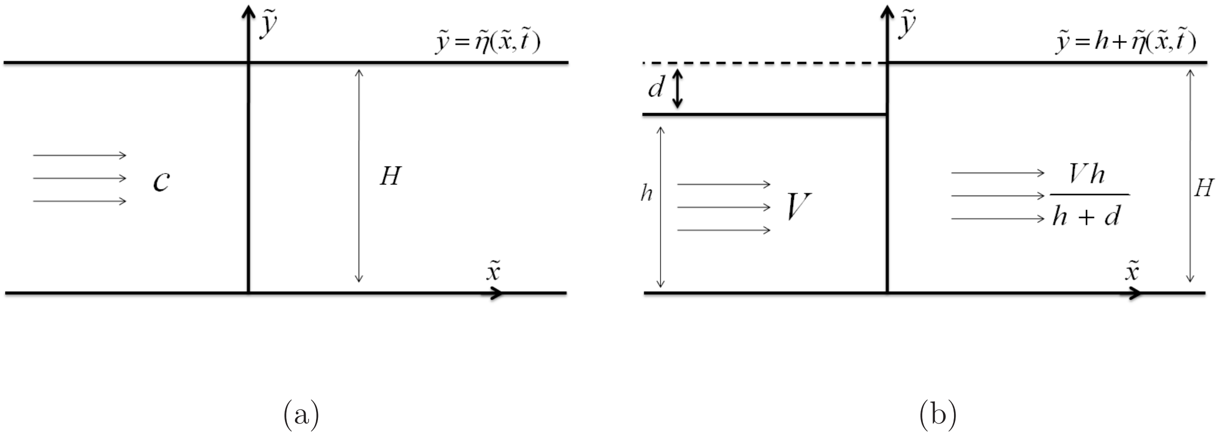

FIGURE 5.1: Sketch of free surface flow past a semi-infinite flat plate in a fluid of finite depth. In figure (a), the plate is located at the level of the undisturbed free surface, whereas in figure (b) the plate is suddenly submerged into the fluid for $\tilde{t} > 0^+$.

5.1.1 Mathematical Formulation

Unsteady two-dimensional free surface flow past a semi infinite plate in a fluid of finite depth is considered, as shown in figure 5.1(a). We assume that the fluid is inviscid and incompressible, and that the flow is irrotational. Cartesian coordinates are introduced so that the $\tilde{x}-$axis lies on the bottom of the plate and the $\tilde{y}$-axis is directed vertically upwards. For $\tilde{x} < 0$, $\tilde{t} = 0$, the fluid is bounded above by a semi-infinite flat plate, and for $\tilde{x} > 0$, $\tilde{t} = 0$, the upper boundary consists of the free surface. It is assumed that the flow for $\tilde{x} < 0$ is that of a uniform stream of depth H and speed c, as shown in figure 5.1(a).

Now, suppose the plate is depressed into the fluid a distance d below the level of the undisturbed free surface at $\tilde{t} > 0^+$, as shown in figure 5.1(b). The distance between the horizontal bottom and the plate is h so that $H = h+d$. Assuming that the fluid upstream is uniform with a constant depth h and speed V, the velocity downstream, by conservation of mass, is $Vh/(h+d)$.

As the flow is irrotational, the $\tilde{x}$ and $\tilde{y}$ components of the velocity field can be expressed through the velocity potential Φ:

$$\tilde{u} = \frac{\partial \Phi}{\partial \tilde{x}}, \quad \tilde{v} = \frac{\partial \Phi}{\partial \tilde{y}}, \quad \forall \tilde{t} \geq 0, \tag{5.1}$$

Substituting these expressions into the continuity equation, $\nabla.\mathbf{v} = 0$, we obtain as usual the Laplace equation for the velocity potential Φ:

$$\nabla^2 \Phi = \frac{\partial^2 \Phi}{\partial \tilde{x}^2} + \frac{\partial^2 \Phi}{\partial \tilde{y}^2} = 0, \quad \text{for} \quad -\infty < \tilde{x} < \infty, \quad \text{on} \quad 0 < \tilde{y} < h + \tilde{\eta}(\tilde{x}, \tilde{t}), \quad \forall \tilde{t} \geq 0. \tag{5.2}$$

Two boundary conditions are required at the free surface, as the surface position, $\tilde{\eta}$, and Φ have to be determined. We obtain one boundary condition by requiring that the fluid velocity is tangential to the free surface, namely,

$$\frac{\partial \tilde{\eta}}{\partial \tilde{t}} + \frac{\partial \Phi}{\partial \tilde{x}} \frac{\partial \tilde{\eta}}{\partial \tilde{x}} = \frac{\partial \Phi}{\partial \tilde{y}}, \quad \text{for} \quad \tilde{x} > 0, \quad \text{on} \quad y = h + \tilde{\eta}(\tilde{x}, \tilde{t}), \quad \forall \tilde{t} \geq 0. \tag{5.3}$$

To obtain the second boundary condition, we apply Bernoulli's equation along the free surface,

$$\frac{\partial \Phi}{\partial \tilde{t}} + \frac{1}{2}(\tilde{u}^2 + \tilde{v}^2) + g\tilde{y} = \frac{1}{2}V^2 + gh + \frac{\tilde{P}}{\rho}, \quad \text{for} \quad \tilde{x} > 0, \quad \text{on} \quad \tilde{y} = h + \tilde{\eta}(\tilde{x}, \tilde{t}), \quad \forall \tilde{t} \geq 0, \tag{5.4}$$

where ρ is the density, g is the acceleration due to gravity, $\tilde{P} = P_{-\infty} - P_a$, $P_{-\infty}$ is the constant pressure at $\tilde{x} < 0$, and P_a is the atmospheric pressure on the free surface.

At the solid boundaries, namely the flat plate ($\tilde{x} < 0$) and the bottom of the fluid ($\tilde{y} = 0$), the normal component of the fluid velocity must be zero. This gives,

$$\frac{\partial \Phi}{\partial \tilde{y}} = 0, \quad \text{for} \quad -\infty < \tilde{x} < 0, \quad \text{on} \quad \tilde{y} = h, \quad \forall \tilde{t} \geq 0, \tag{5.5}$$

$$\frac{\partial \Phi}{\partial \tilde{y}} = 0, \quad \text{for} \quad -\infty < \tilde{x} < \infty, \quad \text{on} \quad \tilde{y} = 0, \quad \forall \tilde{t} \geq 0, \tag{5.6}$$

with h being constant.

To complete the formulation of the unsteady problem, two initial conditions are needed. Assuming that the flow is uniform upstream with velocity potential $\Phi = V\tilde{x}$ and downstream with $\Phi = (\frac{Vh}{h+d})\tilde{x}$ as shown in figure 5.2, we find that the initial condition for the velocity potential is given by

$$\Phi(\tilde{x}, \tilde{y}, \tilde{t}) = \left[\left(\frac{Vh}{h+d} - V\right) H(\tilde{x}) + V\right] \tilde{x}, \quad \text{at} \quad \tilde{t} = 0, \tag{5.7}$$

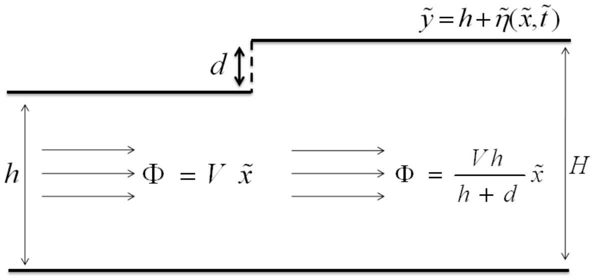

FIGURE 5.2: A schematic of the free surface flow past a flat plate with velocity potential upstream given by $\Phi = V\tilde{x}$ and velocity potential downstream given by $\Phi = (\frac{Vh}{h+d})\tilde{x}$.

---

where $H(\tilde{x})$ is the Heaviside function.

The initial position of the free surface at $y = H$ can be considered as a perturbation of a height $d << H$ relative to the level of the plate $y = h$. Then we obtain the following initial condition for the free surface, namely,

$$\tilde{\eta}(\tilde{x}, \tilde{t}) = dH(\tilde{x}) \quad \text{at} \quad \tilde{t} = 0. \tag{5.8}$$

Equations (5.2)–(5.8) form the mixed boundary-value problem with given initial conditions for the unknown functions, free surface $\tilde{\eta}(\tilde{x}, \tilde{y}, \tilde{t})$ and velocity potential $\Phi(\tilde{x}, \tilde{y}, \tilde{t})$. To solve this problem, it is convenient firstly to reduce it to the dimensionless form. To this end, let us scale all spatial coordinates by the height h, and all velocities by the upstream speed V; that is we let $x = \tilde{x}/h$, $y = \tilde{y}/h$, $\eta = \tilde{\eta}/h$, $v = \tilde{v}/V$, $u = \tilde{u}/V$, $\phi = \Phi/Vh$, $t = V\tilde{t}/h$, and also $P = \tilde{P}/\rho g h$. Then, the Laplace equation (5.2), as shown in figure 5.3, in the domain

$$D : \quad \begin{cases} -\infty < x < 0, \quad 0 < y < 1; \\ \\ 0 \leq x < \infty, \quad 0 < y < 1 + \eta(x, t) \end{cases}$$

reads

$$\frac{\partial^2 \phi}{\partial x^2} + \frac{\partial^2 \phi}{\partial y^2} = 0 \quad \text{for } \forall t \geq 0. \tag{5.9}$$

And the boundary conditions (5.3)–(5.4) at the free surface $x > 0$, $y = 1 + \eta(x,t)$ for $\forall t \geq 0$ become:

$$\frac{\partial \eta}{\partial t} + \frac{\partial \phi}{\partial x}\frac{\partial \eta}{\partial x} = \frac{\partial \phi}{\partial y}; \tag{5.10}$$

$$\frac{\partial \phi}{\partial t} + \frac{1}{2}(u^2 + v^2) + \frac{\eta}{F^2} = \frac{1}{2} + \frac{P}{F^2}. \tag{5.11}$$

It is assumed that the thickness of the plate is not zero, but is greater than the depth of the plate submerging, d (the plate models a submerged platform or a ship). In this case there is no back flow of fluid into the region above the plate. The boundary conditions at the rigid plate (5.5) and bottom (5.6) reduce to:

$$\frac{\partial \phi}{\partial y} = 0 : -\infty < x < 0,\ y = 1,\ \forall t \geq 0 \quad \text{at the plate}, \tag{5.12}$$

$$\frac{\partial \phi}{\partial y} = 0 : -\infty < x < \infty,\ y = 0,\ \forall t \geq 0 \quad \text{at the bottom}. \tag{5.13}$$

The initial conditions (5.7)–(5.8) in the dimensionless variables read

$$\phi(x,y,0) = \left[1 - \frac{\epsilon}{1+\epsilon}H(x)\right]x \approx \left[1 - \epsilon H(x)\right]x, \tag{5.14}$$

$$\eta(x,0) = \epsilon H(x), \tag{5.15}$$

where $\epsilon = d/h \ll 1$ is the small parameter. The other two dimensionless parameters, the Froude number F and the applied pressure P, were introduced as

$$F = \frac{V}{\sqrt{gh}}, \quad P = \frac{P_{-\infty} - P_a}{\rho g h}. \tag{5.16}$$

The boundary conditions (5.9)-(5.13) can be reduced to the steady state problem derived in Chapter 2, if we omit all temporal derivatives letting $\partial t = 0$.

In the following section we linearise the problem (5.9)–(5.13) and solve it by means of Laplace transform and Wiener–Hopf technique. The formal solution can be presented in quadrature in the form of definite integrals. To calculate the integrals we use numerical approximation of the contour integrals in the complex plane exploiting the best rational approximation method suggested by Trefethen *et al.* [57].

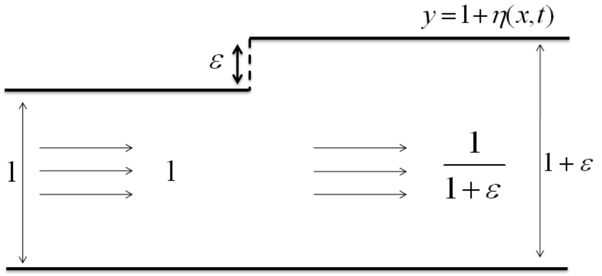

FIGURE 5.3: A schematic for the non-dimensional unsteady problem for $t > 0^+$, where $\epsilon = d/h$ is the non-dimensional distance between the height of the plate and the undisturbed free surface.

5.1.2 Linearised Stern Flow Problem

In this section, we linearise the boundary conditions (5.9)-(5.13) under the assumption that $P/(1-F^2) \ll 1$ and solve the resultant linear equations exactly using the Wiener–Hopf technique.

Note then that without the external pressure exerting on the plate (i.e., when $P = 0$) the problem posted above has the trivial unperturbed solution which represent the uniform stream:

$$\phi = x, \quad \eta = 0, \tag{5.17}$$

which is formally valid for all Froude numbers F.

When a small external pressure is applied on the plate, the solution of the linearised problem (5.9)–(5.13) can be considered as weakly perturbed stationary solution (5.17):

$$\phi(x,y,t) = x + \frac{P}{1-F^2}\phi_1(x,y,t) + \mathcal{O}\left(\frac{P^2}{(1-F^2)^2}\right), \tag{5.18}$$

$$\eta(x,t) = \frac{P}{1-F^2}[1+\eta_1(x,t)] + \mathcal{O}\left(\frac{P^2}{(1-F^2)^2}\right). \tag{5.19}$$

By applying the linearisation (5.18)–(5.19) to equations (5.9)–(5.13), we find the function $\phi_1(x,y,t)$ satisfies the Laplace equation in the fluid domain $D : -\infty <$

$x < \infty, \quad 0 < y < 1, \quad \forall t \geq 0$:

$$\frac{\partial^2 \phi_1}{\partial x^2} + \frac{\partial^2 \phi_1}{\partial y^2} = 0, \tag{5.20}$$

and boundary condition at the bottom:

$$\frac{\partial \phi_1}{\partial y} = 0 : \quad -\infty < x < \infty, \quad y = 0, \quad \forall t \geq 0. \tag{5.21}$$

The boundary conditions on the free surface and rigid plate in the linear approximation can be presented as ($-\infty < x < \infty$ and $y = 1$ for $\forall t \geq 0$):

$$\frac{\partial \phi_1}{\partial y} + F^2 \left[\frac{\partial^2 \phi_1}{\partial t^2} + 2\frac{\partial}{\partial t}\left(\frac{\partial \phi_1}{\partial x}\right) - \frac{\partial^2 \phi_1}{\partial y^2} \right] = n(x,t), \tag{5.22}$$

$$\frac{\partial \phi_1}{\partial y} = m(x,t), \tag{5.23}$$

where $m(x,t) \equiv 0$ at the flat plate, $x < 0$, and $m(x,t)$ is the unknown function describing the free surface at $x > 0$. The function $n(x,t) \equiv 0$ at the free surface, $x > 0$, and $n(x,t) \equiv P$ at $x < 0$.

The initial conditions (5.14)–(5.15) in the linear approximation become:

$$\phi_1(x,y,0) = -xH(x), \tag{5.24}$$

$$\eta_1(x,0) = -1 + H(x). \tag{5.25}$$

Finally, given the solution to equations (5.20)–(5.25), the shape of the free surface can be recovered for $x > 0, \quad y = 1$ and $\forall t \geq 0$ via the equation

$$\eta(x,t) = \frac{P}{1-F^2}\left[1 - F^2\left(1 + \frac{\partial \phi_1}{\partial t} + \frac{\partial \phi_1}{\partial x}\right)\right]. \tag{5.26}$$

In the next section, the linearised problem (5.20)–(5.25) is solved using the Laplace transform method together with the Wiener–Hopf technique.

5.2 Wiener–Hopf technique

5.2.1 Application of the Laplace and Fourier Transforms

The differential system (5.20)-(5.25) is solved using the Wiener–Hopf technique. Before doing that, we apply the Laplace transform to functions ϕ_1, m and n:

$$\tilde{\phi}(x,y,s) = \int_0^\infty \phi_1(x,y,t)e^{-st}dt, \qquad \text{and} \qquad \tilde{m}(x,s) = \int_0^\infty m(x,t)e^{-st}dt, \tag{5.27}$$

and

$$\tilde{n}(x,s) = \int_0^\infty n(x,t)e^{-st}dt. \tag{5.28}$$

It is assumed that there is a real number α such that these transforms exist for $\mathrm{Re}(s) > \alpha$. Application of the Laplace transform to the boundary conditions (5.20)-(5.21) gives

$$\nabla^2\tilde{\phi} = 0, \quad \text{for} \quad -\infty < x < \infty, \quad 0 < y < 1, \tag{5.29}$$

$$\tilde{\phi}_y = 0, \quad \text{for} \quad -\infty < x < \infty, \quad y = 0. \tag{5.30}$$

And Laplace transform of equation (5.22)–(5.23) gives at $y = 1$ and $-\infty < x < \infty$:

$$\tilde{\phi}_y + F^2\Bigg[s^2\tilde{\phi} + 2s\tilde{\phi}_x - \tilde{\phi}_{yy} + 2x\delta(x) + (sx+2)H(x)\Bigg] = \tilde{n}(x,s), \tag{5.31}$$

$$\tilde{\phi}_y = \tilde{m}(x,s), \tag{5.32}$$

where $m(x,s) = 0$ for $x < 0$ and $n(x,s) = 0$ for $x > 0$, and assume that

$$m(x,s) = \mathcal{O}(\mathrm{e}^{\tau_+ x}), \quad n(x,s) = \mathcal{O}(\mathrm{e}^{\tau_+ x}) \quad \text{as} \quad x \to -\infty,$$

where $\tau_+ > 0$ is left unspecified.

Next, we define the Fourier transform of $\tilde{\phi}$ with respect to x in (5.27) as

$$\hat{\tilde{\phi}}(k,y,s) = \int_{-\infty}^\infty \tilde{\phi}(x,y,s)e^{ikx}dx. \tag{5.33}$$

This Fourier transform does not converge for real values of k, but instead must hold in the infinitely long strip $0 < \mathrm{Im}(k) < \tau_+$ that can be detected by the far field behaviour of the function $\tilde{\phi}(x,y,s)$.

By applying the Fourier transform to (5.29) yields

$$\frac{d^2\hat{\tilde{\phi}}}{dy^2}(k,y,s) - k^2\hat{\tilde{\phi}}(k,y,s) = 0, \tag{5.34}$$

which has general solution

$$\hat{\tilde{\phi}}(k,y,s) = A(k,s)\cosh ky + B(k,s)\sinh ky. \tag{5.35}$$

The Fourier transform of the boundary condition (5.30) is

$$\frac{\partial\hat{\tilde{\phi}}}{dy} = 0, \quad \text{at} \quad y = 0, \tag{5.36}$$

which, by substituting (5.36) into (5.35) at $y = 0$, determines that the function $B(k, s) = 0$, therefore solution to (5.35) reduce to

$$\hat{\tilde{\phi}}(k, y, s) = A(k, s)\cosh ky. \tag{5.37}$$

The Fourier transform of boundary conditions (5.31) and (5.32) are given respectively by

$$\frac{\partial\hat{\tilde{\phi}}_1}{\partial y} = \hat{\tilde{m}}(k, s), \tag{5.38}$$

and

$$\hat{\tilde{\phi}}_y - F^2\hat{\tilde{\phi}}_{yy} + [s^2F^2 + 2iF^2ks]\hat{\tilde{\phi}} - \frac{F^2(2ik - s)}{k^2} = \hat{\tilde{n}}(k, s). \tag{5.39}$$

Substituting (5.37) into (5.38) and (5.39), we obtain

$$\hat{\tilde{m}}(k, s) = kA(k, s)\sinh(k), \tag{5.40}$$

and

$$\hat{\tilde{n}}(k, s) = kA(k, s)\sinh(k)G_1(k, s) - \frac{F^2(2ik - s)}{k^2}, \tag{5.41}$$

where

$$G_1(k, s) = \left[1 + \frac{s^2F^2 + 2iF^2ks - F^2k^2}{k\tanh(k)}\right], \tag{5.42}$$

where (5.40) and (5.41) are analytic in the strip $0 < \mathrm{Im}(k) < \tau_+$. Here $\hat{\tilde{n}}(k, s)$ and $\hat{\tilde{m}}(k, s)$ are the Fourier transforms of $\tilde{m}(x, s)$ and $\tilde{n}(x, s)$, respectively. Equations (5.40) and (5.41) can be reduced to the corresponding equation for the steady-state problem presented in Chapter 2, if we put $s = 0$ and omit the last term of equation (5.41).

Eliminating $A(k, s)$ from equations (5.40) and (5.41), we obtain the equation of the unknown function $\hat{\tilde{m}}(x, s)$ in terms of function $\hat{\tilde{n}}(x, s)$:

$$\hat{\tilde{m}}(k, s) = \frac{\hat{\tilde{n}}(k, s) + \frac{F^2(2ik-s)}{k^2}}{G_1(k, s)}. \tag{5.43}$$

Also from equation (5.37) and (5.40) we find

$$\hat{\tilde{\phi}}(k, y, s) = \frac{\cosh ky}{k\sinh k}\hat{\tilde{m}}(k, s). \tag{5.44}$$

Once $\hat{\tilde{m}}(x, s)$ is determined, we can recover the unknown free surface function $\eta(x, t)$ through equations (5.26) and (5.44).

5.2.2 The Wiener–Hopf equation

The first key step of the Wiener–Hopf technique is to factorise the function $G_1(k,s)$ as

$$G_1(k,s) = \frac{1}{k^2} K_+(k,s) K_-(k,s), \tag{5.45}$$

where $K_+(k,s)$ is analytic and non-zero in the upper-half plane, and $K_-(k,s)$ is analytic and non-zero in the lower-half plane (the details of factorisation are presented in Section 5.2.5).

Anticipating the use of the Wiener–Hopf technique, $\hat{\tilde{m}}(x,s)$ and $\hat{\tilde{n}}(x,s)$ can be split into

$$\hat{\tilde{m}}(k,s) = \hat{\tilde{m}}_-(k,s) + \hat{\tilde{m}}_+(k,s), \tag{5.46}$$

$$\hat{\tilde{n}}(k,s) = \hat{\tilde{n}}_-(k,s) + \hat{\tilde{n}}_+(k,s), \tag{5.47}$$

where

$$\hat{\tilde{m}}_-(k,s) = \int_{-\infty}^{0} \tilde{m}(x,s) e^{ikx} dx, \quad \text{and} \quad \hat{\tilde{n}}_-(k,s) = \int_{-\infty}^{0} \tilde{n}(x,s) e^{ikx} dx \tag{5.48}$$

are analytic functions in the lower-half plane, and

$$\hat{\tilde{m}}_+(k,s) = \int_{0}^{\infty} \tilde{m}(x,s) e^{ikx} dx, \quad \text{and} \quad \hat{\tilde{n}}_+(k,s) = \int_{0}^{\infty} \tilde{n}(x,s) e^{ikx} dx$$

are analytic functions in the upper-half plane. Since the plate is flat, so that $m(x,t) = 0$ for $x < 0$, then $\hat{\tilde{m}}_-(k,s) = 0$. Also the atmospheric pressure can be taken to be identically zero for $x > 0$; this gives $\hat{\tilde{n}}_+(k,s) = 0$. taking into account this prosperities, we can present equation (5.43) in the form

$$\hat{\tilde{m}}_+(k,s) = \frac{\hat{\tilde{n}}_-(k,s) + \frac{F^2(2ik-s)}{k^2}}{G_1(k,s)}, \tag{5.49}$$

which is analytic in the strip $0 < \mathrm{Im}(k) < \tau_+$. substituting equation (5.45) into equation (5.49), we obtain the Wiener–Hopf equation

$$\hat{\tilde{m}}_+(k,s) K_+(k,s) = \frac{k^2 \hat{\tilde{n}}_-(k,s)}{K_-(k,s)} + \frac{F^2(2ik-s)}{K_-(k,s)}, \tag{5.50}$$

where the left-hand side represents an analytic function in the upper-half plane, whereas all terms in the right hand-side are analytic in the lower-half plane. Because both sides of equation (5.50) are equal in the strip $0 < \mathrm{Im}(k) < \tau_+$, then the entire function in the left-hand side must be the analytic continuation of the entire function in the right-hand side and vise-versa.

By studying the behavior of the left-hand side of equation (5.50) as $k \to \infty$ in the upper-half plane and the right-hand side of that equation in the lower-half plane, we can conclude on a basis of the Liouville's theorem ([5]) that each side of the equation must be equal to some constant E. Then equation (5.50) becomes

$$\hat{\hat{m}}_+(k,s)K_+(k,s) = \frac{k^2\hat{\hat{n}}_-(k,s)}{K_-(k,s)} + \frac{F^2(2ik-s)}{K_-(k,s)} = E. \tag{5.51}$$

Thus, equation(5.51) for the two unknown functions $\hat{\hat{m}}_+(k,s)$ and $\hat{\hat{n}}_-(k,s)$ is split into two independent equations for each of the functions individually. The equation for the former function gives

$$\hat{\hat{m}}_+(k,s) = \frac{E}{K_+(k,s)}. \tag{5.52}$$

It follows from equation (5.44) that the transformed function $\hat{\hat{\phi}}(k,y,s)$ is given by

$$\hat{\hat{\phi}}(k,y,s) = \frac{E}{K_+(k,s)}\frac{\cosh ky}{k\sinh k}. \tag{5.53}$$

5.2.3 The Location of the Free Surface $\eta_1(x,t)$

In this section the location of the free surface is evaluated as follow:
Substituting equation (5.53) into (5.33), we obtain

$$\hat{\hat{\phi}}(k,y,s) = \int_{-\infty}^{\infty}\left[\int_0^{\infty}\phi_1(x,y,t)e^{-st}dt\right]e^{ikx}dx = \left[\frac{E}{K_+(k,s)}\right]\frac{\cosh ky}{k\sinh k}, \tag{5.54}$$

and applying then the inverse Fourier and Laplace transforms to equation (5.54), we can find the integral representation of the exact solution to the linearised problem for the normalised velocity potential as

$$\phi_1(x,y,t) = \frac{1}{2\pi i}\int_{\gamma-i\infty}^{\gamma+i\infty}\left[\frac{1}{2\pi}\int_{-\infty+i\delta}^{\infty+i\delta}\left[\frac{E}{K_+(k,s)}\right]\frac{\cosh ky}{k\sinh k}e^{-ikx}dk\right]e^{st}ds, \tag{5.55}$$

where γ is a vertical contour for the inverse Laplace transform that is located to the right of all singularities; δ is a real constant in the range $0 < \delta < \tau_+$.
To use the formula for the free surface, equation (5.26), we need to determine the derivative of $\phi_1(x,1,t)$ with respect to x, namely

$$\frac{\partial\phi_1}{\partial x}(x,1,t) = \frac{1}{2\pi i}\int_{\gamma-i\infty}^{\gamma+i\infty}\left[\frac{1}{2\pi}\int_{-\infty+i\delta}^{\infty+i\delta}-i\left[\frac{E}{K_+(k,s)}\right]\coth ke^{-ikx}dk\right]e^{st}ds, \tag{5.56}$$

and the derivative of $\phi_1(x,1,t)$ with respect to t, namely

$$\frac{\partial\phi_1}{\partial t}(x,1,t) = \frac{1}{2\pi i}\int_{\gamma-i\infty}^{\gamma+i\infty} s\left[\frac{1}{2\pi}\int_{-\infty+i\delta}^{\infty+i\delta}\left[\frac{E}{K_+(k,s)}\right]\frac{\coth k}{k}e^{-ikx}dk\right]e^{st}ds. \quad (5.57)$$

We can choose a path of integration in equation (5.55) to lie in the strip $0 < \mathrm{Im}(k) < \tau_+$ as required ([5]). Then, substituting equation (5.56) and (5.57) into equation (5.26) provides the integral representation for the free surface $\eta(x,t)$ in term of the inverse Fourier and Laplace transforms as

$$\eta(x,t) = \frac{P}{1-F^2}\left[1 - F^2 + \frac{1}{2\pi i}\int_{\gamma-i\infty}^{\gamma+i\infty} I(x,s)e^{st}ds\right], \quad (5.58)$$

where

$$I(x,s) = \frac{EF^2}{2\pi}\int_{-\infty+i\delta}^{\infty+i\delta}\frac{ik-s}{K_+(k,s)k\tanh k}e^{-ikx}dk. \quad (5.59)$$

Due to complicated nature of the function $G_1(k,s)$, it is impossible to calculate the inverse transforms in equation (5.58) analytically. But this can be done numerically by means of the approximated method for the inverse Laplace transform proposed by Trefethen *et al.*[57]. In the next section we will calculate the integral by that method.

5.2.4 Numerical Approximation of the Contour Integral

In 2006, Trefethen *et al.* developed an algorithm to approximate contour integrals of the form

$$\mathcal{F} = \frac{1}{2\pi i}\int_{\Gamma} f(z)e^{z}dz, \quad (5.60)$$

where $f(z)$ is analytic for $z \notin (-\infty \quad 0]$, and Γ denotes a Hankel contour that lies in the region of analyticity of $f(z)$. Suppose the integral (5.60) is approximate by a quadrature method

$$\mathcal{F} = \frac{1}{2\pi i}\int_{\Gamma} f(z)e^{z}dz \approx \sum_{k=1}^{N} C_k e^{z_k} f(z_k), \quad (5.61)$$

The sum in equation (5.61) can be interpreted according to residue calculus as

$$\mathcal{F} = \frac{1}{2\pi i}\int_{c} r(z)f(z)dz, \quad (5.62)$$

under the assumption $\mid f(z) \mid \to 0$ as $\mid z \mid \to \infty$, where c is a closed contour in the region of analyticity of $f(z)$ that winds clockwise around each point of z_k and $r(z)$ is the rational function

$$r(z) = \sum_{k=1}^{N} \frac{C_k e^{z_k}}{z - z_k}.$$

Now, by letting Γ' be a contour for the integral in equation (5.60) like Γ, except lying between $\mathbb{R}^-$ and the point z_k, then Γ' is equivalent to Γ for the integral (5.60) of $e^z f(z)$. Then, if we define Γ to be the union of Γ' with a large circular arc of radius $R \to \infty$, then the integral on such closed contour Γ' is equivalent to the integral on the contour c in the integral (5.62) involving $r(z)f(z)$,(see Trefethen *et al.*[57], 2006, and figure 5.4). Therefore, equation (5.62) can be replaced by

$$F_N = \frac{1}{2\pi i} \int_{\Gamma'} r(z) f(z) dz. \tag{5.63}$$

To obtain the higher accuracy result, many values N are needed, in general. However Trefethen *et al.* [57] have shown that much smaller values of N can be used by exploiting the best rational approximation. According to these authors, if one suppose that the poles and residues of $r(z)$ are $z_1, ..., z_N$ and $C_1, ..., C_N$, respectively, then the integral in (5.62) is equal to the sum in equation (5.61). This is a rational function deviation from e^z which decreases at the optimal rate as $(9.28903)^{-N}$ when $N \to \infty$. The Matlab code was provided by Trefethen *et al.*[57] for computing the best approximation of the function e^z. This yields that the integral in equation (5.62) can be approximated by the following sum:

$$\frac{1}{2\pi i} \int_{\Gamma} r(z) e^z dz \approx \sum_{j=1}^{N} C_j f(z_j), \tag{5.64}$$

where z_j and C_j are the poles and residues, respectively, shown in Table 5.1. These quantities were used in calculating the free surface shown in equation (5.58).

Following Trefethen *et al.* [57], we let $s = z/t$; this allows us to express equation (5.58) as

$$\eta(x,t) = \frac{P}{1 - F^2} \left[1 - F^2 + \frac{1}{2\pi i} \int\limits_{\gamma - i\infty}^{\gamma + i\infty} I(x, z/t) e^z dz \right], \tag{5.65}$$

where

$$I(x, z/t) = \frac{1}{2\pi t} \int_{-\infty + i\delta}^{\infty + i\delta} \left[\frac{EF^2(ik - z/t)}{K_+(k, z/t)} \right] \frac{1}{k \tanh k} e^{-ikx} dk. \tag{5.66}$$

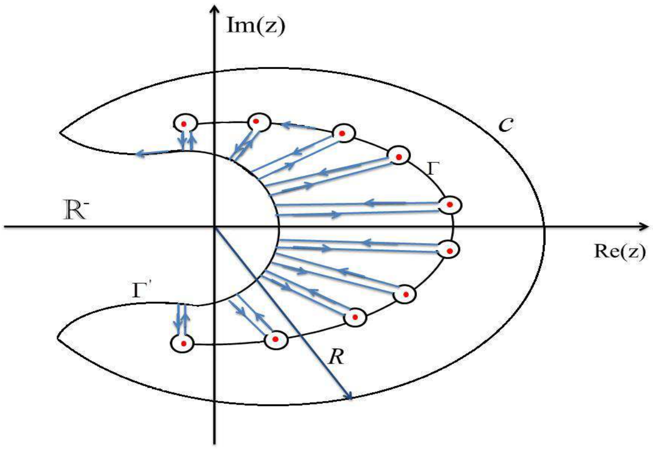

FIGURE 5.4: The contour of integration consisting of the path Γ' and path c of infinitely large radius R. Red dots show the positions of poles in equation (5.61).

Applying the rational approximation given by equation (5.64) allows us to approximate equation (5.65) as

$$\eta(x,t) = \frac{P}{1-F^2}\left[1 - F^2 - \frac{1}{2\pi i t}\sum_{j=1}^{N} C_j I(x, z_j/t)\right], \tag{5.67}$$

From the numerical investigation performed here, we found that $N = 10$ provides quite good approximation of the inverse Laplace transform of the function $I(x, z/t)$.

In equation (5.66), we require $K_+(k, z/t)$, which depends upon the roots of f_1 for different values of z as shown in Section 5.2.5, so for each value of z we have different $K_+(k, z/t)$, and thus a different $I(x, z/t)$, as shown in Appendix C. From Section 5.2.5 equation (5.84) we found that $K_+(k, z/t)$ can be expressed in the generalised form

$$K_+(k, z/t) = \frac{z^2}{t^2}F^2 e^{2itk/z}\Gamma\left(1 - \frac{ik}{\pi}\right)\prod_{j=1}^{\infty}\left(1 - \frac{k}{\zeta_j}\right)e^{k/\zeta_j}, \tag{5.68}$$

where ζ_j are the zeros of the function $K_+(k, z/t)$. Using properties of the gamma-function (see, e.g., Sec. 6.1.31 in ref.[67]),

$$\Gamma\left(1 - \frac{ik}{\pi}\right)\Gamma\left(1 + \frac{ik}{\pi}\right) = \frac{k}{\sinh k}, \tag{5.69}$$

j	z_j	C_j
1	$4.0277 + 1.1939i$	$-4.8184 - 21.0546i$
2	$4.0277 - 1.1939i$	$-4.8184 + 21.0546i$
3	$3.2838 + 3.5944i$	$7.1172 + 8.8195i$
4	$3.2838 - 3.5944i$	$7.1172 - 8.8195i$
5	$1.7154 + 6.0389i$	$-2.5656 - 1.2164i$
6	$1.7154 - 6.0389i$	$-2.5656 + 1.2164i$
7	$-0.8944 + 8.5828i$	$0.2726 + 0.0142i$
8	$-0.8944 - 8.5828i$	$0.2726 - 0.0142i$
9	$-5.1612 + 11.3752i$	$0.0058 + 0.0007i$
10	$-5.1612 - 11.3752i$	$-0.0058 - 0.0007i$

TABLE 5.1: The first ten values of poles z_j and residues C_j provided by Trefethen *et al.*[57] through the Matlab program.

we can replace the gamma-function $\Gamma\left(1 - ik/\pi\right)$ in equation (5.68) with the function $k/\sinh k\Gamma\left(1 + ik/\pi\right)$. Taking into account this property, and substituting (5.68) into (5.66), $I(x, z/t)$ becomes

$$I(x,z/t) = \frac{E}{2\pi i}\int_{-\infty+i\delta}^{\infty+i\delta} \frac{(ik-\frac{z}{t})\Gamma\left(1+\frac{ik}{\pi}\right)\cosh(k)e^{-ikx}}{k^2\frac{z^2}{t^2}e^{\frac{2itk}{z}}\prod_{j=1}^{\infty}\left(1-\frac{k}{\zeta_j}\right)e^{\frac{k}{\zeta_j}}}dk.$$

This integral can be evaluated by closing the contour in the lower half-plane, to have zeros at $k = 0$ and $k = \zeta_j, j = 1, 2, ...$, using the residue theorem, we obtain

$$\begin{aligned} I(x,z/t) &= -E\Bigg(\mathrm{Res}_{k=0}\frac{d}{dk}\left[\frac{(ik-z/t)\Gamma\left(1+\frac{ik}{\pi}\right)\cosh(k)e^{-ikx}}{\frac{z^2}{t^2}e^{2itk/z}\prod_{j=1}^{\infty}\left(1-\frac{k}{\zeta_j}\right)e^{k/\zeta_j}}\right] \\ &+ \mathrm{Res}_{k=\zeta_j}\left[\frac{(ik-z/t)\Gamma\left(1+\frac{ik}{\pi}\right)\cosh(k)e^{-ikx}}{k^2\frac{z^2}{t^2}e^{2itk/z}\prod_{j=1}^{\infty}\left(1-\frac{k}{\zeta_j}\right)e^{k/\zeta_j}}\right]\Bigg), \end{aligned}$$

which may also be written as

$$I(x,z/t) = -E\left(\frac{3+0.183755\frac{z}{t}}{\frac{z^2}{t^2}F^2}i - \prod_{j=1}^{\infty}\left[\frac{(i\zeta_j - z/t)\Gamma\left(1+\frac{i\zeta_j}{\pi}\right)\cosh(\zeta_j)e^{-i\zeta jx}}{\zeta_j\frac{z_j^2}{t^2}e^{1+2it\zeta j/z}}\right]\right) \tag{5.70}$$

Substituting into function $I(x, z/t)$ ten values of z_j instead of z, we obtain from equation (5.67) the approximate value for $\eta(x, t)$ is given by

$$\begin{aligned} \eta(x,t) &= \frac{P}{1-F^2}\Bigg[1-F^2+\frac{E}{2\pi it}\sum_{\jmath=1}^{10}C_\jmath\Bigg[\Bigg(\frac{3+0.183755\frac{z_\jmath}{t}}{\frac{z_\jmath^2}{t^2}F^2}i- \\ &\prod_{j=1}^{\infty}\Bigg(\frac{(i\zeta_j - z_\jmath/t)\Gamma\left(1+\frac{i\zeta_j}{\pi}\right)\cosh(\zeta_j)e^{-i\zeta jx}}{\zeta_j\frac{z_\jmath^2}{t^2}e^{1+2it\zeta j/z_\jmath}}\Bigg)\Bigg)\Bigg]\Bigg]. \end{aligned} \tag{5.71}$$

The value of E in equation (5.71) can be found by applying the condition that $\eta(x = 0, t) = 1$, for a given F and t.

5.2.5 Factorisation of $G_1(k, s)$

The details of the factorisation $G_1(k, s)$ are handled in the same way as that presented in Chapter 2. Let $G_1(k, s) = f_1(k, s)f_2(k, s)/k^2$, where the functions

$f_1(k,s)$ and $f_2(k,s)$ are given by

$$f_1(k,s) = k\sinh(k) + F^2(s-ik)^2\cosh(k) \quad \text{and} \quad f_2(k,s) = \frac{k}{\sinh(k)}. \tag{5.72}$$

The splitting of the Wiener–Hopf equation depends on the roots of functions $f_1(k,s)$ and $f_2(k,s)$. Assuming $s=0$, we obtain the same functions for the steady problem that was presented in Chapter 2. In this case, when $s=0$, $G_1(k,0)$ is given by

$$G_1(k,0) = 1 - F^2 k\coth(k) = f_1(k,0)f_2(k,0), \tag{5.73}$$

where

$$f_1(k,0) = \frac{\sinh(k)}{k} - F^2\cosh(k), \tag{5.74}$$

and

$$f_2(k,0) = \frac{k}{\sinh(k)}. \tag{5.75}$$

As the function, f_1, has two real poles at $k=\pm\mu_R$ and infinitely many imaginary poles at $k=\pm i\pi\mu_n, n=1,2,...$, by using the Weierstrass infinite product theorem [29], f_1 can be factorised as

$$\begin{aligned} f_1(k,0) &= (1-F^2)\left(1-\frac{k^2}{\mu_R^2}\right)\prod_{n=1}^{\infty}\left(1+\frac{k^2}{\pi^2\mu_n^2}\right), \\ &= \left(1-\frac{k^2}{\mu_R^2}\right)H_+(k)H_-(k), \end{aligned} \tag{5.76}$$

such that

$$H_+(k) = \frac{\alpha T(k)}{\Gamma(\frac{3}{2}+\frac{ik}{\pi})} \quad \text{and} \quad H_-(k) = \frac{\alpha T(-k)}{\Gamma(\frac{3}{2}-\frac{ik}{\pi})}. \tag{5.77}$$

We may also determine that

$$f_2(k,0) = \Gamma\left(1+\frac{ik}{\pi}\right)\Gamma\left(1-\frac{ik}{\pi}\right). \tag{5.78}$$

Finally $G_1(k,0)$, by substituting equations (5.76) and (5.78) into equation (5.73) , is given by

$$G_1(k,0) = \left(1-\frac{k^2}{\mu_R^2}\right)\frac{\alpha^2 T(k)T(-k)\Gamma(1-\frac{ik}{\pi})\Gamma(1+\frac{ik}{\pi})}{\Gamma\left(\frac{3}{2}+\frac{ik}{\pi}\right)\Gamma\left(\frac{3}{2}-\frac{ik}{\pi}\right)} = K_-(k,0)K_+(k,0), \tag{5.79}$$

where

$$K_+(k,0) = \left(1 - \frac{k^2}{\mu_R^2}\right)\frac{\alpha^2 T(k)\Gamma(1+\frac{ik}{\pi})}{\Gamma(\frac{3}{2}+\frac{ik}{\pi})}, \tag{5.80}$$

and

$$K_-(k,0) = \frac{T(-k)\Gamma(1-\frac{ik}{\pi})}{\Gamma(\frac{3}{2}-\frac{ik}{\pi})}, \tag{5.81}$$

are analytic and non-zero in the upper and lower halves of the k-plane, respectively. This result has been checked numerically to ensure the function $G_1(k,0)$ in equation (5.73) and its factorisation in equation (5.79) are in agreement as shown in figure (5.5).

For the unsteady problem we put $s = z/t$, where values of z have been found by Trefethen [57] for the inverse Laplace transform. Equation (5.72) with $s = z/t$ becomes

$$f_1(k,z/t) = k\sinh(k) + F^2(z/t - ik)^2\cosh(k). \tag{5.82}$$

The roots of this equation with complex function $f_1(k,z/t)$ of the complex variable k depend on two parameters F and z/t. We investigate further positions of roots in the complex plane k for ten complex values of z_j from Table 5.1. Thus, complex function f_1 actually contains two real parameters F and t. To find roots of $f_1(k,z_j/t)$, one can plot zero isolines for functions $\mathrm{Re}f_1(k,z/t)$ and $\mathrm{Im}f_1(k,z/t)$ and find their intersections as shown in figure 5.6.

For each value of z_j function $f_1(k,z_j/t)$ has the infinite number of complex roots in the upper half-plane denoted by $\tilde{\zeta}_l$ and infinite number of complex roots in the lower half-plane denoted by ζ_j. One can show that asymptotically at large values of indices l and j, the roots are $k_l \approx i(\pi/2 + l\pi)$ and $k_j \approx -i(\pi/2 + j\pi)$. Using the Weierstrass infinite product theorem [29], f_1 can be factorised as

$$f_1(k,z/t) = (z/t)^2F^2e^{2ikt/z}\prod_{l=1}^{\infty}\left(1-\frac{k}{\tilde{\zeta}_l}\right)e^{k/\tilde{\zeta}_l}\prod_{j=1}^{\infty}\left(1-\frac{k}{\zeta_j}\right)e^{k/\zeta_j},$$

and

$$f_2(k,z/t) = \frac{k}{\sinh(k)} = \Gamma\left(1+\frac{ik}{\pi}\right)\Gamma\left(1-\frac{ik}{\pi}\right). \tag{5.83}$$

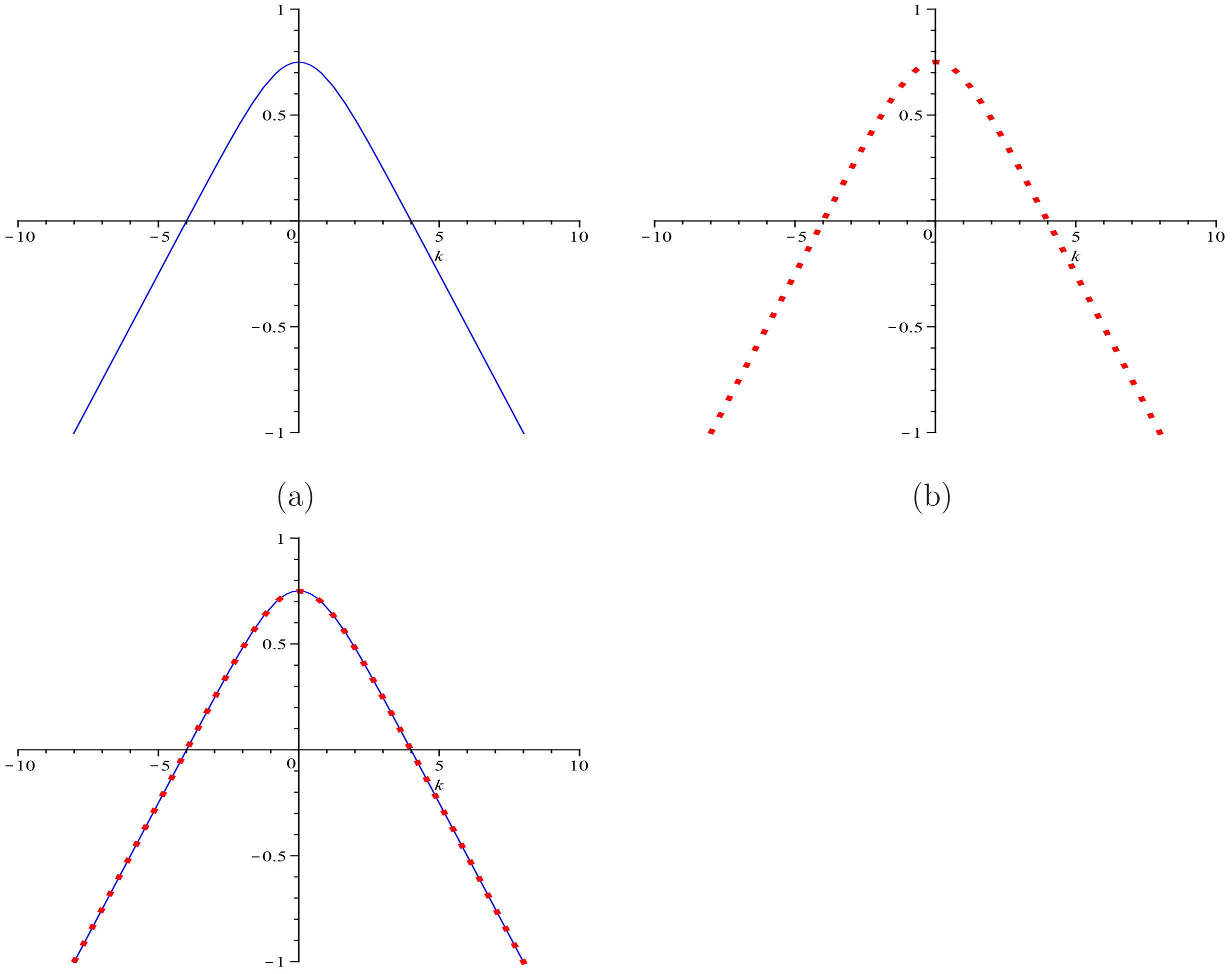

(a)

(b)

(c)

FIGURE 5.5: Figure (a) shows plot of the function $G_1(k)$ in equation (5.73) at $F = 0.5$. Figure (b) shows plot of the function $G_1(k)$ in equation (5.79) at $F = 0.5$. Figure (c) shows plot of the function $G_1(k)$ in equation (5.73) and (5.79).

Thus, function $G_1(k, z/t)$ can be presented in the following forms

$$\begin{aligned} G_1(k, z/t) &= \frac{1}{k^2} f_1(k, z/t) f_2(k, z/t) \\ &= \frac{1}{k^2}\Gamma\left(1-\frac{ik}{\pi}\right)\Gamma\left(1+\frac{ik}{\pi}\right)\frac{z^2}{t^2}F^2 e^{2itk/z}\prod_{l=1}^{\infty}\left(1-\frac{k}{\tilde{\zeta}_l}\right)e^{k/\tilde{\zeta}_l} \\ &\quad \prod_{j=1}^{\infty}\left(1-\frac{k}{\zeta_j}\right)e^{k/\zeta_j}, \\ &= \frac{1}{k^2}K_-(k, z/t)K_+(k, z/t), \end{aligned}$$

we have

$$K_+(k, z/t) = \frac{z^2}{t^2}F^2 e^{2itk/z}\Gamma\left(1-\frac{ik}{\pi}\right)\prod_{j=1}^{\infty}\left(1-\frac{k}{\zeta_j}\right)e^{k/\zeta_j}, \tag{5.84}$$

and

$$K_-(k, z/t) = \Gamma\left(1+\frac{ik}{\pi}\right)\prod_{l=1}^{\infty}\left(1-\frac{k}{\tilde{\zeta}_l}\right)e^{k/\tilde{\zeta}_l}, \tag{5.85}$$

where $K_+(k, z/t)$ is analytic in the upper-half plane and $K_-(k, k, z/t)$ is analytic in the lower-half plane.

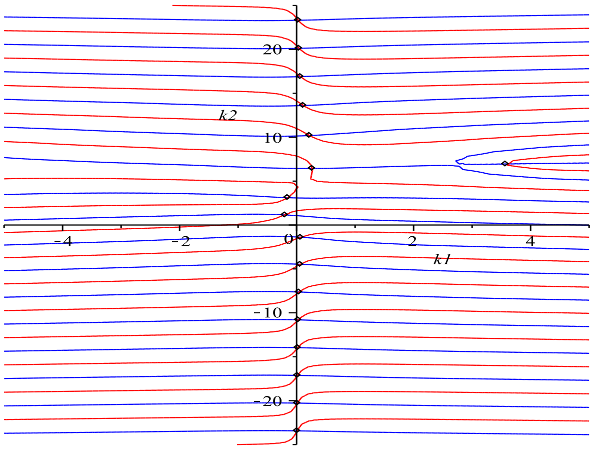

FIGURE 5.6: Zero isolines of functions $\mathrm{Re} f_1(k, z/t)$ (red lines) and $\mathrm{Im} f_1(k, z/t)$ (blue lines). Dots indicate intersection points of isolines. The plot was generated for $F = 0.5$, $t = 1$ and $z_1 = 4.0277 + 1.1939i$.

For each value of z_j we will go through the process of finding the roots of the function $f_1(k, z_j/t)$ and derivation of function $K_+(k, z_j/t)$ for the subsequent derivation of the function $I(x,z)$ in equation (5.66) is illustrated below for the fixed value of z_j. Let us fix the time t and use the first value of z_j from Table 5.1, $z_1 = 4.0277 + 1.1939i$, then we find that $f_1(k, z_1/t)$ has infinitely many complex roots in the upper half-plane are given by $\tilde{\zeta}_l, l = 1, 2, 3, ...$, and in the lower half-plane, $\zeta_j, j = 1, 2, 3, ...$ as shown in figure 5.6.

Then $f_1(k, z_1/t)$ can be factorised by the following way

$$f_1(k, z_1/t) = z_1^2 F^2 e^{2ik/z_1} \prod_{l=1}^{\infty}\left(1-\frac{k}{\tilde{\zeta}_l}\right)e^{k/\tilde{\zeta}_l} \prod_{j=1}^{\infty}\left(1-\frac{k}{\zeta_j}\right)e^{k/\zeta_j},$$

and

$$f_2(k, z_1/t) = \frac{k}{\sinh(k)} = \Gamma\left(1+\frac{ik}{\pi}\right)\Gamma\left(1-\frac{ik}{\pi}\right). \tag{5.86}$$

Then from equation (5.45) and by using the factorisation of f_1 and f_2 above, we find

$$\begin{aligned} G_1(k, z_1/t) &= \frac{1}{k^2} f_1(k, z_1/t) f_2(k, z_1/t) \\ &= \frac{1}{k^2}\Gamma\left(1-\frac{ik}{\pi}\right)\Gamma\left(1+\frac{ik}{\pi}\right)\frac{z_1^2}{t^2}F^2 e^{2itk/z_1}\prod_{l=1}^{\infty}\left(1-\frac{k}{\tilde{\zeta}_l}\right)e^{k/\tilde{\zeta}_l}\prod_{j=1}^{\infty}\left(1-\frac{k}{\zeta_j}\right)e^{k/\zeta_j}, \\ &= \frac{1}{k^2} K_-(k, z_1/t) K_+(k, z_1/t), \end{aligned}$$

where

$$K_+(k, z_1/t) = \frac{z_1^2}{t^2}F^2 e^{2itk/z_1}\Gamma\left(1-\frac{ik}{\pi}\right)\prod_{j=1}^{\infty}\left(1-\frac{k}{\zeta_j}\right)e^{k/\zeta_j}, \tag{5.87}$$

and

$$K_-(k, z_1/t) = \Gamma\left(1+\frac{ik}{\pi}\right)\prod_{l=1}^{\infty}\left(1-\frac{k}{\tilde{\zeta}_l}\right)e^{k/\tilde{\zeta}_l}. \tag{5.88}$$

Now derived function $K_+(k, z_1/t)$ can be substituted into equation (5.66) for the inverse Fourier transform providing function $I(x, z_1/t)$ which will be express as

$$\begin{aligned}
I_1(x, z_1/t) &= \frac{1}{2\pi i}\int_{-\infty+i\delta}^{\infty+i\delta} \frac{EF^2(ik - z_1/t)}{K_+(k, z_1/t)k\tanh(k)} e^{-ikx}dk \\
&= \frac{1}{2\pi i}\int_{-\infty+i\delta}^{\infty+i\delta} \frac{EF^2(ik - z_1/t)e^{-ikx}}{k\tanh(k)\Gamma\left(1 - \frac{ik}{\pi}\right)\frac{z_1^2}{t^2}F^2 e^{2itk/z_1}\prod_{j=1}^{\infty}\left(1 - \frac{k}{\zeta_j}\right)e^{k/\zeta_j}}dk \\
&= \frac{E}{2\pi i}\int_{-\infty+i\delta}^{\infty+i\delta} \frac{(ik - z_1/t)\Gamma\left(1 + \frac{ik}{\pi}\right)\cosh(k)e^{-ikx}}{k\sinh(k)\Gamma\left(1 - \frac{ik}{\pi}\right)\Gamma\left(1 + \frac{ik}{\pi}\right)\frac{z_1^2}{t^2}e^{2itk/z_1}\prod_{j=1}^{\infty}\left(1 - \frac{k}{\zeta_j}\right)e^{k/\zeta_j}}dk \\
&= \frac{E}{2\pi i}\int_{-\infty+i\delta}^{\infty+i\delta} \frac{(ik - z_1/t)\Gamma\left(1 + \frac{ik}{\pi}\right)\cosh(k)e^{-ikx}}{k^2\frac{z_1^2}{t^2}e^{2itk/z_1}\prod_{j=1}^{\infty}\left(1 - \frac{k}{\zeta_j}\right)e^{k/\zeta_j}}dk,
\end{aligned}$$

which may be evaluated by closing the contour in the lower half-plane, to have zeros at $k = 0$ and $k = \zeta_j, j = 1, 2, ...$ Using residue theorem, we find

$$\begin{aligned}
I_1(x, z_1/t) \quad &= \quad -E\left(\mathrm{Res}_{k=0}\frac{d}{dk}\left[\frac{(ik - z_1/t)\Gamma\left(1 + \frac{ik}{\pi}\right)\cosh(k)e^{-ikx}}{\frac{z_1^2}{t^2}e^{2itk/z_1}\prod_{j=1}^{\infty}\left(1 - \frac{k}{\zeta_j}\right)e^{k/\zeta_j}}\right]\right. \\
&+ \quad \left.\mathrm{Res}_{k=\zeta_j}\left[\frac{(ik - z_1/t)\Gamma\left(1 + \frac{ik}{\pi}\right)\cosh(k)e^{-ikx}}{k^2\frac{z_1^2}{t^2}e^{2itk/z_1}}\prod_{j=1}^{\infty}\left(1 - \frac{k}{\zeta_j}\right)e^{k/\zeta_j}\right]\right),
\end{aligned}$$

which may be written as

$$\begin{aligned}
I_1(x, z_1/t) \quad &= \quad -E\left(\frac{3 + 0.183755\frac{z_1}{t}}{\frac{z_1^2}{t^2}F^2}i\right. \\
&- \quad \left.\prod_{j=1}^{\infty}\left[\frac{(i\zeta_j - z_1/t)\Gamma\left(1 + \frac{i\zeta_j}{\pi}\right)\cosh(\zeta_j)e^{-i\zeta jx}}{\zeta_j\frac{z_1^2}{t^2}e^{1+2it\zeta j/z_1}}\right]\right).
\end{aligned}$$

Now, from equation (5.67) and using $N = 10$, we find that

$$\eta(x, t) = \frac{P}{1 - F^2}\left[1 - F^2 - \frac{1}{2\pi it}\left(C_1I_1(x, z_1/t) + C_2I_2(x, z_2/t) + ... + C_{10}I_{10}(x, z_{10}/t)\right)\right] \quad (5.89)$$

where η is the formula to generate the free surface profile, $C_1, ..., C_{10}$, $z_1, ..., z_{10}$ is a known parameter. $I_1(x, z_1/t)$ is found above and $I_2(x, z_2/t), ..., I_{10}(x, z_{10}/t)$ are evaluated in Appendix C.

The procedure of computing the unsteady free surface profile given by equation (5.89) is summarised in the following algorithm. We choose the Froude number

$F = 0.5$, Pressure $P = 0.01$, time $t = 1, 5, 10, 100, 1000$ and the separation point between the flat plate and the free surface $\eta(x = 0, t) = 1$.

Algorithm 2: Unsteady Free surface flow

INPUT: Froude number F, pressure P, time t and the separation point $\eta(x = 0, t) = 1$.

Step 1: *Compute the poles* z_j *and residues* C_j *using Trefethen Matlab code presented in [57] (see Table (5.1)).*

Step 2: *Approximate the function* $I(x, z/t)$ *using the contour integral approximation given by equation (5.66).*

Step 3: *Evaluate the roots* ζ_j *and* $\tilde{\zeta}_l$ *of the function* $f_1(k, s)$ *given by (5.82) at a fixed time* t, F, P *and ten values of* z_j.

Step 4: *For a given time* t, *Compute the approximation function* $I(x, z_j/t)$ *for ten values of* z_j *given by equation (5.70).*

Step 5: *Using the function* $I(x, z_j/t)$ *computed in step 4, calculate the constant* E *(given in equation (5.70)), for a given time* t, P *and* F, *where* $\eta(x, 0) = 1$

Step 6: *For ten values of* z_j, *and a given time* t, *compute the elevation of the free surface* $\eta(x, t)$ *given by equation (5.89).*

5.3 Results and Discussions

The problem of transient two-dimensional free surface flow past a semi-infinite flat plate in a fluid of finite depth is solved analytically using the Laplace transform and the Wiener–Hopf technique for the subcritical case, $F < 1$.

The free surface profile $\eta(x, t)$ is given by equation (5.71) are computed for any instant of time t with appropriate accuracy using, for instance, ten values of poles z_j and residues C_j from Table 5.1 as given by Trefethen *et al.* [57] (the accuracy can be raised if required; then more data should be added into the Table using the Matlab code provided by Trefethen *et al.*[57]). To use this formula for different time moments, function $G(k, z/t)$ should be factorised anew every time and roots of function $f_1(k, z/t)$ should be found as shown in Appendix C.

We studied the dependence of accuracy of calculation of a free surface on the number of poles taken from Table 5.1. It is expected that after the transient process, when $t \to \infty$, the free surface in the near-field zone behind the stern should be stationary. Hence, it shape can be compared with the steady state solution obtained by Ogilat *et al.*[75] for the same parameters. Figure 5.7 illustrates the comparison of free surface shape obtained in this study at $t = 1000$ with the steady-state solution. As one can see, solution obtained with only 8 poles does not match with the steady-state solution, whereas solution obtained with 10 poles does match and is practically indistinguishable from the steady-state solution.

Figure 5.8 illustrates the influence of the number of roots of function $G_+(k, s)$ on the accuracy of solution. In this case $N = 10$ poles were chosen but number of roots were taken 40 and 60. As follows from figure 5.8, 40 roots is not enough to obtain accurate solution. Only the first period of wave can be satisfactorily described with the help of 40 roots. Wave amplitude is reproduced with fairly good accuracy, but not the wave period.

Thus,it was concluded that the optimal number of poles is $N = 10$ and number of roots is 60. In further studies these number were used.

The transition to the steady-state regime is illustrated by figure 5.9. As one can see from that figure, in the near-field zone, the transient solution approaches stationary solution by $t = 1000$. At early times, the maximal splash may be significantly greater than the stationary wave amplitude.

As one can see from figure 5.9, the waves are evolving at relatively short times, and the free surface approaches the horizontal flat level at large x. At large time, the free surface eventually attains the steady state, at least, at the near-field zone close to the flat stern as shown in figure 5.10.

As one can see from figure 5.9, the waves are undeveloped in relatively short times, and the free surface approaches the unperturbed horizontal level at large x. After elapsing some time, generated waves become stationary, at least, at the near-field zone just behind the stern. In the transient period large amplitude splash is generated, as one can see in figure 5.10. The dependence of maximal wave amplitude on time is shown in figure 5.11. As follows from this figure, after the first splash, maximal wave amplitude drops down, increases again and only after that it gradually decreases to the steady-state value. For the considered parameters (see figure caption), maximal amplitude of the splash is 3.4 times greater than the amplitude of stationary wave.

5.4 Conclusion

In this chapter we investigated the transient problem of wave generation past the flat stern which is suddenly submerged at the initial instant of time into the moving water at small depth d which is much less than the total fluid depth h. It is assumed that the Froude number is less than the critical one, $F \equiv V/\sqrt{gh} < 1$. Solution to the linearised problem has been obtained in the analytic form, equation (5.71), and then calculated numerically. The traditional methods to this class of mixed boundary problems were used: Laplace transform on time, Fourier transform on x and Wiener–Hopf technique. It was shown that in the transient period high amplitude splash is generated, then the amplitude of highest wave drops down and quickly increases again. After that the wave amplitude gradually approaches the stationary state which is characterised by a constant amplitude quasi-sinusoidal trailing wave. The time dependence of the free-surface perturbation behind the plate was found numerically and presented graphically.

The problem of the stern shape optimisation to reduce generated waves was not considered in this chapter, whereas for the steady-state problem it has been shown [75] that optimal shapes do exist such that the trailing waves can be almost completely eliminated. We leave this problem for the impeding study.

In the next chapter the steady problem for the two-layer model in a fluid of finite depth will be investigated.

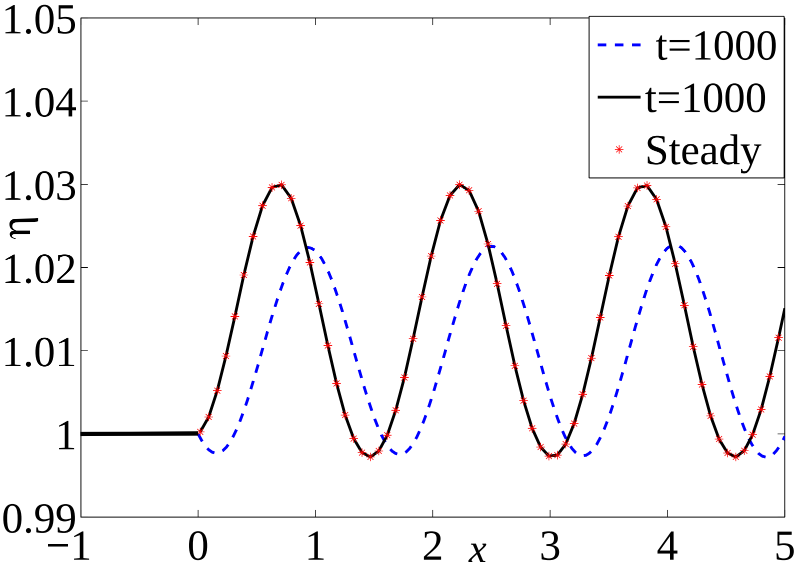

FIGURE 5.7: Free surface profile in dimensionless variables relative to unperturbed level $y = 1$ for $t = 1000$ as obtained from equation (5.71) with different numbers of poles in Table 5.1. Dashed line pertains to $N = 8$, solid line – $N = 10$, and dots show the steady-state solution derived by Ogilat *et al.* [75]. The plot was generated for $P = 0.01$, $F = 0.5$ and with 60 complex roots of function $G_+(k, s)$.

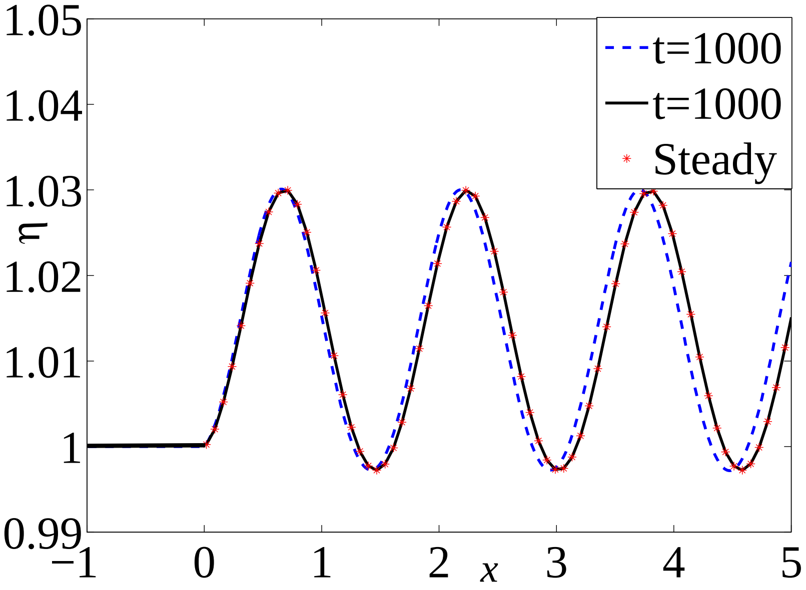

FIGURE 5.8: Free surface profile in dimensionless variables relative to unperturbed level $y = 1$ for $t = 1000$ as obtained from equation (5.71) with fixed number of poles $N = 10$ from Table 5.1, but with different numbers of complex roots of function $G_+(k, s)$. Dashed line pertains to 40 roots, solid line – to 60 roots, and dots show the steady-state solution derived by Ogilat *et al.* [75]. The plot was generated for $P = 0.01$, $F = 0.5$.

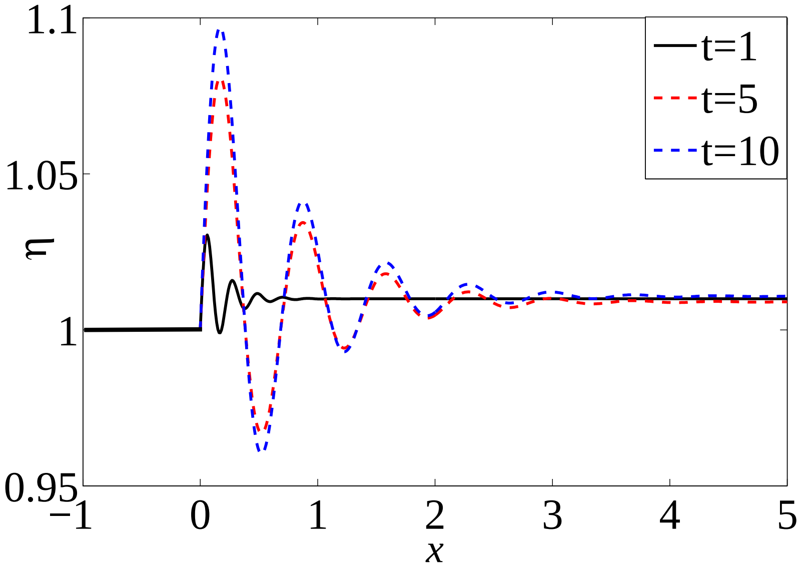

FIGURE 5.9: The free surface profile for $P = 0.01$, $F = 0.5$ and different instants of time as per equation (5.71).

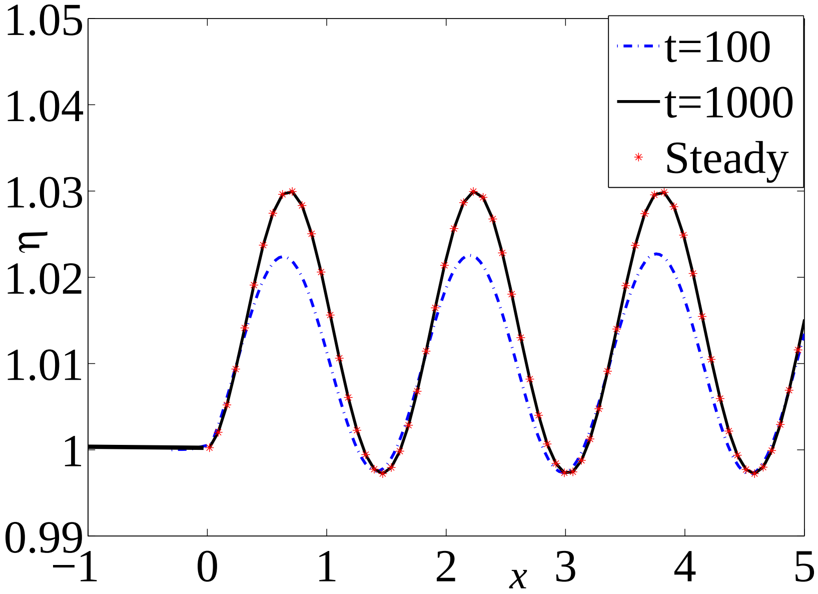

FIGURE 5.10: The free surface profile for $P = 0.01$, $F = 0.5$ and different instants of time as per equation (5.71). The steady state solution derived in Ogilat *et al.* [75] is shown in this figure for the comparison.

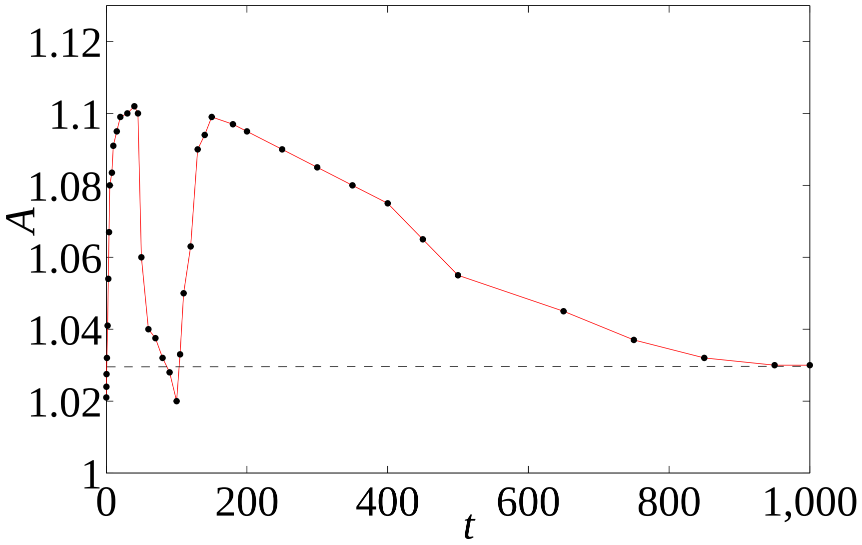

FIGURE 5.11: Maximal wave amplitude $A = \eta_{max}$ against time as per equation (5.71). The plot was generated for $P = 0.01$, $F = 0.5$.

Chapter 6

Stationary Internal Waves Past a 2D Stern in Two-Layer a Fluid

6.1 Introduction

In two-layer fluid may exist internal waves that propagate beneath the free surface on the interface between the layers of different density. Such waves are usually hidden from eyesight, however, sometimes they produce a visible response on the surface (for details see [101, 41]). In this Chapter we study internal wave generation past a two-dimensional (2D) semi-infinite flat plate in a fluid of a finite depth. The linearised problem is solved analytically using a Fourier transform and the Wiener–Hopf technique. Our main interest is in the possibility to minimise trailing waves past the stern or eliminate them at all, as well as to study the influence of the density aspect ratio on the generated waves.

6.2 Mathematical formulation

We consider a 2D flow in two-layer fluids of a finite depth as shown in figure 6.1. As before, the fluid is assumed to be inviscid and incompressible and the flow is irrotational; the density of upper layer is ρ_1 and the density of lower layer is $\rho_2 > \rho_1$, whereas the layers depths are h_1 and h_2, respectively. The velocity potential in the upper and lower layers are, respectively, Φ_1 and Φ_2.

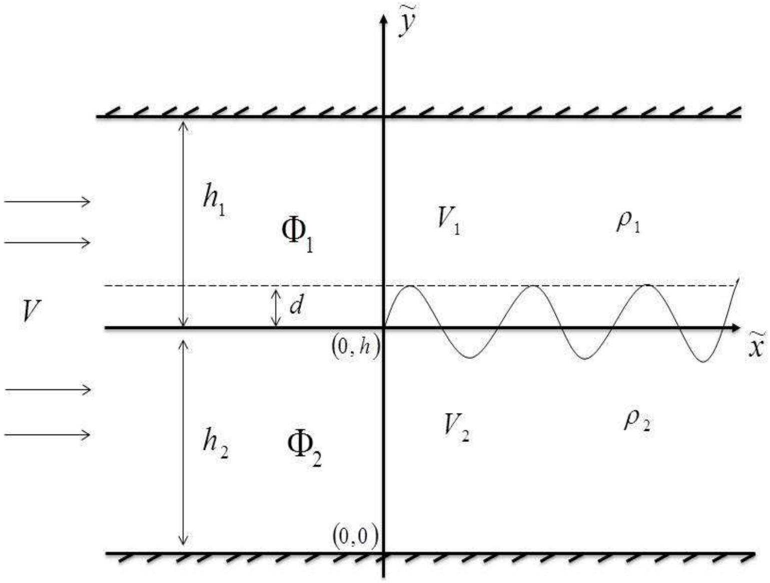

FIGURE 6.1: A sketch of the two-layer model with internal waves at the interface.

As the flow is irrotational, the $\tilde{x}$ and $\tilde{y}$ components of the velocity field can be presented as

$$\tilde{u_i} = \frac{\partial \Phi_i}{\partial \tilde{x}}, \quad \tilde{w_i} = \frac{\partial \Phi_i}{\partial \tilde{y}}, \quad i = 1, 2, \tag{6.1}$$

where $\tilde{u_i}$ is the horizontal velocity and $\tilde{w_i}$ is the vertical velocity of the fluid.

The fluid far upstream is uniform with the speed V and the speed far downstream in the upper and lower layers are the same. The downstream speeds in both layer should be the same as the tangential discontinuity of the velocity will appear. This leads to hydrodynamic instability, which is far from our interest here.

The Cartesian coordinates are introduced such as shown in Fig. 6.1. It is assumed that there is a thin flat plate at $\tilde{x} < 0$, which is submerged onto depth d below the interface between the layers.

Since we assumed that the fluid is incompressible, the governing equations are

$$\nabla^2 \Phi_1 = 0, \qquad \nabla^2 \Phi_2 = 0, \tag{6.2}$$

in the upper and lower layers, correspondingly. To eliminate the influence of surface waves and simplify the mathematical formulation of the problem, we will use further the "rigid lid approximation" traditionally used in the study of internal waves. Two boundary conditions can be used then for the vertical velocity components in each layer:

$$\frac{\partial \Phi_1}{\partial \tilde{y}}|_{\tilde{y}=H} = 0, \quad \frac{\partial \Phi_2}{\partial \tilde{y}}|_{\tilde{y}=0} = 0, \quad -\infty < \tilde{x} < \infty, \tag{6.3}$$

where $H = h_1 + h_2$. Other two boundary conditions are used at the rigid plate, at $\tilde{x} < 0$:

$$\frac{\partial \Phi_1}{\partial \tilde{y}} = 0, \quad \frac{\partial \Phi_2}{\partial \tilde{y}} = 0, \quad \tilde{y} = h_2, \quad \tilde{x} < 0. \tag{6.4}$$

At the interface between two layers, $\tilde{y} = h_2 + \tilde{\eta}(\tilde{x})$, $\tilde{x} > 0$, two kinematic boundary conditions are used (fluid particles on both sides of the interface move vertically together with the interface):

$$\frac{\partial \Phi_1}{\partial \tilde{x}} \frac{\partial \tilde{\eta}}{\partial \tilde{x}} = \frac{\partial \Phi_1}{\partial \tilde{y}}, \qquad \frac{\partial \Phi_2}{\partial \tilde{x}} \frac{\partial \tilde{\eta}}{\partial \tilde{x}} = \frac{\partial \Phi_2}{\partial \tilde{y}}. \tag{6.5}$$

One more dynamical boundary condition can be expressed in terms of the

Bernoulli equations:

$$\frac{1}{2}\left[\left(\frac{\partial\Phi_1}{\partial\tilde{x}}\right)^2+\left(\frac{\partial\Phi_1}{\partial\tilde{y}}\right)^2\right]+g\tilde{y} = \frac{1}{2}V^2+gh_2+\frac{\tilde{p}_1}{\rho_1}, \quad \text{at } \tilde{y}=(h_2+\tilde{\eta})^+, \tag{6.6}$$

$$\frac{1}{2}\left[\left(\frac{\partial\Phi_2}{\partial\tilde{x}}\right)^2+\left(\frac{\partial\Phi_2}{\partial\tilde{y}}\right)^2\right]+g\tilde{y} = \frac{1}{2}V^2+gh_2+\frac{\tilde{p}_2}{\rho_2}, \quad \text{at } \tilde{y}=(h_2+\tilde{\eta})^-. \tag{6.7}$$

where symbols ‘plus’ and ‘minus’ stand for that the corresponding quantities should be taken either just above the interface or just below the interface.

As follows from these equations, the pressure difference at the interface is:

$$\Delta p \equiv \tilde{p}_1-\tilde{p}_2=\rho_1\left\{\frac{1}{2}\left[\left(\frac{\partial\Phi_1}{\partial\tilde{x}}\right)^2+\left(\frac{\partial\Phi_1}{\partial\tilde{y}}\right)^2\right]+g\tilde{y}-\frac{1}{2}V^2-gh_2\right\}-$$

$$\rho_2\left\{\frac{1}{2}\left[\left(\frac{\partial\Phi_2}{\partial\tilde{x}}\right)^2+\left(\frac{\partial\Phi_2}{\partial\tilde{y}}\right)^2\right]+g\tilde{y}-\frac{1}{2}V^2-gh_2\right\}. \tag{6.8}$$

At the interface between two fluids, $x>0$, the pressure difference is zero as the pressure is continuous across the interface, whereas the pressure difference across the plate, $x<0$, is not zero, in general, and may be a function of x. This function can be determined from the solution of the problem.

It is convenient to formulate the problem in dimensionless variables to minimise the number of free parameters. To this end we scale all lengths and velocities with respect to the depth of the lower layer h_2 and speed V respectively. Thus, we introduce the dimensionless variables as follows:

$$x=\tilde{x}/h_2, \quad y=\tilde{y}/h_2, \quad \tilde{\phi}_1=\Phi_1/Vh_2, \quad \tilde{\phi}_2=\Phi_2/Vh_2,$$

$$p_1=\tilde{p}_1/gh_2, \quad p_2=\tilde{p}_2/gh_2, \quad \eta=\tilde{\eta}/h_2, \quad b=h_1/h_2.$$

Then, the Laplace equations in each layers and boundary conditions (6.2)–(6.7) become

$$\nabla^2\tilde{\phi}_1=0; \quad \nabla^2\tilde{\phi}_2=0, \quad 0<y<\infty, \quad -\infty<x<\infty, \tag{6.9}$$

$$\frac{\partial\tilde{\phi}_1}{\partial y}\Big|_{y=1+b}=0, \quad \frac{\partial\tilde{\phi}_2}{\partial y}\Big|_{y=0}=0, \quad -\infty<x<\infty. \tag{6.10}$$

At $y = 1, \quad x < 0$:

$$\frac{\partial \tilde{\phi}_1}{\partial y} = 0, \quad \frac{\partial \tilde{\phi}_2}{\partial y} = 0. \tag{6.11}$$

At $y = 1 + \eta(x) \quad x > 0$:

$$\frac{\partial \tilde{\phi}_1}{\partial x}\frac{\partial \eta}{\partial x} = \frac{\partial \tilde{\phi}_1}{\partial y}, \quad \frac{\partial \tilde{\phi}_2}{\partial x}\frac{\partial \eta}{\partial x} = \frac{\partial \tilde{\phi}_2}{\partial y}, \tag{6.12}$$

$$a\left\{\frac{F^2}{2}\left[\left(\frac{\partial \tilde{\phi}_1}{\partial \tilde{x}}\right)^2 + \left(\frac{\partial \tilde{\phi}_1}{\partial \tilde{y}}\right)^2 - 1\right] + y - 1\right\} -$$

$$\frac{F^2}{2}\left[\left(\frac{\partial \tilde{\phi}_2}{\partial \tilde{x}}\right)^2 + \left(\frac{\partial \tilde{\phi}_2}{\partial \tilde{y}}\right)^2 - 1\right] - y + 1 = n_1(x), \tag{6.13}$$

where $a = \rho_1/\rho_2$, $F = V/\sqrt{gh_2}$ and $n_1(x) = \Delta p/\rho_2$, and $n_1(x) \equiv 0$ at $x > 0$.

6.2.1 Linearised two-layer model

Further we will consider the linearised problem assuming that all perturbations are small enough (their smallness will be specified later). For the velocity potentials we put

$$\tilde{\phi}_1 = x + \epsilon\phi_1, \quad \tilde{\phi}_2 = x + \epsilon\phi_2, \quad \eta(x) = \epsilon\eta_1(x), \quad n_1(x) = \epsilon n(x), \tag{6.14}$$

where $\epsilon = d/h_2 \sim F^2/(1-a) \ll 1$. Then the main equation and boundary conditions (6.9)–(6.13) become

$$\nabla^2\phi_1 = 0, \quad \nabla^2\phi_2 = 0, \tag{6.15}$$

$$\frac{\partial \phi_1}{\partial y}|_{y=1+b}, \quad \frac{\partial \phi_2}{\partial y}|_{y=0} = 0, \quad -\infty < x < \infty, \tag{6.16}$$

$$\frac{\partial \phi_1}{\partial y} = m(x), \quad \frac{\partial \phi_2}{\partial y} = m(x), \quad y = 1, \quad -\infty < x < \infty, \tag{6.17}$$

where $m(x)$ is the known function describing the shape of the plate for $x < 0$ and unknown function describing the interface between layers for $x > 0$. Since we assume here that the plate is flat, then we have $m(x) \equiv 0$ when $x < 0$, whereas when $x > 0$ we have

$$\frac{\partial \eta_1}{\partial x} = \frac{\partial \phi_1}{\partial y}, \quad \frac{\partial \eta_1}{\partial x} = \frac{\partial \phi_2}{\partial y}, \quad y = 1. \tag{6.18}$$

Linearised equation (6.13) reads

$$\eta_1(x) = \frac{F^2}{1-a}\left(a\frac{\partial \phi_1}{\partial x} - \frac{\partial \phi_2}{\partial x}\right) - \frac{n(x)}{1-a}, \tag{6.19}$$

where $n(x) \equiv 0$ for $x > 0$. Then the location of the interface for $x > 0$ becomes

$$\eta_1(x) = \frac{F^2}{1-a}\left(a\frac{\partial\phi_1}{\partial x} - \frac{\partial\phi_2}{\partial x}\right). \tag{6.20}$$

To solve the derived set of linear differential equations (6.15)–(6.19), we apply the Fourier transform.

6.2.2 Application of Fourier Transforms

The linear set of differential equations (6.15)–(6.19) can be solved by means of the Fourier transform and Wiener–Hopf technique. The Fourier transform of the velocity potentials in each layer are given by

$$\bar{\phi}_1(k,y) = \int\limits_{-\infty}^{\infty} \phi_1(x,y)e^{ikx}dx, \quad \bar{\phi}_2(k,y) = \int\limits_{\infty}^{\infty} \phi_2(x,y)e^{ikx}dx. \tag{6.21}$$

By applying the Fourier transform to equation (6.15) we find

$$\frac{\partial^2\bar{\phi}_1(k,y)}{\partial y^2} - k^2\bar{\phi}_1(k,y) = 0, \tag{6.22}$$

and

$$\frac{\partial^2\bar{\phi}_2(k,y)}{\partial y^2} - k^2\bar{\phi}_2(k,y) = 0. \tag{6.23}$$

The general solutions to these equation subject to boundary conditions (6.16) are

$$\bar{\phi}_1(k,y) = A(k)\left[\cosh ky - \tanh k(1+b)\sinh ky\right], \tag{6.24}$$

$$\bar{\phi}_2(k,y) = C(k)\cosh ky. \tag{6.25}$$

Also, the Fourier transform of the boundary conditions (6.17) and (6.19) gives

$$\frac{\partial\bar{\phi}_1}{\partial y} = \bar{m}(k), \quad \frac{\partial\bar{\phi}_2}{\partial y} = \bar{m}(k), \quad y = 1, \quad -\infty < x < \infty, \tag{6.26}$$

$$\bar{\eta}_1(k) = \frac{ikF^2}{1-a}\left(a\bar{\phi}_1 - \bar{\phi}_2\right) - \frac{\bar{n}(k)}{(1-a)} =$$

$$\frac{ikF^2}{1-a}\left\{aA(k)\left[\cosh k - \tanh k(1+b)\sinh k\right] - C(k)\cosh k\right\} - \frac{\bar{n}(k)}{1-a}. \tag{6.27}$$

From equation (6.18) we have

$$ik\bar{\eta}_1 = \bar{m}(k). \tag{6.28}$$

By substituting equation (6.24) and (6.25) into (6.26), we find that

$$A(k)=\frac{\bar{m}(k)}{k\left[\sinh ky-\tanh k(1+b)\cosh ky\right]},\quad C(k)=\frac{\bar{m}(k)}{k\sinh ky},\tag{6.29}$$

By substituting $A(x)$ and $C(k)$ from (6.29), at $y=1$, into (6.27), we find

$$\bar{\eta}_1(k)=\frac{iF^2\bar{m}(k)}{1-a}\left[a\frac{1-\tanh k(1+b)\tanh k}{\tanh k-\tanh k(1+b)}-\frac{1}{\tanh k}\right]-\frac{\bar{n}(k)}{1-a}.\tag{6.30}$$

Combining now equations (6.28) and (6.30), we derive

$$\left\{\frac{F^2}{1-a}\left[a\frac{1-\tanh k(1+b)\tanh k}{\tanh k-\tanh k(1+b)}-\frac{1}{\tanh k}\right]+\frac{1}{k}\right\}i\bar{m}(k)=\frac{\bar{n}(k)}{1-a},\tag{6.31}$$

or alternatively

$$\bar{m}(k)=-\frac{ik\bar{n}(k)}{G_2(k)},\tag{6.32}$$

where

$$G_2(k)=1-a-F^2k\left[\frac{1}{\tanh k}+a\frac{\tanh k(1+b)\tanh k-1}{\tanh k-\tanh k(1+b)}\right].\tag{6.33}$$

Unfortunately, the expression for $G_2(k)$ in its general form is such that the application of the Wiener–Hopf technique used in the previous Chapters is not possible here. Therefore, we will consider further a particular case of infinitely deep upper layer when $b\to\infty$. In this case equation (6.33) reduces to

$$G_2(k)=1-a-kF^2\left(a+\frac{1}{\tanh k}\right).\tag{6.34}$$

When the density ratio vanishes, i.e. $a\equiv\rho_1/\rho_2=0$, this expression reduces to the case of surface waves studied in Chapter 2:

$$G_2(k)=1-F^2k\coth k.\tag{6.35}$$

6.3 The Wiener–Hopf equation

Thus, we have found the function $m(x)$ can be determined with the help of inverse Fourier transform from equation (6.32), where function $G_2(k)$ is given by equation (6.34).

Anticipating the use of the Wiener–Hopf technique, $\bar{m}(k)$ and $\bar{n}(k)$ can be split into

$$\bar{m}(k)=\bar{m}_-(k)+\bar{m}_+(k),\tag{6.36}$$

$$\bar{n}(k) = \bar{n}_-(k) + \bar{n}_+(k), \tag{6.37}$$

where

$$\bar{m}_-(k) = \int_{-\infty}^{0} m(x)e^{ikx}dx, \quad \text{and} \quad \bar{n}_-(k) = \int_{-\infty}^{0} n(x)e^{ikx}dx, \tag{6.38}$$

are analytic functions in the lower-half plane, and

$$\bar{m}_+(k) = \int_{0}^{\infty} m(x)e^{ikx}dx, \quad \text{and} \quad \bar{n}_+(k) = \int_{0}^{\infty} n(x)e^{ikx}dx, \tag{6.39}$$

are analytic functions in the upper-half plane. Since the plate is flat then $\bar{m}_-(k) = 0$, and the pressure for $x > 0$, giving $\bar{n}_+(k) = 0$. This implies that the Wiener–Hopf equation, (6.32), becomes

$$\bar{m}_+(k) = \frac{-ik\bar{n}_-(k)}{G_2(k)}. \tag{6.40}$$

The method of solving (6.40) depends on the decomposition of $G_2(k)$ in the form

$$G_2(k) = W_+(k)W_-(k), \tag{6.41}$$

where $W_+(k)$ is analytic and non-zero in the upper-half plane, and $W_-(k)$ is analytic and non-zero in the lower-half plane. The Wiener–Hopf equation from (6.40) becomes

$$\bar{m}_+(k)W_+(k) = \frac{-ik\bar{n}_-(k)}{W_-(k)}, \tag{6.42}$$

where the left-hand side is analytic and non-zero in the upper-half plane and the right hand-side is analytic and non-zero in the lower-half plane.

By studying the behavior of the left-hand side of (6.42) as $k \to \infty$ in the upper-half plane and the right-hand side in the lower-half plane, with the use of Liouville's theorem ([18], p. 85) both sides must be equal to some constant E which must be determined. As such, equation (6.42) becomes

$$\bar{m}_+(k)W_+(k) = \frac{-ik\bar{n}_-(k)}{W_-(k)} = E. \tag{6.43}$$

The solution to equation (6.43) for $\bar{m}_+(k)$ is substituted into (6.29), as $b \to \infty$, to yield the equation

$$\bar{m}_+(k) = kA(k)(\sinh ky - \cosh ky) = \frac{E}{W_+(k)}, \tag{6.44}$$

and

$$\bar{m}_+(k) = kC(k)\sinh ky = \frac{E}{W_+(k)}. \tag{6.45}$$

It follows from equations (6.24) and (6.25), as $b \to \infty$, that the transformed functions $\bar{\phi}_1(k, y)$ and $\bar{\phi}_2(k, y)$ are given by

$$\bar{\phi}_1(k, y) = -\frac{E}{kW_+(k)}, \tag{6.46}$$

$$\bar{\phi}_2(k, y) = \frac{E}{k\tanh kW_+(k)}. \tag{6.47}$$

In the next section we will determine the function $W_+(k)$ and then apply the inverse Fourier transform to equations (6.46) and (6.47) to generate a formula for the interface profile.

6.3.1 Factorisation of $G_2(k)$

In this section we will factorise the denominator $G_2(k)$ given by equation (6.34) into two functions which are analytic and nonzero in the upper and lower $k-$planes following the same way that was presented in the paper by McCue & Stump [85] and discussed in Section 1.3.2 of Chapter 2.

Let us rewrite function $G_2(k)$ from equation (6.34) in the following way:

$$G_2(k) = \left[\frac{\sinh k}{k}(1-a) - F^2(a\sinh k + \cosh k)\right]\frac{k}{\sinh k} = f_1(k)f_2(k), \tag{6.48}$$

where

$$f_1(k) = \left[\frac{\sinh k}{k}(1-a) - F^2(a\sinh k + \cosh k)\right], \tag{6.49}$$

and

$$f_2(k) = \frac{k}{\sinh k}. \tag{6.50}$$

Splitting of $f_1(k)$ depends upon the value of the Froude number and the density ratio a. When the Froude number $F < 1$ and the density ratio $a < 1$, there are two real roots denoted by $k = \pm\mu$, of f_1 and infinitely many imaginary roots denoted by $k = \pm i\pi u_n$ for $n = 1, 2, 3, \ldots$. Then the function f_1 is factorised, using the Weierstrass infinite product theorem [29], into the form

$$f_1(k) = \left(1 - a - F^2\right)\left(1 - \frac{k^2}{\mu^2}\right)\prod_{n=1}^{\infty}\left(1 - \frac{ik}{\pi u_n}\right)\left(1 + \frac{ik}{\pi u_n}\right). \tag{6.51}$$

Following McCue and Stump [85], f_1 can be written as

$$f_1(k) = \Big(1 - a - F^2\Big)\Big(1 - \frac{k^2}{\mu^2}\Big)R(k)R(-k), \tag{6.52}$$

where function

$$R(k) = \frac{\mu F D(k)}{\sqrt{\pi(1-F^2)}\Gamma(3/2 - ik/\pi)}, \tag{6.53}$$

is analytic every where, with zeros at $k = -i\pi u_n$ for $n = 1, 2, 3, ...$ and $D(k)$ is given by

$$D(k) = \prod_{n=1}^{\infty}\Big(1 + \frac{u_n - [n + 1/2]}{n + 1/2 - ik/\pi}\Big). \tag{6.54}$$

Using the properties of gamma function in the complex plane ([67], page 256, 6.1.31), the function f_2 is also can be written as

$$f_2(k) = \frac{k}{\sinh k} = Q(k)Q(-k), \tag{6.55}$$

where

$$Q(k) = \Gamma\Big(1 - ik/\pi\Big) \tag{6.56}$$

is analytic and non-zero in the upper-half plane, with poles $k = -in\pi$, for $n = 1, 2, ...$ Then equation (6.48) can be written as

$$\begin{aligned} G_2(k) &= f_1(k)f_2(k), \\ &= \Big(1 - a - F^2\Big)\Big(1 - k^2/\mu^2\Big)R(k)R(-k)Q(k)Q(-k), \\ &= W_+(k)W_-(k), \end{aligned}$$

where

$$W_+(k) = \Big(1 - a - F^2\Big)\Big(1 - k^2/\mu^2\Big)R(k)Q(k),$$

this implies that using equations (6.53) and (6.56), $W_+(k)$ becomes

$$W_+(k) = \frac{\mu F\Big(1 - a - F^2\Big)\Big(1 - k^2/\mu^2\Big)\Gamma\Big(1 - ik/\pi\Big)D(k)}{\sqrt{\pi(1-F^2)}\Gamma(3/2 - ik/\pi)} \tag{6.57}$$

and

$$W_-(k) = R(-k)Q(-k) = \frac{\mu F\Gamma\Big(1 + ik/\pi\Big)D(-k)}{\sqrt{\pi(1-F^2)}\Gamma(3/2 + ik/\pi)}. \tag{6.58}$$

6.4 Calculation of the interface shape $\eta_1(x,t)$

In this section the shape of the interface between two layers is calculate as follows. Substituting equations (6.46) and (6.47) into equation (6.21), we obtain

$$\bar{\phi}_1(k,y) = \int_{-\infty}^{\infty} \phi_1(x,y)e^{ikx}dx = -\frac{E}{kW_+(k)}, \tag{6.59}$$

and

$$\bar{\phi}_2(k,y) = \int_{-\infty}^{\infty} \phi_1(x,y)e^{ikx}dx = \frac{E}{k\tanh kW_+(k)}. \tag{6.60}$$

Applying the inverse Fourier transform, the solution for $\phi_1(x,y)$ and $\phi_2(x,y)$ can be expressed as

$$\phi_1(x,y) = -\frac{1}{2\pi i}\int_{-\infty+i\delta}^{\infty+i\delta} \frac{E}{kW_+(k)}e^{-ikx}dk, \tag{6.61}$$

and

$$\phi_2(x,y) = \frac{1}{2\pi i}\int_{-\infty+i\delta}^{\infty+i\delta} \frac{E}{k\tanh kW_+(k)}e^{-ikx}dk, \tag{6.62}$$

where δ is a positive constant so that the poles along the real k-axis lies below the inversion contour. To use the formula for the interface profile, equation (6.20), we need to determine the derivative of $\phi_1(x,y)$ and $\phi_2(x,y)$ with respect to x, namely

$$\frac{\partial\phi_1}{\partial x}(x,y) = \frac{1}{2\pi}\int_{-\infty+i\delta}^{\infty+i\delta} \frac{E}{W_+(k)}e^{-ikx}dk, \tag{6.63}$$

and

$$\frac{\partial\phi_2}{\partial x}(x,y) = -\frac{1}{2\pi}\int_{-\infty+i\delta}^{\infty+i\delta} \frac{E}{\tanh kW_+(k)}e^{-ikx}dk. \tag{6.64}$$

Then, substituting equation (6.63) and (6.64) into equation (6.20) gives the location of the free surface as

$$\eta_1(x) = \frac{F^2}{1-a}\frac{E}{2\pi}\int_{-\infty+i\delta}^{\infty+i\delta} \frac{a+\coth k}{W_+(k)}e^{-ikx}dk, \tag{6.65}$$

where $W_+(k)$ is given in equation (6.57) and E can be determined from the separation point between the flat plate and the free surface, which follows from the condition $\eta_1(x) = -1$.

By examination of the expression for $\eta_1(x)$, we find that $\eta_1(x)$ has a pole at the origin, two poles at $k = \pm\mu$, and infinitely many poles at $k = -i\pi u_m$. By closing the contour in the lower half-plane and using residue theorem, the location of the interface as given by equation (6.65) can be presented finally in the form

$$\begin{aligned}
\eta_1(x) \quad &= \quad \frac{E\sqrt{\pi(1-F^2)}}{F(1-a-F^2)}\Bigg[\frac{-\mu(1/2-i\mu/\pi)\Gamma(i\mu/\pi)e^{-i\mu x}}{(1-a-\mu F^2 a)\Gamma(1/2+i\mu/\pi)\prod_{n=1}^{\infty}\left(1+\frac{u_n-[n+1/2]}{n+1/2-i\mu/\pi}\right)} \\
&+ \quad \frac{\mu(1/2+i\mu/\pi)\Gamma(-i\mu/\pi)e^{i\mu x}}{(1-a+\mu F^2 a)\Gamma(1/2-i\mu/\pi)\prod_{n=1}^{\infty}\left(1+\frac{u_n-[n+1/2]}{n+1/2+i\mu/\pi}\right)} \\
&+ \frac{u_m\mu^2F^2\prod_{n=1}^{\infty}\left(1+\frac{u_n-(n+1/2)}{n+1/2+\pi u_m}\right)\Gamma(u_m)e^{-\pi u_m x}}{(1-a+i\pi u_m F^2 a)(1-F^2+\pi^2 u_m^2 F^4)\Gamma(1/2+u_m)}\Bigg]. \qquad (6.66)
\end{aligned}$$

In the next section we present the calculation of the interface shape for different parameters and discuss the results obtained.

6.5 Conclusion

The steady two-dimensional flow past a semi-infinite flat plate in a fluid of finite depth for the two layer model is solved analytically using the Fourier transform and the Wiener–Hopf technique for the subcritical case, $F < 1$. This problem can be considered as a free-surface problem similar to the problem solved in Chapter 2, if we assume that the density ratio $\rho_1/\rho_2 = 0$.

The interface profiles given by equation (6.66) are computed for two values of Froude number and different values of density ratio as shown in figure 6.2 (a) and (b). When density ratio is small (i.e., the density difference between the layers is relatively big), wave amplitudes are smaller than in the case when the density ratio is close to one (i.e., small density difference). It is quite natural as in the later case even small external force can cause large amplitude perturbation, due to buoyancy force is rather small when the density difference between the layers is negligible.

Increase of the Froude number leads to the increase of wave period (cf. panels (a) and (b) in figure 6.2), whereas the amplitudes remain almost the same.

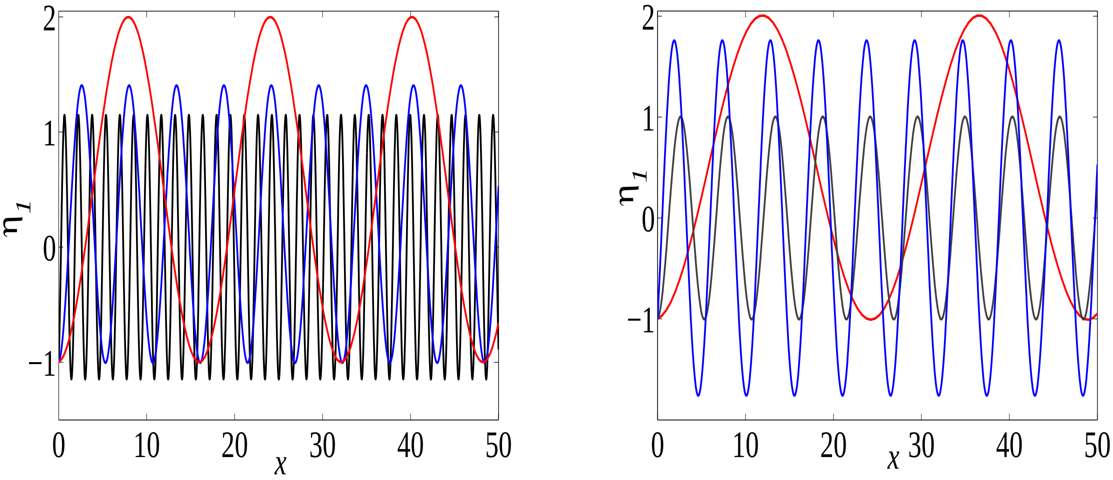

(a) (b)

FIGURE 6.2: This figure shows the interface profile for different values of a: black line – $a = 0$, blue line – 0.5, red line – 0.7. Panel (a) – Froude number $F = 0.5$, and panel (b) – $F = 0.7$.

The relation between the wave amplitude A and the density ratio $a = \rho_1/\rho_2$ for Froude numbers $F = 0.5$ and 0.7 are shown in figure 6.3(a). As one can see from this figure, the wave amplitude increases when the density ratio a growths. Similarly the wavelength λ monotonically increases too when the density ratio growths. This can be seen from figure 6.3(b). In the meantime, the curve $A(a)$ for $F = 0.5$ is above the similar curve for $F = 0.7$, whereas the curve $\lambda(a)$ for $F = 0.5$ is below the similar curve for $F = 0.7$. The detailed dependence of these parameters on the Froude number will be a subject of a separate study in the future.

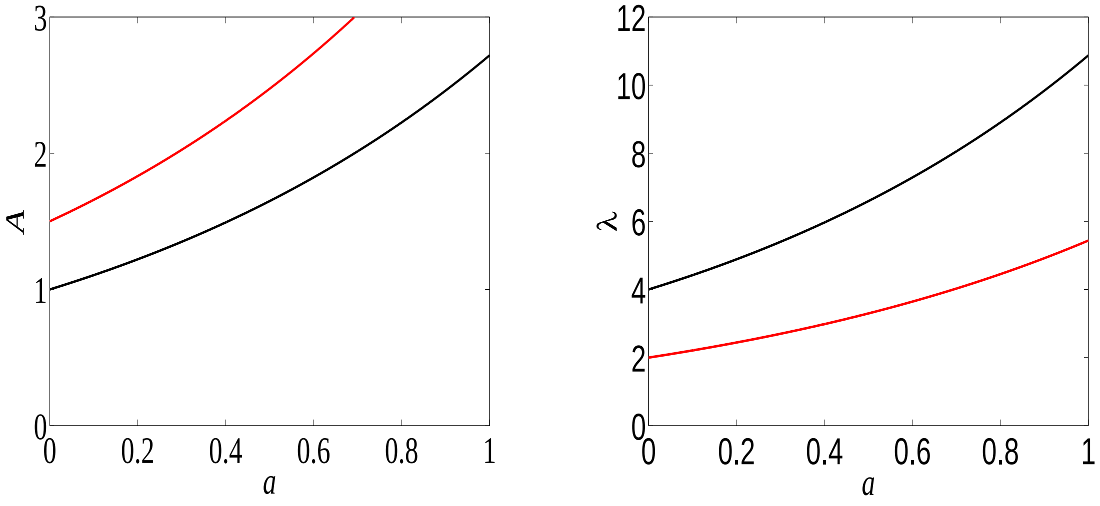

FIGURE 6.3: This figure shows the dependence of wave amplitude (a) and wavelength (b) on the density ratio for two values of Froude number: $F = 0.5$ (red line) and $F = 0.7$ (black line).

Chapter 7

Conclusion and Future Work

7.1 Research Outcomes

This research aimed to design in a perspective a ship stern that may effectively minimise or eliminate downstream waves. It has been shown in this Theses that such aim can be achieved for certain models of stern shapes. This has been demonstrated both numerically and theoretically by means of linear and weakly nonlinear solutions. For stern shapes that have the downward point separating with the free surface were determined to have eliminated the wave amplitude downstream.

Within the framework of linearised steady problem, the solution was derived for the free surface past a curved plate. The free surface was then analysed using the Fourier transform and Wiener–Hopf methods. The resultant Wiener–Hopf equation was solved for relatively small Froude numbers $F < 1$ using the factorisation method. The derived formula is applicable to a stern of any shape in contrast to the problem solved by McCue and Stump [85] for the flat plate case only.

The numerical solution to the fully nonlinear problem for the stationary problem presented in Chapter 2 was solved in Chapter 3, using the conformal mapping. The problem was transformed from the physical plane to the non-physical plane where the free surface is known. It enabled Cauchy's integral theorem to be applied. The boundary integral equation method was also used to derive an integral equation for the unknown free surface. A system of nonlinear equations was derived and then solved by Newton's method. Chapter 3 presents the novel numerical algorithm developed in the Theses to generate the free surface profile past different stern shapes.

The exact solution to the weakly nonlinear problem was derived and presented in Chapter 4. The solution was constructed with the help of the phase plane. Comparisons of linear and nonlinear solutions for different families of stern shapes (curved plates) were also presented. This chapter presents also a comparison of the results of simulation with the results known from the literature for the flat plate case. It has been demonstrated that the solution to the free surface flow past a flat plate in a fluid of finite depth is reasonably accurate.

Chapter 5 contains the solution to the linearised non-stationary problem of free surface flow development past a flat plate suddenly submerged into the flow at small depth. The problem formulation is presented under basic assumptions. The solution for free surface is derived with on the basis of application of the Laplace and Fourier transforms, as well as Wiener–Hopf method. The method of numerical solution to the derived equation was developed with the help of the best rational approximation for the inverse Laplace transform. The free surface profile has been plotted for short and long times using rather complex and sophisticated formula. It has been demonstrated that the unsteady solution eventually approaches the steady state solution as $t \to \infty$. The transition to the steady state has been studied in details. In particular, it has been shown that the large-amplitude splash arises at the beginning and then wave amplitude non-monotonically approaches the steady state value.

Chapter 6 is devoted to problem generalisation to internal waves generation in two-layer fluid past stationary moving stern. The problem has been formulated for the case when the lower layer has finite depth, whereas the upper layer is infinite. The solution to this problem was derived in the linear approximation using the Fourier transform and Wiener–Hopf method. The influence of the density aspect ratio has been analysed. It has been confirmed that in the limit of zero density of the upper layer the solution derived for two-layer model reduces to the solution for free-surface case.

7.2 Future Directions

This research examined the effect of different families of stern shapes to eliminate waves past the stern and hence minimise the wave drag for the ship model. The results obtained can be used to model the flow near the stern of a wide blunt ship. While two-dimensional models do not describe real bow and stern flows exactly, they are useful for understanding the details of wave generation by mowing blunt body and, to certain extant, can provide valuable information about flow structure in the near-stern zone. In particular, the results show that the wave amplitude can be minimised in two-dimensional case and, perhaps, in three-dimensional case too. The three-dimensional case is much more complicated and is challenging for future study.

A number of extensions to further research of steady and unsteady problems are possible. In particular, the solutions obtained in the Theses by means of linear approximation and within the framework of weakly nonlinear model, apparently, can be further improved and tested numerically in the original Navier–Stokes equation. While the linearised unsteady problem of the free surface flow past a semi-infinite *flat* plate in a fluid of finite depth has been solved in the Theses, further study is highly desirable to describe the case of semi-infinite *curved* plate. The aim is to find such families of plate shapes which may provide trailing waves of minimal amplitude. Such a problem may be solved on the basis of technique developed in this work.

The case of two-layer fluid was only briefly considered in the Theses. However the problem of wave minimisation on the interface between two layers of a fluid of different densities is also very interesting and topical. The problem can be even further generalised for smoothly stratified fluid. Again sterns of different shapes can be studied both theoretically and numerically. The dependences of results on the density aspect ratio or character of stratification, as well as the depth layer ratio should be studied.

Appendix A

Relation Between P and ϵ

From the Bernoulli equation,

$$\frac{1}{2}V^2 + gh + \frac{\tilde{P}_{-\infty}}{\rho} = \frac{1}{2}c^2 + gH + \frac{\tilde{P}_a}{\rho},$$

by using Eq. (2.1) divided by gh, we can be write down

$$\frac{1}{2}F^2\left(1 - \frac{h}{H}\right) - \frac{H}{h} + 1 = \frac{\tilde{P}_a - \tilde{P}_{-\infty}}{\rho g h}$$

where $F = V/\sqrt{gh}$. Defining $P = (\tilde{P}_{-\infty} - \tilde{P}_a)/\rho g h$, we can express the equation written above as (note that $h/H = 1 - \epsilon$):

$$\frac{1}{2}F^2\left[1 - (1-\epsilon)^2\right] - \left(\frac{1}{1-\epsilon}\right) + 1 = -P. \tag{A.1}$$

With the help of Taylor expansion around $\epsilon = 0$, we find

$$\frac{1}{2}F^2\left[1 - (1 - 2\epsilon + \epsilon^2)\right] - (1 + \epsilon + \epsilon^2 + ...) + 1 = -P,$$

which implies that

$$\epsilon = \frac{P}{1-F^2} + O(\epsilon^2),$$

and hence, for $\epsilon \ll 1$ we can use the approximate relationship

$$\epsilon \approx \frac{P}{1-F^2}. \tag{A.2}$$

Appendix B

Consideration of the Infinite Product $T(k)$

This appendix shows the calculation of the infinite product $T(k)$ in Chapter 2. In Tables B.2 and B.3, the real and imaginary parts of the infinite product $T(\mu_R)$ are shown for different Froude numbers and integer values, N. Table B.4 shows the calculation of the infinite product $T(i\pi\mu_m)$, for different values of the Froude number, and $m = 1$, 100 and 1000 as given by (2.81). The result is accurate to 7 significant places when $N = 10^4$ and $m = 1$.

The exact and approximation values of the ratio

$$\frac{\Gamma(\mu_m)}{\Gamma(\frac{1}{2}+\mu_m)} \tag{B.1}$$

is computed using Maple 12. The approximate values of this ratio are computed for different values of m via Stirling's formula [67],

$$\frac{\Gamma(\mu_m)}{\Gamma(\frac{1}{2}+\mu_m)} \sim \frac{1}{\mu_m^{1/2}} + \frac{1}{8\mu_m^{3/2}} + \frac{1}{128\mu_m^{5/2}}. \tag{B.2}$$

It is very accurate, as can be seen in Table B.1.

m	exact	approximate
10	0.312889751	0.312891082
50	0.141079516	0.141079521
100	0.099877087	0.099877087
169	0.076866745	0.076866745
200	0.070666854	0.070666854
1000	0.031618830	0.031618830

TABLE B.1: This table shows calculation of the exact values of the ratio $\Gamma(\mu_m)/\Gamma(\frac{1}{2}+\mu_m)$, and the approximation values by using Stirling's formula, for different values of the integer m, when the Froude number $F = 0.5$.

Real part of $T(\mu_R)$				
F	$N = 10^2$	$N = 10^3$	$N = 10^4$	$N = 10^5$
0.35	0.702426646	0.697256224	0.696737560	0.696737665
0.5	0.752736684	0.750023284	0.749750122	0.749750119
0.65	0.814755841	0.813017838	0.812842581	0.812842570
0.8	0.864510225	0.863292569	0.863169352	0.863169351
0.95	0.898969000	0.898071033	0.897980933	0.897980932
0.99	0.906129897	0.905296339	0.905213082	0.905213080

Imaginary part of $T(\mu_R)$				
F	$N = 10^2$	$N = 10^3$	$N = 10^4$	$N = 10^5$
0.35	−0.183490507	−0.182217505	−0.182082802	−0.182082264
0.5	−0.110048865	−0.109671347	−0.109631580	−0.109631560
0.65	−0.055203066	−0.055092317	−0.055080469	−0.055080354
0.8	−0.025267980	−0.025235292	−0.025231780	−0.025231785
0.95	−0.008096851	−0.008089657	−0.008088816	−0.008088451
0.99	−0.003247759	−0.003245125	−0.003244824	−0.003244320

Table B.2: This table shows the calculation of the real and imaginary part of the infinite product $T(\mu_R)$, for different values of the Froude number F, for the first N terms.

Real part of $T(\mu_R)$				
F	$N = 10^2$	$N = 10^3$	$N = 10^4$	$N = 10^5$
0.35	0.702426646	0.696680400	0.696680117	0.696680114
0.5	0.752736684	0.749719793	0.749719614	0.749719612
0.65	0.814755841	0.812823266	0.812823169	0.812823168
0.8	0.864510225	0.863156163	0.863156095	0.863156094
0.95	0.898969000	0.897970361	0.897970311	0.897970310
0.99	0.906129897	0.905296339	0.905296318	0.905296315
Imaginary part of $T(\mu_R)$				
F	$N = 10^2$	$N = 10^3$	$N = 10^4$	$N = 10^5$
0.35	-0.183490507	-0.182067833	-0.182067759	-0.182067758
0.5	-0.110048865	-0.109627138	-0.109627116	-0.109627116
0.65	-0.055203066	-0.055079209	-0.055079203	-0.055079203
0.8	-0.025267980	-0.025231340	-0.025231338	-0.025231338
0.95	-0.008096851	-0.008088755	-0.008088755	-0.008088816
0.99	-0.003247759	-0.003245125	-0.003245125	-0.003245124

TABLE B.3: This table shows the calculation of the real and imaginary part of the infinite product $T(\mu_R)$, for different values of the Froude number F after N terms, given by equation (2.80).

$T(i\pi\mu_m)$				
F	$N = 10^2$	$N = 10^3$	$N = 10^4$	$N = 10^5$
$m = 1$				
0.35	0.639707391	0.635043339	0.634519171	0.634519168
0.5	0.780091693	0.777301138	0.776986776	0.776986774
0.65	0.862012932	0.860187780	0.859982098	0.859982095
0.8	0.907656427	0.906387651	0.906244542	0.906244541
0.95	0.934337759	0.933411686	0.933307016	0.933307016
0.99	0.939528969	0.938671464	0.938582240	0.938582235
$m = 100$				
0.35	0.971233847	0.966489626	0.965728921	0.965728914
0.5	0.984641131	0.982281040	0.981902482	0.981902478
0.65	0.990703525	0.989298331	0.989095055	0.989072119
0.8	0.993834642	0.992903949	0.992753941	0.992753940
0.95	0.995626556	0.994965242	0.994858679	0.994858677
0.99	0.995973312	0.995363997	0.995274212	0.995274208
$m = 10000$				
0.35	0.999651731	0.999469070	0.999287045	0.999271106
0.5	0.999817204	0.999727789	0.999639545	0.999630629
0.65	0.999889916	0.999836826	0.999773151	0.999779545
0.8	0.999927143	0.999891889	0.999853915	0.999854263
0.95	0.999948342	0.999923831	0.999898840	0.999896674
0.99	0.999952445	0.999929930	0.999920766	0.999920760

TABLE B.4: This table shows the calculation of the infinite product $T(i\pi\mu_m)$, for different values of the Froude number F, given by (2.81). The calculation been made after N terms for different values of m.

Appendix C

Evaluation $I(x, z/t)$ and The Roots Of $f_1(k, z/t)$ For Different Values Of z

Ten values of z_j are used here to evaluate the roots of function f_1, given by equation (5.72), at $t = 1$, $F = 0.5$ and various values of z.

For each value of z_j function f_1 has the infinite number of complex roots in the upper half-plane (they are denoted by $\tilde{\zeta}_l$, $l = 1, 2, 3, \ldots$) and infinite number of complex roots in the lower half-plane (they are denoted by ζ_j, $j = 1, 2, 3, \ldots$. But the roots ζ_j and $\tilde{\zeta}_l$ are different for each particular value of z_j as shown in the Figs. C.1 – C.5. This leads to different functions $G_1(k, z/t)$ and then, different functions $I(x, z/t)$, correspondingly.

So we have the general formulae for $I(x, z/t)$ and $G_1(k, z/t)$:

$$I_r(x, z_r/t) = -iE\Bigg(A_r + iB_r\Bigg), \quad \text{for} \quad r = 1, 2, \ldots, 10, \tag{C.1}$$

where

$$A_r = \frac{3 + 0.183755(z_r/t)}{(z_r/t)^2 F^2}, \tag{C.2}$$

and

$$B_r = \prod_{j=1}^{\infty} \frac{(i\zeta_j - z_r/t)\Gamma\Bigg(1 + \frac{i\zeta_j}{\pi}\Bigg)\cosh(\zeta_j)e^{-i\zeta j x}}{\zeta_j (z_r/t)^2 e^{1+2it\zeta j/z_r}}. \tag{C.3}$$

$$\begin{aligned} G_1(k,z_r/t) &= \frac{1}{k^2} f_1(k,z_r/t) f_2(k,z_r/t) \\ &= \frac{1}{k^2}\Gamma\left(1-\frac{ik}{\pi}\right)\Gamma\left(1+\frac{ik}{\pi}\right)(z_r/t)^2 F^2 e^{2itk/z_r}\prod_{l=1}^{\infty}\left(1-\frac{k}{\tilde{\zeta}_l}\right)e^{k/\tilde{\zeta}_l}\prod_{j=1}^{\infty}\left(1-\frac{k}{\zeta_j}\right)e^{k/\zeta_j}, \\ &= \frac{1}{k^2}K_-(k,z_r/t)K_+(k,z_r/t), \quad \text{for} \quad r=1,2,\ldots,10, \end{aligned}$$

where

$$K_+(k,z_r/t) = (z_r/t)^2 F^2 e^{2itk/z_r}\Gamma\left(1-\frac{ik}{\pi}\right)\prod_{j=1}^{\infty}\left(1-\frac{k}{\zeta_j}\right)e^{k/\zeta_j}, \quad \text{for} \quad r=1,2,\ldots,10, \tag{C.4}$$

and

$$K_-(k,z_r/t) = \Gamma\left(1+\frac{ik}{\pi}\right)\prod_{l=1}^{\infty}\left(1-\frac{k}{\tilde{\zeta}_l}\right)e^{k/\tilde{\zeta}_l}, \quad \text{for} \quad r=1,2,\ldots,10. \tag{C.5}$$

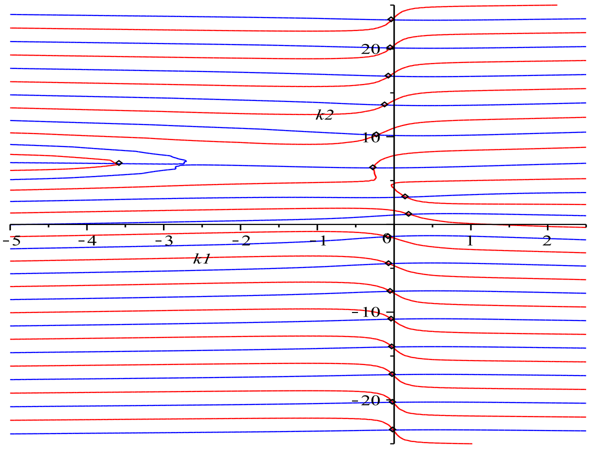

FIGURE C.1: Zero isolines of functions $\mathrm{Re} f_1(k,z/t)$ (blue lines) and$\mathrm{Im} f_1(k,z/t)$ (red lines). Dots indicate intersection points of isolines. The plot was generated for $F=0.5$, $t=1$ and $z_2 = 4.0277 - 1.1939i$.

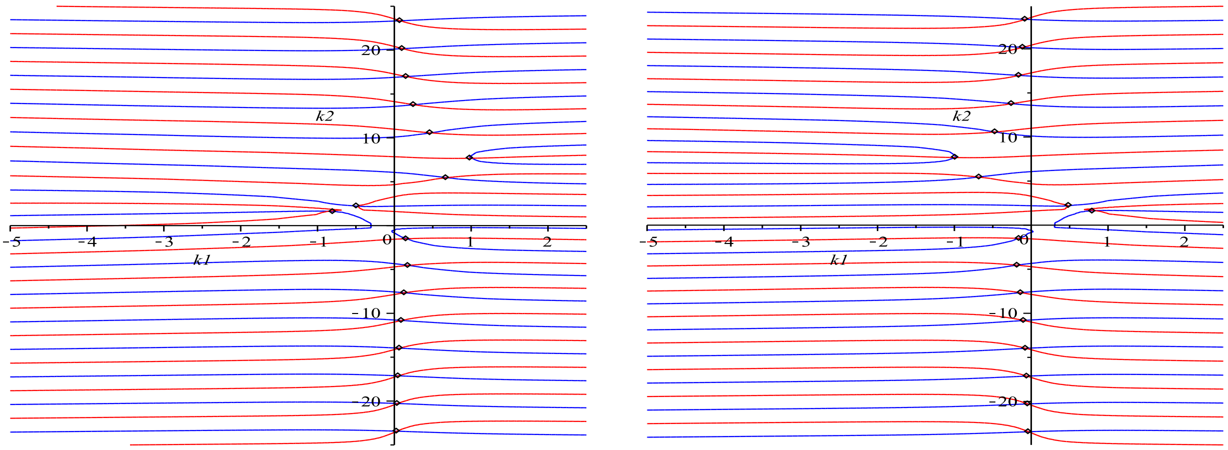

(a) (b)

FIGURE C.2: Zero isolines of functions Re$f_1(k, z/t)$ (blue lines) and Im$f_1(k, z/t)$ (red lines). Dots indicate intersection points of isolines. The plot was generated for $F = 0.5$, $t = 1$ and $z_3 = 3.2838 + 3.5944i$, $z_4 = 3.2838 - 3.5944i$ in figure (a) and (b) respectively.

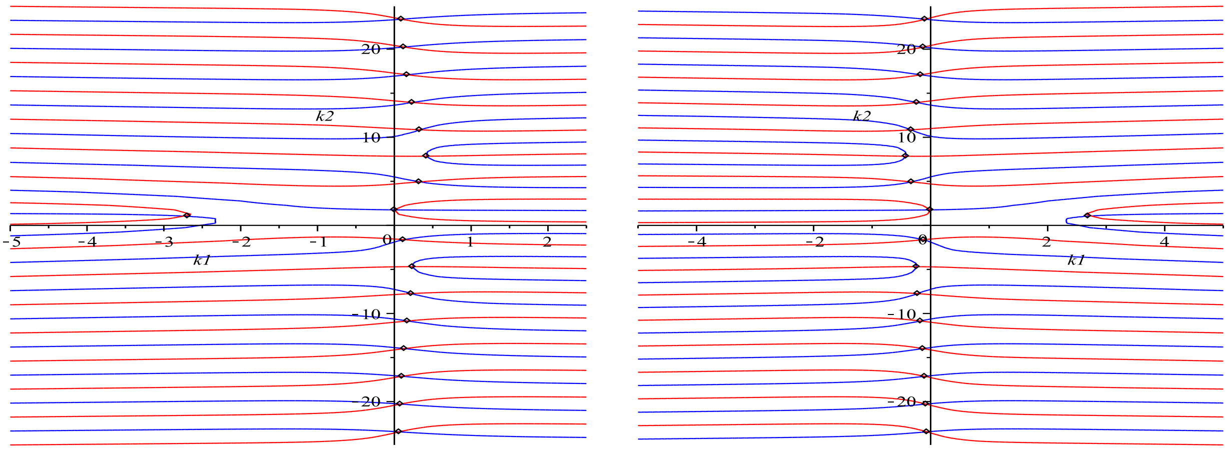

(a) (b)

FIGURE C.3: Zero isolines of functions Re$f_1(k, z/t)$ (blue lines) and Im$f_1(k, z/t)$ (red lines). Dots indicate intersection points of isolines. The plot was generated for $F = 0.5$, $t = 1$ and $z_5 = 1.7154 + 6.0389i$, $z_6 = 1.7154 - 6.0389i$ in figure (a) and (b) respectively.

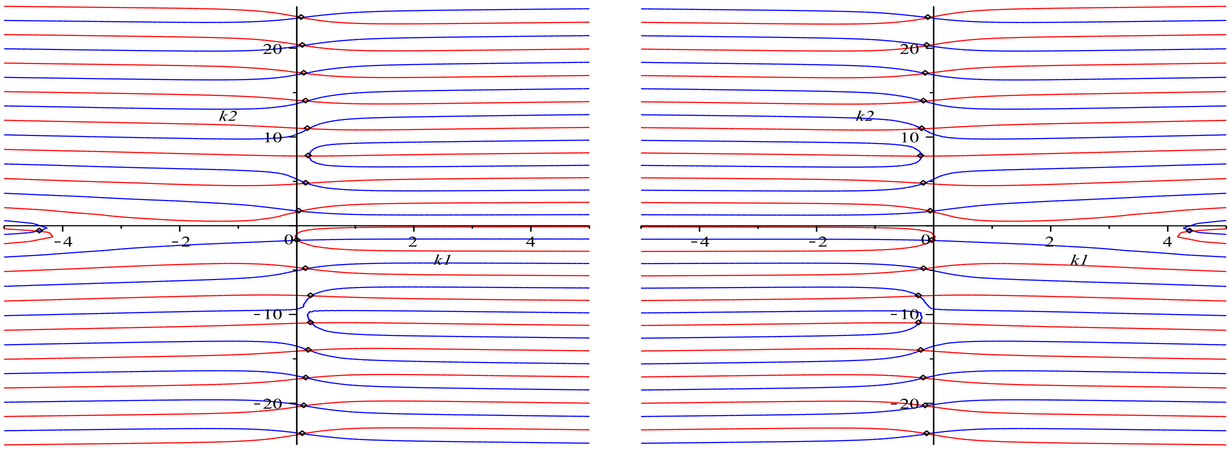

(a) (b)

FIGURE C.4: Zero isolines of functions $\mathrm{Re} f_1(k, z/t)$ (blue lines) and $\mathrm{Im} f_1(k, z/t)$ (red lines). Dots indicate intersection points of isolines. The plot was generated for $F = 0.5$, $t = 1$ and $z_7 = -0.8944 + 8.5828i$, $z_8 = -0.8944 - 8.5828i$ in figure (a) and (b) respectively.

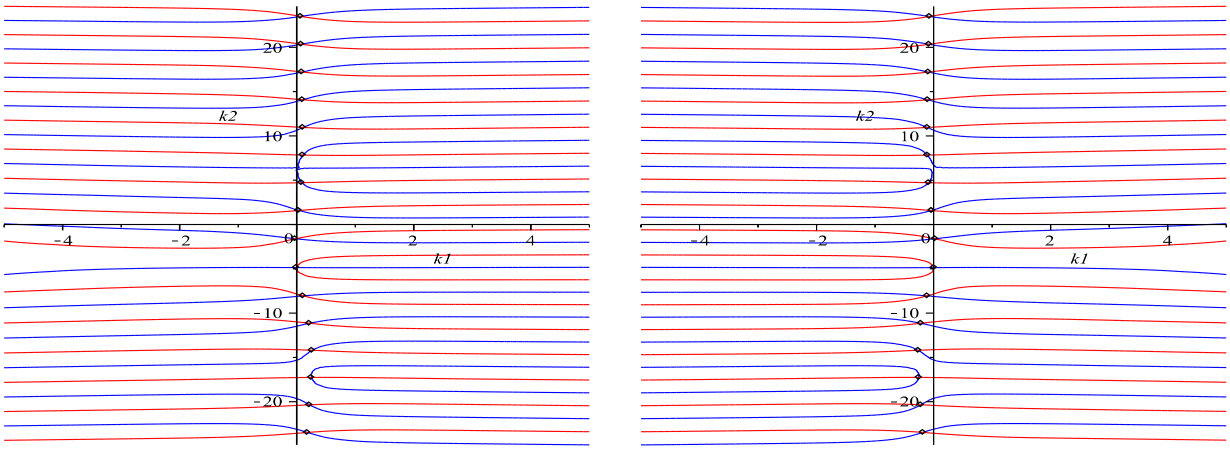

(a) (b)

FIGURE C.5: Zero isolines of functions $\mathrm{Re} f_1(k, z/t)$ (blue lines) and $\mathrm{Im} f_1(k, z/t)$ (red lines). Dots indicate intersection points of isolines. The plot was generated for $F = 0.5$, $t = 1$ and $z_9 = -5.1612 + 11.3752i$, $z_{10} = -5.1612 - 11.3752i$ in figure (a) and (b) respectively.

References

[1] A. C. King and M. I. G. Bloor, Free-surface flow over a step, *J. Fluid Mech.*, 182:193-208, 1987.

[2] A. M. J. Davis, Continental shelf wave scattering by a semi-infinite coastline, *Geophys, Astrophys, Fluid Dynamics*, 39:25-55, 1987.

[3] A. Merzougui, H. Mekias and F. Guechi, Surface tension effect on a two dimensional channel flow a gainst an inclined wall, *Applied Mathematics Science*, 47:2313-2326, 2007.

[4] A. N. Norris and J. D. Achenbach, Elastic wave diffraction by a semi-infinite crack in a transversely isotropic material, *Quart. J. Mech. Appl. Math.*, 37:565-580, 1984.

[5] B. Noble, *Methods Based on the Wiener–Hopf technique*, Chelsea Press, New York, 1988.

[6] B. J. Binder and J. M. Vanden-Broeck, Free surface flow past surfboards and sluice gates, *Euro. Jnl. of Applied Mathemtics*, 16:601-619, 2005.

[7] B. J. Binder and J. M. Vanden-Broeck, The effect of disturbances on the flows under a sluice gate and past an inclined plate, *J. Fluid Mech.*, 576:475-490, 2007.

[8] B. J. Binder, J. M. Vanden-Broeck and F. Dias. On satisfying the radiation condition in free surface flows, *J. Fluid Mech.*, 624:179-189, 2009.

[9] B. J. Binder, F. Dias and J. M. Vanden-Broeck, Steady free surface flow past an uneven channel bottom, *Theor. Comput. Fluid Dyn.*, 20:125-144, 2006.

[10] B. J. Binder, F. Dias and J. M. Vanden-Broeck, Influence of rapid changes in a channel bottom on free surface flows, *IMA Journal of Applied Mathematics*, 73:254-273, 2008.

[11] B. J. Binder, Steady free-surface flow at the stern of a ship, *Physics of Fluids*, 22:012104, 2010.

[12] C. D. Andersson and J.M. Vanden-Broeck, Bow flows with surface tension, *Proc. R. Soc. London*, 452:1985-1997, 1996.

[13] D. E. Farrow, and E. O. Tuck, Further studies of stern wavemaking, *J. Austral. Math. Soc. Ser.*, 36B:424-437, 1995.

[14] D. I. Meiron and P. G. Saffman, Overhanging interfacial gravity waves of large amplitude, *J. Fluid Mech.*, 129:213-218, 1983.

[15] D. I. Meiron G. R. Baker and S. A. Orszag, Generalized vortex methods for free-surface flow problems, *J. Fluid Mech.*, 123:477-501, 1982.

[16] D. S. Jones, A simplifying technique in the solution of a class of diffraction problems, *Quart. J. Math.*, 3:189-196, 1952.

[17] D. V. Boger, C. Tiu and P.H. T. Uhlherr, *Rheology and Flow of Non-Newtonian Systems*, Dept. of Chemical Engineering, Monash University, Melbourne, 1976.

[18] E. C. Titchmarsh, *Theory of Fourier Integrals*, Oxford University Press, New York, 1948.

[19] E. C. Titchmarsh, *The Theory of Function Theory*, Oxford University Press, London, 1939.

[20] E. O. Tuck, and J. M. Vanden-Broeck, A cusp-like free-surface flow due to a submerged source or sink, *J. Austral. Math. Soc. Ser.*, 25B:443-450, 1984.

[21] E. O. Tuck, Shallow water flows past slender bodies, *J. Fluid Mech.*, 26:81-95, 1966.

[22] E. O. Tuck, Low aspect ratio flat ship theory, *J. Hydronaut*, 9:1-12, 1975.

[23] E. Palm, J. Grue, On the wave field due to a moving body performing oscillations in the vicinity of the critical frequency, *J. Engng. Math. 3*, 5:219-232, 1999.

[24] E. Varley and J. D. A. Walker, Method for solving singular integrodifferential equation, *IMAJ. Appl. Math.*, 43:11-45, 1989.

[25] F. Dias and J. M. Vanden-Broeck. Trapped waves between submerged obstacles, *J. Fluid Mech.*, 509:93-102, 2004.

[26] F. M. White, *Viscous Fluid Flow*, McGraw-Hill, New York, 1991.

[27] G. Birkhhoff and E. Zarantonello. Jets, *Wakes and Cavities*, New York, 1957.

[28] G. C. Hocking, Bow flows with smooth separation in water of finite depth, *J. Austral. Math. Soc.*, 35B:114-126, 1993.

[29] G. F. Carrier, M. Krook and C. E. Pearson, *Function of Complex Variable: Theory and technique*, Mcgraw-Hill, USA, 1966.

[30] G. H. Schmidt, Linearised stern flow of a two-dimensional shallow-draft ship, *Journal of Ship Research*, 236-242, 1981.

[31] G. H. Schmidt and J. A. Sparenberg, On the linearised theory of hub cavity with swirl, *National Academy of Science*, 348-361, 1979.

[32] H. J. Haussling, Two-dimensional linear and nonlinear stern waves, *J. Fluid Mech.*, 79:759-769, 1980.

[33] H. Lamb, *Hydrodynamics*, Canbridge university press, UK, 1993.

[34] H. Maruo, High and low aspect ratio approximation of planing surfaces, *Schiffstechnik*, 14:57-64, 1967.

[35] H. Zhang and G. C. Hocking, Withdrawal of layer fluid through a line sink in a porous medium, *J. Austral. Math. Soc. Ser.*, 38B:240-254, 1996.

[36] H. Zhang and G. C. Hocking, Axisymmetric flow in an oil resevoir of finite depth caused by a point sink above an oil-water interface, *J. Eng. Math.*, 32:365-376, 1997.

[37] I. D. Abrahams and G. R. Wicham, General Wiener–Hopf factorization of matrix kernels with exponential phase factors, *SIAM J. Appl. Math.*, 50:819-838, 1990.

[38] I. G. Currie, *Fundamental Mechanics of Fluids*, Marcel Dekker, New York, 2003.

[39] I. Ten and M. Kashiwagi, Hydrodynamics of a body floating in a two-layer fluid of finite depth, part 1,*Jouranl of Marine Science and Technology*, 9:127-141, 2004.

[40] J. Asavanant and J. M. Vanden-Broeck, Nonlinear free-surface flows emerging from vessels and flows under a sluice gate, *J. Austral. Math. Soc.*, 38B:63-86, 1996.

[41] J. Apel, L. A. Ostrovsky, Y. A. Stepanyants and J. F. Lynch, Internal solitons in the ocean and their effect on underwater sound, *J. Acoust. Soc. Am.*, 2007, v. 121, n. 2, 695–722.

[42] J. C. Amazigo, Fully plastic crack in an infinite body under Anti-Plane Shear, *Int. J. Solids Struct.*, 10:23-38, 1974.

[43] J. D. Hoffman, *Numerical Methods for Engineers and Scientists*, McGraw-Hill, Inc, 1992.

[44] J. J. Stoker, *Water Waves*, Wiley and Sons, 1958.

[45] J. J. Stoker 1957 *Water Waves: the Mathematical Theory with Applications,* NewYork, 1957.

[46] J. M. Vanden-Broeck, *Gravity-capillary free-surface flows*, Cambridge university press, UK, 2010.

[47] J. M. Vanden-Broeck, Nonlinear stern waves, *J. Fluid Mech.*, 96:603-611, 1980.

[48] J. M. Vanden-Broeck, Bow flows in water of finite depth, *Phys. Fluid Mech.*, 1A:1328-1330, 1989.

[49] J. M. Vanden-Broeck and E. O. Tuck, Computation of near-bow or stern flows using series expansion in the Froude number, *In Proc. 2nd Intl Conf. Numerical Ship Hydrodynamics, Berkeley, CA*, 371-381, 1977.

[50] J. M. Vanden-Broeck and J. B. Keller, Weir flows, *J. Fluid Mech.*, 176:283-293, 1987.

[51] J. M. Vanden-Broeck, L. W. Schwartz and E. O. Tuck, Divergent low-Froude-number series expansion in nonlinear free-surface flow problems, *Proc. R. Soc. London*, 361A:207-224, 1978.

[52] J. M. Vanden-Broeck, L. W. Schwartz and E. O. Tuck, Numerical computation of steep gravity waves in shallow water, *Phys. Fluids*, 22(10):1868-1871, 1979.

[53] J. H. Michell, The wave resistance of a ship, *Phil. Mag.*, 106-115, 1898.

[54] J. V. Wehausen, E. V. Laitone, *Surface waves,* Berlin, 1960.

[55] K. Subramanya, *Flow in Open Channels*, McGraw-Hill, 1986.

[56] L. D. Landau and F. M. Lifshitz, *Fluid Mechanics*, Pergamon press, UK, 1959.

[57] L. N. Trefethen, J. A. C. Weideman and T. Schmelzer, Talbot quadratures and rational approximation, *BIT Numerical Mathematics*, 653-670, 2006.

[58] L. N. Trefethen, M. H. Gutknecht, The Carathéodory-Fejér method for real rational approximation, *SIAM J. Num. Anal.*, 420-436, 1983.

[59] L. K. Forbes and L. W. Schwartz, Free-surface flow over a semicircular obstruction, *J. Fluid Mech.*, 114:299-314, 1982.

[60] L. K. Forbes, On the wave resistance of a submerged semi-elliptical body, *Journal of Engineering Mathemtics*, 15:287-298, 1981.

[61] L. K. Forbes, On the effects of non-linearity in free surface flow about a submerged point vortex, *Journal of Engineering Mathemtics*, 19:139-155, 1985.

[62] L. K. Forbes and G. C. Hocking, An intrusion layer in stationary incompressible fluid part 2: A solitary wave, *Euro. Jnl of Applied Mathematics*, 17:577-595, 2007.

[63] L. W. Schwartz, Computer extension and analytic continuation of Stokes'expansion for gravity waves, *J. Fluid Mech.*, 62:553-578, 1974.

[64] L. W. Schwartz and J. D. Fenton, Strongly nonlinear waves, *Ann. Rev.Fluid Mech.*, 14:39-60, 1982.

[65] M. A. Madurashingle, Splashless ship bows with stagnant attachment, *J. Ship Res.*, 32:194-202, 1988.

[66] M. A. Madurashingle and E. O. Tuck, Ship bows with continuous and splashless flow attachment, *J. Austral. Math. Soc.*, 27B:442-452, 1986.

[67] M. Abramowitz and I. A. Stegun, *Handbook of Mathematical Functions*, Dover, New York, 1970.

[68] M. G. Blyth and J.M. Vanden-broeck, Free surface flow over a trapped bubble, *IMA Journal of Applied Mathematics*, 10:1-12, 2008.

[69] M. G. Blyth and J. M. Vanden-Broeck, New solutions for capillary waves on curved sheets of fluid, *IMA Journal of Applied Mathematics*, 70:588-601, 2005.

[70] M. J. Lighthill, *Waves in Fluids*, Cambridge University Press, New York, 2001.

[71] M. Maleewong and R. H. J. Grimshaw, Nonlinear free surface flows past a semi-infinite flate plate in water of finite depth, *J. Fluid Mech.*, 062-102, 2008.

[72] M. Rahman, *Relating modern theory to advanced engineering application*, Clarendon Press, Oxford, 1995.

[73] M. Maleewong, J. Asavanant and R. Grimshaw, Free surface flow under gravity and surface tension due to an applied pressure distribution: I bond number greater than one-third, *Theor. Comut. Fluid. Dyn.*, 19(4):237-252, 2005.

[74] N. Wiener and E. Hopf, Uber eine Klasse singularer integralgleichungen, *S. B. Preuss. Akad. Wiss*, 696-706, 1931.

[75] O. Ogilat, S. W. McCue, I. W. Turner, J. A. Belward and B. J. Binder, Minimising wave drage for free surface flow past a two-dimensional stern, *Phys. Fluids*, 23: 07210001, 2011.

[76] P. A. Tyvand, Unsteady free surface flow due to a line source, *Physics of Fluids*, 4A:671-676, 1992.

[77] R. L. Panton, *Incompressible Flow*, Wiley-Interscience, New York, 1984.

[78] R. W. Yeung, Nonlinear bow and stern waves-inviscid and viscous solutions, In Mathematical Approaches in Hydrodynamics, *SIAM J. Appl. Math.*, 349-369, 1991.

[79] S. Cole, A simple example from flat ship theory, *J. Fluid Mech.*, 189:301-310, 1988.

[80] S. I. Pai, *Viscous Flow Theory*, Van Nostrand, 1956.

[81] S. J. Chapman and J. M. Vanden-Broeck, Exponential asymptotics and gravity waves, *J. Fluid Mech.*, 567:299-326, 2006.

[82] S. W. McCue and L. K. Forbes, Free-surface flows emerging from beneath a semi-infinite plate with constant vorticity, *J. Fluid Mech.*, 461:387-407, 2002.

[83] S. W. McCue and L. K. Forbes, Bow and stern flow with constant vorticity, *J. Fluid Mech.*, 399:277-300, 1999.

[84] S. W. McCue and L. K. Forbes, Smoothly attaching bow flows with constant vorticity, *ANZIAM. J*, 42:354-371, 2001.

[85] S. W. McCue and D. M. Stump, Linear stern in infinite depth channels, *Q. J Mech. Appl. Math*, 53(4):629-643, 2000.

[86] S. Tooley and J. M. Vanden-Broeck, Capillary waves past a flat plate in water of finite depth, *Journal of Applied Mathematics*, 69:259-269, 2004.

[87] S. Zhu and Y. Zhang, A flat ship theory on bow and stern flows, *ANZIAM. J*, 45:1-15, 2003.

[88] S. S-P. Shen, On the accuracy of the stationary forced Korteweg–de Vries equation as a model equation for flows over bump, *Q. Appl. Math.*, 53:701-719, 1995.

[89] T. B. Benjamin, Internal waves of permanent form in fluids of great depth, *J. Fluid Mech.*, 29:559-592, 1967.

[90] T. B. Benjamin, A new kind of solitary wave,*J. Fluid Mech.*, 245:401-411, 1992.

[91] T. E. Stokes, G. C. Hocking and L. K. Forbes, Unsteady free surface flow induced by a line sink in a fluid of finite depth, *Computers and Fluid*, 37:236-249, 2008.

[92] T. J. Osborne and D. M. Stump, Capillary waves on a Eulerian jet emerging from a channel, *Physics of Fluids*, 13:616-623, 2001.

[93] T. M. R. Ellis, *Fortran 77 Programming*, Addison-Wesley, 1990.

[94] T. R. Akylas, Unsteady and nonlinear effects near the cusp lines of the Kelvin ship-wave pattern, *J. Fluid Mech.*, 175:333-342, 1987.

[96] V. T. Buchwald and F. Viera, Linearised evaporation from a soil of a finite depth above a water table, *J. Austral. Math. Soc.*, 39:557-576, 1998.

[96] V. T. Buchwald and F. Viera, Linearised evaporation from a soil of a finite depth near a wetted region, *Q. J Mech. Appl. Math.*, 49:49-64, 1996.

[97] W. J. Cody, G. Meinardus and R. S. Varga, Chebyshev rational approximation to e^{-x} in $(0, +\infty]$ and application to heat-conduction problems, *J. Approximation theory*, 50-65, 1969.

[98] Y. Kang and J. M. Vanden-Broeck, Stern waves with vorticity, *ANZIAM. J*, 43:321-332, 1999.

[99] Y. M. Liu, D. K. P. Yue, On the time dependence of the wave resistance of a body accelerating from rest, *J. Fluid Mech.*, 310:337-363, 1996.

[100] Y. Nakayama and R. F. Boucher, *Introduction to fluid mechanics*, Tokyo, 1998.

[101] Yu. Z. Miropolsky, *Dynamics of Internal Gravity Waves in the Ocean*, Gidrometeoizdat, Leningrad, 1981 (in Russian; Engl. transl.: 2001, Kluwer Academic, Dordrecht).